

UNCLASSIFIED

AD NUMBER: AD0909125

LIMITATION CHANGES

TO:

Approved for public release; distribution is unlimited.

FROM:

Distribution limited to US. Government Agencies only; Test and Evaluation; 1 Aug 1972. Other requests for this document must be referred to Air Force Avionics Laboratory, Wright-Patterson AFB, OH 45433.

AUTHORITY

Per DoD 5200.1 dtd 31 Dec 1985

THIS REPORT HAS BEEN DELIMITED
AND CLEARED FOR PUBLIC RELEASE
UNDER DOD DIRECTIVE 5200.20 AND
NO RESTRICTIONS ARE IMPOSED UPON
ITS USE AND DISCLOSURE.

DISTRIBUTION STATEMENT A

APPROVED FOR PUBLIC RELEASE;
DISTRIBUTION UNLIMITED.

7

Physics of Electron Photon Interaction

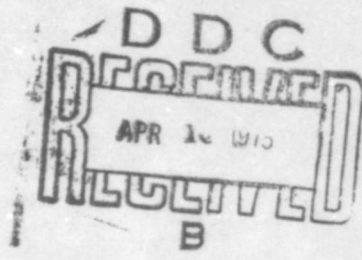
AD909125

W. T. Peria

University of Minnesota

FINAL REPORT AFAL-TR-73-43

JANUARY 1973



Distribution limited to U.S. Government agencies only; test and evaluation; Aug. 1972. Other requests for this document must be referred to AFAL/TEO, Wright-Patterson AFB, Ohio 45433.

Air Force Avionics Laboratory
Air Force Systems Command
Wright-Patterson Air Force Base, Ohio 45433

NOTICE

When Government drawings, specifications, or other data are used for any purpose other than in connection with a definitely related Government procurement operation the United States Government thereby incurs no responsibility nor any obligation whatsoever; and the fact that the Government may have formulated, furnished, or in any way supplied the said drawings, specifications, or other data, is not to be regarded by implication or otherwise as in any manner licensing the holder or any other person or corporation, or conveying any rights or permission to manufacture, use, or sell any patented invention that may in any way be related thereto.

Copies of this report should not be returned unless return is required by security considerations, contractual obligations, or notice on a specific document.

PHYSICS OF ELECTRON PHOTON INTERACTION

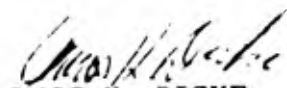
W. T. Peria

Distribution limited to US Government Agencies only; test and evaluation; August 1972. Other requests for this document must be referred to AFAL/TEO, Wright-Patterson AFB, Ohio 45433.

FOREWORD

The research described in this report was carried out in the Physical Electronics Laboratory of the University of Minnesota under Contract No. F33615-69-C-1053 - Project No. 6102, Task No. 6102-03, between October 1, 1968 and March 31, 1972. The work was supervised by W.T. Peria, Professor of Electrical Engineering, University of Minnesota, Minneapolis, Minnesota. The project monitor is W.H. Nelson, AFAL/TEO, Air Force Avionics Laboratory, Wright-Patterson Air Force Base, Ohio.

This technical report has been reviewed and is approved for publication.



AMOS H. DICKE
CHIEF, Electro-Optics Device Branch
Electronic Technology Division

ABSTRACT

A continuation of the experiment examining the sticking probability of energetic alkali ions on Ge is described. Results are given for the Ge(100)-Cs system in the zero coverage region. Experimental difficulties which forced discontinuation of the study are discussed.

A study of the Ge(100)-Cs-O photosurface is described with particular emphasis on the structural changes associated with cathode formation.

A stable negative electron affinity Si(100)-Cs-O photocathode was obtained and the optimum amount of Cs determined to be 1.3 monolayer. A work function value of ~ 0.6 eV was measured.

Experimental results of an electron scattering experiment on Ge(100) are summarized. A full report is forthcoming.

Auger spectra obtained from vacuum-cleaved alkali halide crystals are presented and some of the difficulties encountered are summarized.

Preliminary evaluation of the use of Auger spectroscopy for the analysis of aqueous solutions is described.

A description of a system for studying complex photocathodes is given.

TABLE OF CONTENTS

	<u>Page</u>
I. Introduction and Summary	1
1.1 Deposition of High Energy Alkali Ions on Semiconductor Surfaces	2
1.2 A Study of the Cesium-Oxygen Overlayer on Germanium (100)	3
1.3 The Silicon Negative Electron Affinity Photocathode	4
1.4 A Study of Electron Scattering from Germanium (100)	6
1.5 Auger Spectra of Cleaved Alkali Halides	6
1.6 The Use of Auger Electron Spectroscopy for the Chemical Analysis of Solutions	6
1.7 A System for Studying Complex Photocathodes	7
1.8 Photoemission Studies of the Alkali Covered Germanium (111) Surface	7
1.9 Photoemission Studies of Clean and Cesiumated Silicon and Germanium (100)	9
1.10 An Observation of Surface State Emission in the Energy Distribution of Electrons Field Emitted from Germanium (100)	9
1.11 Field Emission From Germanium (111)	11
1.12 A Study of the Sodium-Covered Ge(111) Surface by Ion Neutralization	12
1.13 Auger Spectra of the Elementary Constituents of the III-V and II-VI Compounds	13
II. Summary of Technical Progress	14
2.1 Deposition of High Energy Alkali Ions on Semiconductor Surfaces	14

TABLE OF CONTENTS (continued)

	<u>Page</u>
2.2 A Study of the Cesium-Oxygen Overlayer on Germanium (100)	16
2.2.1 The Clean Surface	17
2.2.2 Cesium and Oxidation	18
2.2.3 Thick Cs-O Layers	24
2.3 The Silicon Negative Electron Affinity Photocathode	25
2.3.1 Vacuum System and Accessories	25
2.3.2 The Clean Surface	25
2.3.3 Cesium and Activation	26
2.3.4 Discussion	29
2.4 A Study of Electron Scattering From Germanium (100)	31
2.5 Auger Spectra of Cleaved Alkali Halides	34
2.5.1 Experimental Procedure	34
2.5.2 Dissociation and Surface Charging	35
2.5.3 Auger Spectra	36
2.5.3.1 Lithium	36
2.5.3.2 Fluorine	37
2.5.3.3 Sodium	38
2.5.3.4 Chlorine	39
2.5.3.5 Potassium	39
2.5.3.6 Bromine	40
2.5.3.7 Rubidium	41

TABLE OF CONTENTS (continued)

	<u>Page</u>
2.5.3.8 Iodine	42
2.6 The Use of Auger Electron Spectroscopy for the Chemical Analysis of Solutions	43
2.6.1 Adsorption from Solution	44
2.6.2 The Electroplating Method	45
2.6.3 The Solvent Evaporation Method	45
2.7 A System for Studying Complex Photocathodes	46
2.7.1 The Vacuum System	46
2.7.2 Cylindrical Analyzer for Auger Spectroscopy	46
2.7.3 Film Deposition	46
2.7.4 Results	47
III. Conclusions and Suggestions for Further Study	49
3.1 Deposition of High Energy Alkali Ions on Semiconductor Surfaces	49
3.2 A Study of the Cesium-Oxygen Overlayer on Germanium	49
3.3 The Silicon Negative Electron Affinity Photo- cathode	49
3.4 A Study of Electron Scattering from Ge(100)	50
3.5 Auger Spectra of Cleaved Alkali Halides	51
3.6 The Use of Auger Spectroscopy for the Chemical Analysis of Solutions	51
3.7 A System for Studying Complex Photocathodes	51

TABLE OF CONTENTS (continued)

	Page
References	52
Figures	

LIST OF ILLUSTRATIONS

<u>Figure</u>		<u>Page</u>
1	Sticking probability at zero coverage for K ions incident on Ge(111)	55
2	Features in AES spectrum used for Cs coverage determination	56
3	Sticking probability at zero coverage for Cs ions incident on Ge(100)	57
4	Cross-section of vacuum system used for Ge(100)-Cs-O study	58
5	LEED pattern from clean Ge(100) at a) 4 eV and b) 21 eV incident electron energy	59
6	SER from clean, Cs-saturated, and optimized surfaces of Ge(100)	60
7	Initial work function change and increase in white light sensitivity with oxidation vs. Cs coverage on Ge(100)	61
8	Photoelectric yield from Cs-saturated, optimized, and heavily oxidized surfaces	62
9	SER vs. Cs coverage on Ge(100)	63
10	SER vs. oxidation for Ge(100)-Cs	64
11	LEED patterns from Cs-saturated and optimized surfaces of Ge(100) at 16 eV incident electron energy	65
12	SER from Ge(100)-Cs following normal and oxygen contaminated Cs depositions	66
13	SER from Ge(100)-Cs for normal, heated, and resequiated surfaces	67
14	SER from clean, Cs-saturated and optimized surfaces of Ge(100) following 0,1, and 5 Langmuir initial oxygen exposures.	68

LIST OF ILLUSTRATIONS (continued)

<u>Figure</u>		<u>Page</u>
15	Vacuum system for photoemission studies	69
16	Spectral yield of activated Si(100) as a function of surface treatment	70
17	Retarding potential characteristics of clean, cesiated and activated Si(100)	71
18	Photoelectron energy distributions for activated Si(100)	72
19	Schematic diagram of experimental apparatus	73
20	Inelastic electron spectra for a) annealed surface and b) sputtered surface	74
21	Inelastic electron spectra as function of E_p measured in scattering direction of (01) LEED beam at 36 eV	75
22	Inelastic electron spectra measured in (00) LEED beam direction and 2° to either side in plane of incidence	76
23	K-space plots showing scattering conditions for inelastic spectra of Fig. 22	77
24	Inelastic electron spectra measured in (00) LEED beam direction and 2° to either side in plane of incidence	78
25	K-space plots showing scattering conditions for inelastic spectra of Fig. 24	79
26	Inelastic angular intensity distributions in plane of incidence for $E_{loss} = 10$ eV and $E_p = 70-100$ eV	80
27	Inelastic angular intensity distributions in plane of incidence for $E_{loss} = 10$ eV and $E_p = 105-140$ eV	81
28	Secondary electron energy distributions as function of E_p , measured in specular scattering direction	82

LIST OF ILLUSTRATIONS (continued)

<u>Figure</u>		<u>Page</u>
29	Secondary electron energy distributions as function of E_p , measured normal to sample surface.	83
30	Secondary peak energy variation as function of scattering angle for diffraction of secondary electrons; with descriptive wave vector diagrams	84
31	Crystal holder for vacuum cleavage	85
32	Calculated Ag coverage versus observed Auger signal for drop-drying technique	86
33	Auger spectrum of gold with Ag solution drop-dried	87
34	Calculated Ag coverage versus observed Auger signal for drop-drying technique (linear region)	88
35	Auger spectra of gold sample after electroplating	89
36	Cylindrical analyzer for thin film studies	90
37	Flange mounted deposition chamber for thin film studies	91
38	$E_F - E_V$ vs cesium coverage for Ge(111)	92
39	$E_F - E_V$ vs cesium coverage for Ge(100)	93
40	$E_F - E_V$ vs cesium coverage for Si(100)	94
41	Photoelectron energy distributions from cesiated Si(100)	95
42	Energy distribution from (100) facet of Ge	96
43	Energy distribution from (111) facet of Ge	97
44	Tunnelling density of states for Ge(111)	98

SECTION I

INTRODUCTION AND SUMMARY

The general objective of the research program described in this report was the understanding of the changes in surface properties that occur when monolayer quantities of an alkali metal are adsorbed onto the surface of a semiconductor. This objective is related to the practical one of providing photoemitters with improved red response for use in imaging detectors for low light level viewing and in the detection of laser-illuminated scenes. Such photoemitters must have (among other properties) a sufficiently low work function. The necessary values can only be achieved by the addition of alkali metals (mainly cesium) to the surface, often along with some other type of impurity.

In order that efficient photoemitters can be obtained it is essential that the basic physics of alkali adsorption on semiconductors is understood. Unfortunately, until recent years, much work of this kind that has been carried out can be termed haphazard. Surfaces have been exposed to nominal sources of the adsorbate and the parameter of interest examined. There are two defects in this approach. First, there are a number of effects which can lead to surface chemical changes which are not those to be expected (e.g., the presence of impurities). Secondly, one can often gain more insight into the problem by measuring other parameters in addition to the one of interest (e.g., work function and structural changes) one parameter of great importance is the change in electronic energy level structure as a result of the adsorption. This structure determines the extent of the charge transfer between the surface and the bulk and thus the extent of the "band bending." In view of the above, three systems [Si(100), Ge(100) and Ge(111)] with alkali adsorption were studied. The combination of the techniques of photoemission, low-energy electron diffraction (LEED), and Auger electron spectroscopy (AES) enabled the property of interest (e.g., photoemission) to be correlated with surface chemistry and structure.

Since band bending is directly related to the presence of surface electronic states it is highly desirable to have means for detection of such states. Three techniques were developed and their effectiveness evaluated. The techniques were field emission, helium ion neutralization and energy analysis of photoelectrons. A fourth technique evaluation was also initiated, that of the measurement of the angular dependence of secondary electrons, which was believed to hold promise for the determination of band structure at the surface.

The third objective was a study of the complex overlayers often necessary for the activation of commercial photocathodes. It has been known for a long time that the admission of oxygen to a system at appropriate times during the cesiation of a surface leads to a lower work function than would otherwise be achieved. Thus two studies were made on the Cs-O overlayer on Ge(100) and on Si(100). The latter is of particular importance since Si(100), doped so as to be degenerately p-type, can be activated to a state of negative electron affinity. A third study was initiated to study the complex bi-alkali antimonide photocathodes. In these three studies much use was made of ancillary techniques such as LEED, AES, electron reflectance and work function measurements to supplement the photoelectric data.

In the majority of the above mentioned studies extensive use of Auger electron spectroscopy (AES) was made to ensure the chemical composition of the surface. Since AES has, with its surface sensitivity, the capability of becoming an extremely useful analytical technique, studies to characterize the spectra from elements of interest were made. The Auger spectra were obtained from cleaved surfaces of alkali halides. This data will allow comparison with alkali metal spectra obtained on adsorbed layers. In addition the halogen spectra were obtained simultaneously. The Auger spectra from the elements contained in the columns IIB through VIA of the periodic table were obtained. These are of particular interest in semiconductor device technology.

1.1 Deposition of High Energy Alkali Ions on Semiconductor Surfaces

In the previous contract period, Auger electron spectroscopy (AES) was used as a quantitative tool to examine two closely related problems involving deposition of alkali ions on semiconductor surfaces (Ref. 1):

- 1) The sticking probability of energetic K ions on a clean Ge(111) surface.
- 2) The sputtering yield of a K overlayer on a Ge(111) substrate using energetic Cs ions.

The sticking probability results were particularly interesting in that a strong energy dependence was observed (over the range 0-250 eV examined) with a sharp deviation near 20 eV (Fig. 1). This was believed to be the threshold for some energy-loss mechanism which promoted thermal accommodation of the ion to the surface. In particular, the mechanism was thought to be a damage mechanism

which would manifest itself as structural damage for ion energies greater than the damage threshold. A decision was made to extend the study to other surfaces of Ge and Si, watching closely for structural changes during bombardment. Structural damage was to be determined by means of specular electron reflectivity (SER), a measurement which is known to be very sensitive to changes in surface structure (Ref. 1).

A major fraction of the time devoted to this experiment during the present contract period was spent in construction and testing of apparatus. The data taking was cut short when it became apparent that certain apparatus limitations would make data analysis difficult. The major complication was the inability to obtain uniform quantitative alkali deposition over the range of energies desired (0-200 eV). Most seriously affected were the SER measurements of structural damage because these measurements are affected by total coverage more than by amount of damage. The experiment was terminated after relatively few measurements were taken, and the system was turned over to the study of the Ge(100)-Cs-0 photosurface.

The system was originally equipped to study the Ge(100), Ge(111)-K, Cs systems. The intent was to study the zero coverage sticking probability vs. alkali ion deposition energy. The Ge(111)-Cs data was taken before the extent of the nonuniformity problem was realized so the results are unreliable and are not given here. Nonuniformity errors were minimized in the Ge(100)-Cs experiment by taking AES coverage measurements with a defocused electron beam. The sticking probability (Fig. 3) exhibits a greater than linear dropoff from unity at low deposition energy to ~ 0.7 at 200 eV. No theoretical explanation was attempted. The experiment was terminated before the Ge(100)-K system was examined.

1.2 A Study of the Cesium-Oxygen Overlayer on Germanium (100)

A study of the Ge(100)-Cs-0 photosurface, undertaken as part of a survey experiment in the previous contract period and later abandoned (Ref. 1), was revived during the later portion of the present contract period. The work was carried out in conjunction with the Si(100) study and was designed to uncover some of the structural factors associated with the fabrication of Ge, Si-Cs-0 photocathodes as well to gain a general understanding of the Ge(100)-Cs-0 system. The structural information was obtained from measurements of specular electron reflectivity (SER) and low energy electron diffraction (LEED).

An intrinsic sample was chosen so that the flat band condition would prevail over the escape depth of the photoelectrons. This ensured that the photoelectric measurements contained only information

about the surface region without the complicating bulk contribution. A heavily doped p-type sample ($0.001 \text{ } \Omega\text{-cm}$) was prepared for later use to maximize the photoemission from bulk states.

A reproducibly clean, well-ordered surface was prepared by the sputter-anneal process and was characterized by AES, work function, LEED, and SER measurements. The best photoelectric response was obtained by depositing a saturated Cs layer and peaking the yield with oxygen. A photoelectric threshold of $1.20 \pm .10 \text{ eV}$ was obtained (Fig. 8) with a corresponding work function of $0.95 \pm .15 \text{ eV}$. Thick, low work function layers of cesium oxide were grown on the surface during one phase of the experiment but no additional enhancement of the photoelectric yield was observed. A thorough discussion of the photoelectric properties of the optimized surface was impossible because of the inability to perform photoelectric energy distribution measurements. Lack of a good work function reference prevented a more precise determination of the final work function.

Measurements of specular electron reflectivity were found to be especially helpful in understanding the cathode formation process. The size and shape of certain features in these curves at certain stages of the formation process correlated strongly with the degree of performance of the final surface. In some cases it was possible to spot irregularities which reduced the ultimate sensitivity. For example, oxidation of the clean surface prior to cesiation was found to degrade the final yield by blocking normal Cs sites. Also, slight heating of the saturated Cs layer was found to produce irreversible structural changes which prevented oxygen from optimizing the surface. One implication of the latter observation is that the ultimate photoelectric response may in fact be limited by the necessity of room temperature formation.

1.3 The Silicon Negative Electron Affinity Photocathode

Recently Martinelli (Refs. 12,13) has shown that silicon can be activated to a state of negative electron affinity by oxidation of the cesiated surface. The material employed is the (100) surface of heavily doped p-type silicon ($0.005\text{-}0.01 \text{ } \Omega\text{-cm}$). The purpose of the present study was to investigate the conditions for attaining the negative electron affinity state with silicon (100) particularly with respect to optimizing the long wavelength response.

The choice of doping concentration of the silicon is a compromise between a long photoelectron escape depth (minority

diffusion length for a negative electron affinity p-type sample) and a small band bending width. The latter is particularly important if there is band bending at the surface since it is essential that the thermalized photoelectrons be accelerated through the surface barrier with a reasonable probability of escape. The sample employed for this study was a wafer of boron doped $0.015 \text{ } \Omega \cdot \text{cm}$ p-type silicon oriented to give a (100) face parallel to the surface.

The silicon surface was cleaned by sputter-anneal cycles under ultra-high vacuum conditions. Extensive use was made of Auger electron spectroscopy, LEED and work function measurements to supplement the photoelectric measurements. Long-term sputtering (10 hours with $100 \text{ } \mu\text{A}/\text{cm}^2$ at 200 eV) followed by annealing at 1000°C after extensive outgassing of the crystal enabled a clean surface to be obtained. The LEED pattern from the surface was characteristic of a 2×1 domain surface structure although the weak quarter-order reflections reported by Lander (Ref. 7) were also visible at low ($< 30 \text{ eV}$) electron energies. No evidence of the "twinning" reported by King (Ref. 14) from Si(100) heated above 950°C was ever observed. Cesium was deposited from zeolite source and ion gun, enabling an accurate estimate of the alkali coverage to be made.

The spectral yield was monitored as a function of surface treatments (Fig. 16). In comparison to the spectral yield from fully cesiated (≈ 0.50 monolayer) n-type silicon the yield from the degenerate p-type material was much steeper in the threshold region. No evidence for emission from surface states was observed from the sample, consistent with the thin band bending region which allowed bulk valence band emission to dominate the photoelectron energy distributions. As the surface was subjected to sputter-anneal cycles the carbon and oxygen Auger signals decreased. Corresponding yield curves of the oxygen treated cesiated surfaces showed an enhancement in sensitivity as the surface became cleaner. The optimum yield was obtained from a surface sputtered clean (until carbon and oxygen could not be detected within the limits of Auger electron spectroscopy) and cooled slowly from 1000°C . The amount of cesium required was 1.2 monolayers (1 monolayer = $7 \times 10^{14} \text{ atoms cm}^{-2}$) and the white light sensitivity increased fifty-fold with activation with oxygen. The presence of carbon or oxygen on the uncesiated surface did not allow a good photocathode to be produced nor did a surface that was annealed at temperatures below 800°C . On all activated surfaces the presence of thermalized photoelectrons was clearly visible in the photoelectron energy distributions. A work function of $< 0.6 \text{ eV}$ was recorded using standard retarding potential techniques (Ref. 9) for the activated surface.

1.4 A Study of Electron Scattering From Germanium (100)

This report presents a summary of the experimental results from a low energy electron scattering experiment that was begun under another contract and completed under the present one. A full report is presently being prepared and will be submitted in the near future.

An investigation of the scattering of low energy electrons from a Ge(100) surface was initiated for the purpose of determining the types of phenomena that occur and how the surface influences the scattering properties. Low energy electrons are of special interest because their small penetration increases their sensitivity to surface interactions. It was felt that information obtained from such a study on a clean, atomically ordered surface would provide the background for investigating surfaces with adsorbates.

Measurements of the energy and angular distributions of the scattered electrons were made for the primary energy range $5 < E_p < 150$ eV. In all of these measurements, inelastic electron diffraction effects were observed to be the cause of most of the structure in the data. For much of this structure, kinematical diffraction relations could account for the observed behavior.

1.5 Auger Spectra of Cleaved Alkali Halides

This study was an extension of previous work (Sec. 1.13) to the alkali metals and halogens. The alkali halides were chosen because of their thermal stability and the ease of obtaining a clean surface by vacuum cleavage. Although considerable difficulties were encountered, such as electron beam decomposition and charging of the insulator surface, the characteristic spectra of lithium, fluorine, sodium, chlorine, potassium, bromine, rubidium and iodine were obtained.

1.6 The Use of Auger Electron Spectroscopy for the Chemical Analysis of Solutions

This phase of the program was designed to make a preliminary evaluation of AES as an analytical technique applicable to aqueous solutions. The potential advantages include: (a) a single technique would simultaneously detect all elements present and (b) the amount of sample required would be very small.

A secondary motivation for this work was the development of a technique whereby the Auger signal could be calibrated, i.e., by which the Auger signal corresponding to known quantities of a given atomic species could be determined. Satisfying both of these purposes, then,

required the quantitative transfer of a known quantity of a given material from solution to a substrate. Three methods of achieving this end were evaluated. The most promising appears to be the application of a drop of solution of known size to the substrate; evaporation of the solvent appears to leave a residue of reasonably uniform distribution.

The results emphasize the difficulty of preparing standard solutions of the necessary concentrations, which are free of unwanted contamination and the necessity of internal standards for the quantitative analysis of multi-component specimens.

1.7 A System for Studying Complex Photocathodes

A system for studying the commercial processing of photocathodes (e.g., the S20-Na₂KSb[Cs]) was evaluated. The system contained facilities for film formation using commercial techniques (i.e., alkali channels and antimony evaporator). Use of sputtering techniques enable many films to be studied without the lengthy vacuum processing time normally necessary. The films can be evaluated by monitoring the spectral yield and the photoelectron energy distributions. The film formation process can be followed with Auger electron spectroscopy. This system was employed on another contract (Ref. 23) to study the Na₂KSb[Cs] photocathode. The present study will be a continuation of this work where the data from thin films will be compared with data obtained from single crystal material.

1.8 Photoemission Studies of the Alkali Covered Germanium (111) Surface

The understanding of mechanisms involved in work function lowering of a substrate is important in the design of practical photoemitters because a decrease in work function is accompanied by an extension of the low energy limit of the spectral response and by an increase in the overall photosensitivity of the emitter. One common method used to decrease the work function of a substrate is the adsorption of monolayer amounts of alkali metals. This technique has been extensively studied for metal substrates by those interested in thermionic energy converters. However, studies involving semiconductor substrates, until recently, have been less numerous. Since semiconductors generally provide better photoelectric sensitivities than metals, the understanding of the effects caused by adsorption of an alkali on a semiconductor is needed and recently efforts in this direction have been increasing.

Palmberg (Refs. 23,24) and Cordes (Ref. 17) have studied the Ge(111)-Na system and have correlated the shape of the work function (ϕ) versus alkali coverage (θ) curve with LEED, secondary emission, and electron reflectance measurements. Chen (Ref. 25) has extended some of the aspects of this work to other systems involving overlayers consisting of mixtures of the alkalis Na, K and Cs. Weber and Peria (Ref. 9) have improved the accuracy of ϕ versus θ measurements, correlating these with LEED investigations of surface crystallography, and extending the measurements to other semiconductor-single alkali combinations, e.g. Ge(111)-Cs, Ge(111)-K, Ge(100)-Cs, Ge(100)-K, Si(111)-Cs, Si(100)-K. Based on these measurements, Weber has also proposed a model for the adsorption process for these systems involving preferred adsorption sites for the alkali, depending on coverage.

Generally, there are two mechanisms that can be active in the lowering of the work function of a semiconductor during alkali adsorption. First a decrease in the electron affinity, χ , occurs due to the dipole layer formed by the electro-positive alkali and the substrate. Secondly there can be changes in the position of the electron energy bands at the surface with respect to the Fermi level (band bending) since, effectively, the doping of the semiconductor at the surface is being changed. In general both these mechanisms are expected to be effective in any semiconductor-alkali system and an understanding of their relative importance and possible interdependence during intermediate alkali coverages would be useful. The theoretical problems involved in an analysis of the interaction between a small amount of adsorbed alkali and a semiconductor surface are so formidable that a solution to this problem has never been attempted. In fact, a complete theoretical description of a clean semiconductor surface has not yet been developed. For this reason studies of these systems have been limited mainly to experimental investigations and it has been only recently that accurate alkali deposition techniques have been developed (Ref. 9) and some more or less direct measurements have been devised to monitor the positions of the valence band edge and Fermi level at or near the surface. One of the most promising of these latter techniques is the use of photoemission measurements. This technique was used by Allen and Gobeli (Ref. 26) and has been developed more fully by Fischer (Ref. 27) as illustrated by his work on III-V compounds (Refs. 27,28, 29). In light of these developments it was felt that a useful extension of the measurements made on the semiconductor alkali systems would be that of photoemission measurements. Thus it became the purpose of this and the subsequent investigations (Secs. 2.2, 2.3, 1.9) to employ photoemission and related measurements to determine the changes occurring in the electronic energy bands at the semiconductor surface as a function of coverage with cesium or sodium.

The details of the Ge(111) study have already been reported (Ref. 3) and thus only the summary of the results will be presented here. The band bending at the surface was found to vary with cesium coverage as shown in Fig. 38. The figure is a plot of the energy difference between the Fermi level and the valence band edge at the surface ($E_f - E_{v_s}$). The fact that the surface becomes degenerate p-type at saturation coverage is in direct contradiction to the behavior commonly assumed for a semiconductor surface covered with Cs (Ref. 26,30,31). The second main feature of the investigation was the rather clear evidence (in the photoelectron energy distributions) for emission from occupied surface states in the bandgap and for the change in distribution and possible number of these states as a function of coverage.

1.9 Photoemission Studies of Clean and Cesiumated Silicon and Germanium (100)

This study was an extension of the work of Riach (Sec. 1.8) to the (100) faces of silicon and germanium. Since this work has also been reported in an interim report (Ref. 16) only a brief summary will be presented here.

The sputter-annealed (100) surfaces of germanium and silicon were studied using LEED, AES, work function measurements and photoelectric techniques. The effect of submonolayer quantities of cesium were also noted. The clean Ge(100) surface was degenerately p-type with a work function of 4.75 eV. The surface remained degenerately p-type with cesiation (Fig. 39). Sputter-annealed Si(100) had a work function of 4.6 eV and the valence band was 300 meV below the Fermi level at the surface. With cesiation the surface became more n-type until at a coverage of 12% monolayer the valence band was 650 meV below the Fermi level. No further change in band bending was observed (Fig. 40). With the Si(100)-Cs system emission from surface states lying in the band gap could be clearly observed at all coverages (Fig. 41). The effect of the observed band bending was discussed in relationship to the attainment of optimum sensitivity from the negative electron affinity photocathode.

1.10 An Observation of Surface State Emission in the Energy Distribution of Electrons Field Emitted from Germanium (100)

In the interpretation of processes which take place on the surface of a semiconductor, such as the detailed nature of the interaction between alkalis and the surface of Ge and Si, it is of interest to establish the electronic structure of the surface. In particular a more exact knowledge of the energy distribution and density of surface electronic states is desirable.

Since field-emitted electrons tunnel through the surface potential barrier, they retain information about the electronic energy states from which they originate. Therefore energy distribution measurements of field-emitted electrons should produce a means of determining the position and, possibly, the density of surface states, if the contribution from the bulk states can be identified and separated from the surface state emission. From the theoretically predicted density of surface states we expect that field emission from them will be of the same order of magnitude as bulk state emission, because the localization of the surface state electrons compensates for the larger density of the bulk states whose electrons are dispersed through the bulk. Moreover, attenuation of the bulk state wave functions may occur in the surface space charge region due to sharp band bending caused by the high field. Attenuation of the bulk wave functions would give preference to surface state electrons in the field emission process. Since the samples used in field emission have a radius of curvature from 1 to 10 microns there is some question whether surface states on the emitter can be identified with states of the planar surface. However, the major characteristics of electronic states are determined by nearest-neighbor and next-nearest-neighbor interactions. Since the surface of a field emission point can be considered flat, on an atomic scale, we should not expect a strong perturbation of the surface states due to the small radius of curvature. This is particularly true of annealed Ge emitters which develop broad, low index facets. The effect of the applied field on the surface states may, however, be considerable and this provides the greatest source of concern in attempting to compare field-emission results to those obtained from the field-free, planar surface.

Arthur (Ref. 32) has measured the energy distribution of electrons field emitted from (100) and (111) oriented Ge emitters. Although the measurements were made in a retarding potential analyzer which viewed a relatively large portion of the emitter, and may have suffered from trajectory problems, he did observe electrons which apparently originated in the band gap. His results suggest the possibility that a field-emission measurement would be fruitful in attempting to detect surface states directly.

This study has been reported in an interim report; (Ref. 33 a) only a summary is presented here.

Measurements of the energy distribution of field emitted electrons, using an angularly selective energy analyzer, avoided problems associated with electrons which have large transverse momentum components, thus yielding accurate energy distributions largely free of apparatus distortion.

Field emission from the (100) facet of Ge was characterized by a band of surface states which overlapped the valence band edge (Fig. 42) and were very sensitive to contamination and to geometric variation of the surface structure. The density-of-states function multiplied by a rate term rose to a peak .18 eV above the valence band edge. The states tended to be localized to the center of the (100) facet on a field emission point.

The density (6.3×10^{12} states/cm²) and energy distributions of the states observed in field emission agreed reasonably well with the findings of others, perhaps indicating that the field emission measurements can be related to observations on planar, field-free surfaces. The major observable effect of the high fields necessary to field emission appears to be a slight broadening of the density of states function of both the surface and bulk states. The geometric sensitivity and response to contamination by the surface states showed that they were not caused by the applied field.

The most plausible model for the surface states was based on a Kronig-Penny type calculation which predicted a single value for the tunneling probability for electrons in the surface state band at a given applied field. The same model may be pertinent to dangling bonds at the surface.

1.11 Field Emission From Germanium (111)

This study was an extension of that of Shepherd (Sec. 1.10) and is also the subject of an interim report (Ref. 33b) where details of the study are presented.

In addition to detecting electrons which tunneled from the bulk valence and conduction bands, a broad band of electrons with energies in the forbidden gap was observed (Fig. 43). With the applied field the (111) surface was found to be ~ 2 kT n-type. This corresponds to $2.4 \pm 0.24 \times 10^{13}$ electrons/cm² residing in filled surface states. The variation of surface potential with applied field was used in determining the density of states near

the Fermi-level to be $4.8 \pm 1.4 \times 10^{13}$ electrons/cm² eV. The tunnelling density of states (TDS) was derived from the experimental energy distributions (Fig. 44), in conjunction with simplifying assumptions made necessary in the absence of surface state band structure information. This TDS overlaps the valence band by 125 meV, has a maximum 175 meV above the valence band edge and a minimum at mid-gap and then increases sharply towards the conduction-band. Since these results were consistent with those obtained by Shepherd on Ge(100) for both the TDS and the band bending it is suggested that the field emission TED data can be related, in a simple manner, to the energy density of surface states. Some implications of the observed surface state differences for the Ge(100) and Ge(111) surfaces are discussed in relation to the attainment of negative electron affinity in Ge photoemission devices.

1.12 A Study of the Sodium-Covered Ge(111) Surface by Ion Neutralization

The third technique (photoemission the first and field emission the second) that was evaluated for its potential to detect surface states was that of helium ion neutralization. It is well known that ion neutralization is extremely sensitive to the surface conditions. Thus the ion neutralization spectroscopy (INS) technique (Ref. 34) developed out of an extensive series of experimental and interpretive studies of Hagstrum (Refs. 35,36) was intended as a technique for the study of the alkali semiconductor surface. This research has also been the topic of an interim report (Ref. 37) and thus only a summary of the results will be given.

The essential apparatus utilized in this study consisted of a demountable vacuum system containing a helium ion gun, a sodium ion gun, a LEED unit and an ion sputtering chamber. The helium ion beam, generated and focussed into a collector assembly, was neutralized at the sample surface with the consequent ejection of Auger electrons having an energy distribution characteristic of the surface. The surface was changed by sodium deposition, characterized by LEED and work function measurements. Through these characterizations, data obtained in this study was compared with results of other studies of the same surface by a variety of different techniques.

As expected, the total electron yield, defined as the number of Auger electrons emitted per incident ion, was closely related to the work function of the sample and was virtually independent of the ion kinetic energy. The change in the measured width of the Auger electron energy distribution indicated that Ge(111)-Na

surfaces were always p-type, in agreement with the previous studies utilizing the photoemission technique. The distributions, and thus the transition density function (TDF) for the Ge(111)-Na surface varied more readily for surfaces with light sodium coverage. This observation was used to substantiate the model, suggested by LEED and electron reflectance data that sodium adatoms allow the selvedge germanium atoms to relax to their bulk positions.

A numerical approach, utilizing the Laplace transformation in conjunction with a least-squares curve fitting procedure, has been formulated to derive the TDF from the measured distributions.

1.13 Auger Spectra of the Elementary Constituents of the III-V and II-VI Compounds

Auger electrons are created within relatively large depths from the surface since the penetration depth of the high energy primary electron beam is large. However the Auger electrons created must escape from the material without suffering inelastic collisions in order to retain their identity. This escape depth is of the order of five to ten Å (Refs. 38,39), so Auger spectroscopy can be said to be a surface sensitive tool. Concentrations of the order of .01 monolayer (Ref. 40) can be detected.

Each element gives rise to a characteristic Auger spectrum which consists of a series of peaks in the electron energy distribution related to the atomic energy levels of the element. A study was initiated to obtain the Auger spectra of several elements which are common constituents of semiconducting compounds such as GaAs, InSb and CdTe. Auger spectra of Cu, Zn, Ga, Ge, As, Pd, Ad, Cd, In, Sn, Sb and Te have been obtained and are presented. It is expected that these spectra will aid workers in studying surfaces composed of such elements. This study has been published as an Interim Report (Ref. 41).

SECTION II

SUMMARY OF TECHNICAL PROGRESS

2.1 Deposition of High Energy Alkali Ions on Semiconductor Surfaces

The study of the sticking probability of energetic K ions on clean Ge(111) undertaken at the end of the previous contract period (Ref. 1) was expanded this period to include both K and Cs on Ge(100) and Ge(111). The motivation for continuing the study was the observation for Ge(111)-K (Ref. 1) of a sharp discontinuity in the rate of change of the sticking probability near the expected damage threshold (Fig. 1). The thrust of the present experiment was thus to watch for structural changes during ion bombardment, correlating these, if possible, with changes in the sticking probability. Structural damage was to be monitored by means of specular electron reflectivity (SER), a measurement which is known to be very sensitive to changes in surface structure (Ref. 1).

A complete description of the vacuum system and apparatus used in the experiment is given in Sec. 2.2. The functions which could be performed included sputter-anneal cleaning of the sample, deposition of energetic (0-200 eV) K and Cs ions in controlled submonolayer amounts, and measurements of Auger electron spectroscopy (AES), specular electron reflectivity (SER), low energy electron diffraction (LEED), and work function.

The zero coverage sticking probability was taken as the ratio of the actual alkali coverage to the measured coverage. The measured coverage was determined by integrating the ion flux to the sample (typically 3.1×10^{13} ions on the 0.5 cm^2 sample or $\sim .10 \text{ m}$ at unity sticking coefficient) while actual coverage was found by comparing the alkali Auger signal following energetic deposition to that obtained from a calibration at low incident energy. The low energy calibration was done at 2 eV incident ion energy where the sticking probability was assumed to be unity. Structural damage was to be determined with SER and LEED, but these measurements were never taken for reasons which will be discussed later.

It was determined at the onset of the study that uniform ion deposition was an important experimental consideration. An ion gun was designed which accomplished uniform deposition by sweeping a focused beam from an aluminosilicate source in a raster. The focused beam was produced by means of a 3-aperture Einzel lens and the sweeping was accomplished by means of deflection plates. When the guns were tested, space charge spreading was found to be a serious

problem at the current densities necessary for reasonable deposition rates ($> 10^{-8}$ amps/cm²). This necessitated a return to the cylindrical anode design commonly used in this laboratory. These guns were incapable of better than 10% uniformity over the range of deposition energies used, making it difficult to obtain meaningful SER measurements. The SER measurements depend just as strongly on the total coverage as on the amount of structural damage.

Other experimental difficulties were encountered which were related specifically to the Ge-Cs system. It is necessary to discuss the procedure for measuring the sticking probability in order to understand these difficulties. The large 47 eV Cs peak was used as the Cs coverage indicator. This peak occurred on a sharply rising background and coincided with the low energy Ge doublet. Actual Cs coverage was determined from a calibration at low deposition energy of the ratio $R = A/B$ defined in Fig. 2. R was found to be dependent upon the placement of the sample in the hemispherical LEED-Auger analyzer as well as on the inner grid potential, the suppressor grid modulation amplitude, and the condition of the phosphor screen collector. Although these factors were potentially troublesome in view of the minuteness of the changes expected, it was felt that they could be controlled sufficiently during a single experimental run to be able to extract meaningful results.

Several other minor factors deserve mention. The first is related to the fact that the measured flux of ions may not be the true flux because only the total charge delivered to the crystal is measured. Errors occur if there is an appreciable number of ions reflected without charge transfer or if there is appreciable emission of secondary electrons. In the energy range of interest (0-200 eV) neither of these phenomena was expected to affect the results by more than 1% (Ref. 2). The second factor involves the use of AES to determine coverage. Since Auger electrons have short escape depths, AES would not detect ions which could be implanted at higher deposition energies. This effect was not expected to be a problem at the deposition energies used in this experiment. Finally, there is undoubtedly some complication of the zero coverage data due to resputtering of the overlayer. This effect was expected to be small because only ~ 10 m was deposited during each run.

The Ge(111)-Cs results are not given here because the data was obtained before the nonuniformity problem was fully realized. McNeil's Ge(111)-Cs results (Ref. 1) are suspect for the same reason.

However, it can be safely stated for both cases that the sticking probability decreases with increasing ion energy. The Ge(100)-Cs results are shown in Fig. 3. Nonuniformity was circumvented in this experiment by taking measurements of actual coverage with the electron beam defocused sufficiently to cover most of the sample. Sticking probability values are not expected to be in error by more than $\pm 5\%$. No attempt was made to fit the data to a theoretical model. The experiment was terminated before the Ge(100)-K system was examined. The decision to terminate the experiment was based chiefly on the inability to obtain measurements of structural damage.

2.2 A Study of the Cesium-Oxygen Overlayer on Germanium (100)

The vacuum system used in the Ge-Cs-O experiment was a standard 12" diameter stainless steel chamber (Ultek TNB-X) with 100 l/sec ion pumping. The background pressure during the experiment was always $< 1 \times 10^{-10}$ Torr. A cross-section of the system is shown in Fig. 4. The Ge sample was situated at the center and could be rotated via the sample manipulator to any of several measurement stations. It was mounted securely to a tantalum block which was heated by an internal filament. The sample could be heated to 550°C via thermal contact with the tantalum holder and up to its melting point with additional electron bombardment.

Distributed about the center of the system were pieces of apparatus for performing various surface treatments on the sample and for obtaining relevant electrical measurements. A sputtering chamber was used to clean the sample by argon ion bombardment. Controlled amounts of Cs were deposited with an aluminosilicate source and ion gun, and oxygen was introduced from an oxygen flask through a high vacuum valve. The available electrical measurements included photoelectric yield, work function, specular electron reflectivity (SER), low energy electron diffraction (LEED), Auger electron spectroscopy (AES), and secondary electron energy distribution data (SED).

Photoelectric yield measurements were taken with the double monochromator system described in Ref. 3, using the sputtering chamber as collector. The front viewport (7056 glass) was used as the window; its optical properties limited measurements to energies below 3.1 eV (0.400 μ). The full intensity energy spread was < 0.04 eV throughout the measured range and photoyield values greater than 10^{-9} electrons incident photon were estimated to be within 10% of absolute. The window limitation prevented the acquisition of any clean surface photoelectric data.

Work function and specular electron reflectivity measurements were obtained with the SER gun. Details of the operation of the gun are outlined in Ref. 4. The gun is patterned after one described by Zollweg (Ref. 5) and has an effective energy spread of less than 100 meV. Because of the small spread it is possible to detect very small work function changes (~ 20 meV). The SER curves (electron reflection coefficient vs. incident energy) obtained with the gun consist of the 00 diffraction beam superimposed on a smoothly varying background. The curves are understandably sensitive to surface order. The planar collector geometry of the Zollweg gun excludes higher order diffracted beams from the collector current at all primary energies and thereby insures that all maxima can be ascribed to intensity maxima of the 00 beam.

Surface cleanliness was determined with the LEED-Auger analyzer by means of Auger electron spectroscopy. This technique also provided a quantitative measure of Cs and oxygen coverage when submonolayer quantities of these materials were present. LEED patterns observed with the analyzer were used as additional structural indicators. SED spectra were also measured with the analyzer. Maxima in the distributions, believed due to interband transitions, were expected to shift whenever there was a change in the amount of band-bending in the surface region. A peak at ~ 3 eV due to electrons from the Γ_1 and/or Δ_2 conduction band minima was the most obvious feature.

2.2.1 The Clean Surface

The intrinsic Ge sample was cut and a (100) surface was mechanically polished and was cleaned in vacuum by the sputter-anneal process. Surface cleanliness was monitored with AES and carbon was found to be the principal contaminant. Unlike the case of Si, the carbon was readily removed with several light sputter-anneal cycles. The process was continued until the carbon peak in the Auger spectrum was $< 1/50$ the size of the 105 eV Ge peak. This level corresponds to $< 0.2\%$ monolayer and approaches the limit of detectability of carbon. Concentrations giving a ratio of $1/5$ were observed to obliterate most of the structure in the clean surface SER. A similar ratio has been observed to seriously degrade the Ge(100) LEED structure (Ref. 6). No sulfur or oxygen was observed on the clean surface.

The clean surface exhibited a good quality Ge(100)-4 diffraction pattern similar to that observed by Lander and Morrison (Ref. 7). The partially resolved "1/4-order" beams were quite evident at 21 eV incident energy and became almost totally resolved at 4 eV (Fig. 5). Features in the clean surface SER (Fig. 6) were reproducible to within

5%. They were noticeably diminished when the surface was contaminated or improperly annealed. The work function of the clean surface was reproducible to within 50 mv. No photoelectric measurements were taken on the clean surface because of the window limitation mentioned earlier.

2.2.2 Cesium and Oxidation

The Ge-Cs-O photosurface was usually prepared by depositing a saturated Cs layer (~ 1.0 m) on the clean surface and then admitting enough oxygen to maximize the white light yield. (In some cases the yield for 1.50 eV (0.826 μ) photons was maximized but the results were identical.) Any degree of cesiation short of saturation gave inferior results upon oxidation, and no other combination of cesium and oxygen treatments gave a better photoelectric yield. In the discussion to follow the final surface is referred to as the "optimized" surface and is symbolized by Ge(100)-Cs-O. The intermediate state is called the "Cs-saturated" surface and is written Ge(100)-Cs.

It should be noted that the cesiation process in the present experiment was complicated by oxygen contamination associated with the Cs source. This made it difficult to separate the steps of cesiation and oxidation. Oxygen-contaminated Cs-saturated surfaces were observed to have lower work functions and photoelectric thresholds than less contaminated surfaces. However it was found that the amount of oxygen acquired during cesiation did not markedly affect the final outcome of the optimized surface. This may reflect the fact that the sticking coefficient of oxygen on clean Ge is much smaller than on cesiated Ge (Ref. 8) so that much of the oxidation took place during the final stages of cesiation. No other contaminants were detected in the Cs layer.

The amount of oxygen contamination was determined by AES and was found to depend largely upon deposition time. For this reason the ion gun was focused to obtain a greater ion flux to the sample. A deposition rate of 0.30 m/min was achieved, resulting in an oxygen content $< 1/10$ the amount in the optimized layer. An undesirable sequence of the focused deposition was the introduction of coverage nonuniformity. This did not appear to be a serious problem, except at low coverages (< 0.5 m), because of the greater mobility of Cs on partially cesiated surfaces. AES indicated a 15 to 20% coverage variation across the sample at 0.5 m and an undetectable level at saturation. The work function of the Cs-saturated surface was found to be extremely uniform, falling within the limits of reproducibility (± 20 meV) across the sample.

In addition to its uniform coverage, the Cs-saturated surface was both reproducible and stable. The work function remained constant within ± 20 meV over periods exceeding 30 hours. This made it possible to characterize the surface with a reasonable degree of certainty. The partially cesiated surface was not uniform nor reproducible, hence few measurements were taken on it. Those that were taken were regarded as having only qualitative significance.

Work function change ($\Delta\phi$) vs. Cs coverage (θ) is plotted in Fig. 7. It is evident that the minimum work function occurs prior to, and not at, saturation, the exact coverage being uncertain because of the nonuniform Cs deposition. The value $\theta = .65$ is however, in good agreement with the independent observations of Weber (Ref. 9) and Jeanes (Ref. 10). The slight differences in $\Delta\phi$ at $\theta = .65$ from run to run are probably due to differences in the amount of oxygen contamination. It should be noted that in this experiment the final work function shift $3.18 \pm .05$ eV was within experimental error of the value obtained by extrapolating several oxygen contaminated values back to zero contamination.

The photoelectric yield from the Cs-saturated surface corresponding to the 3.18 eV shift is shown in Fig. 8. A threshold of $1.50 \pm .10$ eV is derived from the $Y^{2/5}$ plot. Assuming the surface was initially degenerately p-type (Ref. 10), these values suggest a clean surface work function of $4.68 \pm .15$ eV or lower, depending upon the amount of band bending with cesiation. M.R. Jeanes has done an extensive photoelectric study of the Ge(100)-Cs system (Ref. 10) using an identical sample (cut from some boule, prepared in identical manner), but only to a coverage of 0.70 m. He observed a clean surface work function of 4.75 eV and little or no deviation from p-type degeneracy throughout cesiation. The agreement between the values of clean surface work function obtained in the two experiments indicates there is probably little additional deviation from degeneracy beyond 0.70 m coverage.

The addition of a small amount of oxygen to the Cs-saturated surface reduced the work function by another 0.45 to 0.55 eV, the extent depending upon how long this optimized surface was allowed to age (aging times ~ hours). The photoelectric threshold experienced a similar decrease, but the exact amount of the shift was uncertain due to the inability to obtain data below 1.20 eV (apparatus limitation). It was impossible to arrive at a conclusion about the amount of band bending on the basis of the SED measurements. The structure in these curves was not resolved well enough that small shifts (~ 0.1 eV) could be detected. The photoelectric yield data shown in Fig. 8 is for a surface that had experienced an additional work function shift of 0.50 eV with oxidation.

The optimized surface was uniform reproducible, and stable, with the exception of the aging phenomenon mentioned earlier. Surfaces which were kept in vacuum always tended toward higher yield and lower work function. No deterioration was ever observed over periods as long as several days. The surfaces were also found to be relatively stable to the addition of small amounts of excess oxygen. The yield always decreased with excess oxygen but recovered within minutes to the original value when the oxygen flow was stopped. For this reason the maximum yield state is thought to signal a major change in the oxygen adsorption characteristics of the surface.

There was no accurate means of determining the amount of oxygen necessary to achieve the optimized state. The ion pump current indicated an exposure of $\sim .02$ Langmuir, but this value could have been as much as a factor of 10 low due to the dynamics of the measurement and to the relative positions of the pumps, gas inlet, and sample. The ratio of the 520 eV oxygen Auger peak to the 565 eV cesium Auger peak (hereafter referred to as the O/Cs ratio) was $0.7 \pm .10$. This was 10 times greater than the ratio observed for the freshly cesiated surface, slightly oxygen contaminated from the ion source.

A heavy oxygen exposure (~ 2 Langmuir) caused the photoelectric threshold to increase considerably as shown in Fig. 8. The shift was generally not reproducible and depended upon the amount of oxygen exposure and the length of time before measurements were taken. Oxygen was found to desorb during AES measurements (2000 eV, 50 μ a beam), making it impossible to obtain a precise value for O/Cs. At various stages of bombardment O/Cs varied from 1.37 to 0.80, the photoelectric yield approaching the optimized curve as O/Cs approached the optimized value. The optimized surface was found to be much more stable to electron bombardment.

The work function corresponding to the heavily oxidized yield of Fig. 8 was $1.90 \pm .15$ eV. Lack of appreciable emission near the Fermi level indicates a certain amount of band bending. However, a precise picture is not possible without photoelectron energy distribution data. SED measurements substantiated the band bending conclusion. The peak at ~ 3 eV in the distribution was observed to shift $0.40 \pm .20$ eV toward n-type during the heavy oxidation. This requires the emission in the threshold region to originate elsewhere than from bulk states; e.g., from filled surface states or from adsorbate-created states.

Measurements of SER greatly enhanced the understanding of the photocathode formation process. (These curves represent the specular beam intensity superimposed on a smoothly varying background and are very reproducible for a given surface because of the ability to maintain constant target current.) The size and shape of certain

features in the curves (especially those appearing during cesiation) were found to correlate strongly with the degree of performance of the final surface. A summary of the SER data from the clean, Cs-saturated, and optimized surfaces is shown in Fig. 6. No attempt was made to interpret the origin of the diffraction features, only to use them as an indication of trends during cathode formation.

A collection of SER curves taken at coverage intervals of 0.1 m is shown in Fig. 9. The curves vary markedly with Cs coverage. The clean surface peak A at 8.5 eV gradually diminishes and a new peak B in the 15 to 20 eV range grows until at ~ 0.5 m new features suddenly appear, notably peak C at 16.5 eV and the double peak D at 3 eV. The latter features stabilize at ~ 0.9 m (this figure may be low due to the nonuniform deposition) and deteriorate only slightly with further cesiation. There is also a slight increase in peak B relative to peak C with further cesiation. The deterioration beyond 0.9 m is believed due to oxygen contamination from the Cs source rather than to additional Cs and the surface is presumed to have reached saturation. AES results indicate that there is no further increase in the size of the Cs Auger peaks beyond ~ 1.0 m coverage. Optimization of partially cesiated surfaces (Fig. 7) also indicates saturation in the 1.0 to 1.2 m range. It should be pointed out that the aforementioned coverage values depend on the assumption (which may not be strictly true) that the sticking probability is unity up to saturation and zero beyond.

SER vs. oxidation is shown in Fig. 10. The dominant feature is the huge increase in the magnitude of peak B and its gradual shift to higher energy. This is accompanied by the disappearance of the double peak D and the appearance of the peak E out of the shoulder at 5.5 eV, along with a general increase in the background. The increase in B is thought to indicate a strong ordering of the Cs layer. LEED results (Fig. 11) substantiate this conclusion. The 1/2-order reflections are generally weak for the Cs-saturated surface but increase considerably in intensity with oxidation. The entire LEED pattern from Ge(100)-Cs-0 was noticeably sharp and strong, indicative of a well-ordered surface.

It is evident from Fig. 10 that peak photoresponse (white light) and maximum magnitude of peak B do not coincide. The latter, in fact, continues to grow until the white light yield drops to one-half its maximum value. This implies that additional oxygen applied to the optimized surface continues to promote ordering of the Cs but at the same time begins to form an oxide layer which increases the electron affinity of the surface. When oxidation is carried to saturation, peak B stabilizes at approximately one-half its maximum height.

Several additional experiments using SER measurements provided further information about the Cs layer. The first involved adjusting the focus of the ion gun during Cs deposition so that Cs was deposited at about 1/10 the normal rate. This resulted in considerably more oxygen contamination and slightly more Cs (< 5%) than usual in the Cs layer ($O/Cs = 0.49$ instead of the usual 0.7). The SER from the Cs-saturated surface (Fig. 12) was very similar to that observed on a partially oxidized uncontaminated surface. This may have merely indicated, as noted earlier, that much of the oxidation took place at later stages of cesiation when the sticking probability for oxygen was higher.

The second experiment examined the effect of heating on the Cs-saturated surface. The heating temperature (< 100°C) was chosen such as to raise the work function by at least 0.2 eV. The SER from the heated surface is compared to that from the Cs-saturated surface in Fig. 13. Peak C is diminished or absent while peak B is increased. The LEED pattern from this surface was less distinct and slight streaking of the 1/2 order beams was observed. Recesiation (totaling 0.90 m) did not restore C (Fig. 13) even though the work function shift 3.18 eV was restored. AES indicated a 15% reduction in the 45 eV Cs peak on the heated surface and 8% on the recesiated surface. Oxidation of the recesiated surface did not produce an appreciable increase in the photoelectric yield. AES indicated a deficiency of oxygen ($O/Cs = 0.37$) on the oxidized surface. These observations indicate clearly that irreversible structural changes take place when the Cs-saturated surface is heated; these changes apparently prevent oxygen from playing the proper optimizing role. They may, in fact, occur to some degree at room temperature, thereby partially limiting the response of the room temperature formed photosurface.

A third experiment was designed to examine the effect of precesiation oxidation on the ultimate performance of the photocathode. Oxygen exposures of 1, 5, and 20 Langmuir were used. SER results are summarized in Fig. 14; work function and AES results in Table 1. Peak A in the SER is observed to diminish with oxidation on the clean surface, as are C and D on the Cs-saturated surface and B and E on the optimized surface. The latter two sets of curves are not unlike those obtained from partially cesiated surfaces. Coupled with AES data indicating less Cs on the initially oxidized surfaces, the implication is that Cs sites are destroyed during the initial oxidation. The end result is a higher work function on the optimized surface.

TABLE 1

		Oxygen exposure, Langmuir				Error
		0	1	5	20	
520 eV oxygen Auger peak height (after initial oxidation)	Arbitrary Units	-	7	16	22	± 2
520 eV oxygen Auger peak height (after optimization)		69	68	64	62	± 5
565 eV cesium Auger peak height (after optimization)		100	94	92	84	± 5
O/Cs (after optimization)		0.69	0.73	0.70	0.73	$\pm .05$
Δ^m Ge-0	eV	-	+0.02	+ .07	+ .10	$\pm .02$
Δ^m Ge-0-Cs		-3.18	- 3.20	-3.24	-3.26	$\pm .05$
Δ^m Ge-0-Cs-0		-3.73	- 3.65	-3.57	-3.56	$\pm .05$

2.2.3 Thick Cs-O Layers

Several attempts were made to grow thick, low work function layers on the Ge sample. Two different methods of growth were used, neither of which produced well-defined surfaces because of nonuniform Cs deposition. Another factor which complicated the growth process was the inability to monitor photoemission during cesiation. None of the final surfaces exhibited a photoelectric yield better than that of the "optimized" surface.

The first method consisted of exposing a heavily oxidized Cs-saturated surface alternately to Cs (1.0 m) and oxygen, each time optimizing the photoelectric yield with the oxygen. Cs-O treatments beyond the first did not increase the photoelectric yield by more than 20% or decrease the work function by more than 50 meV. Because the LEED pattern was still unaltered after the fourth treatment, it was concluded that succeeding layers were not sticking.

The second method was identical to the first, except that cesiation was followed by a heavy oxidation (~ 3 Langmuir exposure) rather than an admission of only enough oxygen to optimize the yield. When photoelectric and work function measurements were desired, the procedure was terminated with an "optimizing" oxidation. Cs and oxygen exposures equivalent to 18 monolayers of Cs were applied. It was impossible to determine the thickness of the Cs-O layer due to nonuniformity of Cs deposition and also to uncertainty as to the extent of Cs desorption. Evidence that some buildup occurred was obtained from the observation of exoelectronic emission during oxidation. Efficiencies in excess of 10^{-4} electrons/incident molecule were observed, which is indicative (for cesium oxide) of a thick, low work function layer (Ref. 11).

Energy distribution measurements were made of the exoelectronic electrons using a d.c. differentiation technique with the sputtering chamber as collector. A single peak was observed 450 meV above the thermionic peak. This was taken as evidence that only one type of oxide was being formed (Cs_2O), at least during the early stages of oxidation when the measurements were taken. The electron current was found to be directly proportional to the oxygen pressure as expected, and was observed to decay exponentially in time for a constant oxygen pressure.

As successive Cs-O layers were formed, the surface became increasingly unstable. Work function measurements at later stages of growth were not reliable due to surface instability under electron bombardment. The photoelectric yield was always low and relatively stable for oxidized surfaces and increased with Cs deposition. The cesiated yield, especially in the threshold region, decayed with a time constant of hours. This effect was particularly evident at later stages of film growth, and was thought to represent desorption of loosely bound Cs.

2.3 The Silicon Negative Electron Affinity Photocathode

2.3.1 Vacuum System and Accessories

The study was made in a stainless steel vacuum system (Fig. 15) which after processing and bakeout was capable of a vacuum of less than 5×10^{-11} Torr. The facilities available consisted of argon ion bombardment, electron bombardment heating, cesium ion deposition and an oxygen activation system. The techniques available were Auger electron spectroscopy (capable of detecting $< 1\%$ monolayer of most common impurities), LEED, work function measurements, residual gas analysis and photoemission measurements. The latter included energy analysis of the photoelectrons with a three-grid hemispherical analyzer as well as the determination of the spectral yield. The crystal heating consisted of either electron bombardment from the back surface (abandoned in later studies because of non-uniform heating) or resistive heating. In either case temperatures up to 1100°C were routinely attainable. Sample temperature was monitored with an optical pyrometer.

The vacuum system was pumped with a 100 l/sec ion pump which could be "isolated" by means of a large plate valve from the main chamber. Auxiliary titanium getters were situated both in the pumping well and in the main chamber. Rough pumping ($> 10^{-2}$ Torr) and removal of high pressures of inert gases (argon) was achieved with sorption pumps.

2.3.2 The Clean Surface

The heavily boron doped ($0.01 \Omega \text{ cm}$ p-type) silicon wafer was cut to expose the (100) face. The surface was mechanically polished to give a smooth mirror surface and etched in hydrofluoric acid prior to insertion into the vacuum system.

The method of cleaning the surface was argon ion-bombardment followed by long term outgassing and anneal cycles. The procedure for ion bombardment was to clean the argon by cataphoresis (Ref. 9) prior to admission into the chamber. The getters in the chamber

were flashed, the plate valve closed, the ion pump switched off and argon introduced to $\sim 3 \times 10^{-3}$ Torr pressure. Typical sputtering parameters were $100 \mu\text{A cm}^{-2}$ at 150 volts, although early bombardments were at 250 volts to remove the oxide. Between 1000 and 2000 monolayers were removed during the cleaning process.

Prior to bakeout of the system and any heating of the crystal the surface was sputtered to remove any diffusible contaminants. After bakeout the crystal was outgassed for twenty hours at 900°C and resputtered ($100 \mu\text{A cm}^{-2}$ at 250 volts) until Auger electron spectroscopy showed the oxide was removed. The silicon was now sputtered at 150 volts and annealed at 900°C . This produced a surface with only a small amount of carbon (determined by monitoring the carbon 273 peak) and a reasonable LEED pattern. However, the carbon could not be completely removed until the surface had been subject to fifty hours outgassing at 900°C (in ten hour periods) with intermittent sputtering cycles. The resultant surface gave a high quality LEED pattern characteristic of clean silicon (Ref. 7). No sign of boron was ever observed in the Auger spectra of the clean surface although the doping level employed ($\sim 10^{18}$ atoms cm^{-3}) was such that a sensitivity better than 0.001 monolayers would have been required, unless surface segregation had occurred.

2.3.3 Cesium and Activation

Two methods of cesiating the sample were investigated. The first technique was to use the cesium aluminosilicate zeolite as a source of cesium ions. The second was to use a commercial channel source.

The advantages of the ion source are that considerable experience has been acquired in this laboratory with such sources and the quantitative nature of the deposition. This latter feature is of particular importance if the mechanism for the work function lowering is that of an ordered structure as suggested by Levine (Ref. 15). Another advantage of such sources is that they can be very easily outgassed (an ion current is not drawn from the source unless an accelerating potential is applied to the first grid) a feature not available with commercial channels.

A major disadvantage of ion sources is that, unless an ion gun is used to first focus and defocus the ion beam, poor uniformity and low cesiation rates result. Even with optimization of gun electrodes it was difficult to get cesiation rates above 0.2 monolayers-minute.⁻¹ However, perhaps the most serious objection is that such sources have been shown to give off oxygen as a contaminant (Ref. 16). This source of contamination is very difficult to eliminate since it arises from a solid state electrolytic process in the zeolite. However, with careful use of the gun (i.e. running in the space

charge mode) this contamination can be minimized (to less than 1%) monolayer of oxygen with the deposition of 1.5 monolayers of cesium.

The advantages of the cesium channel source are that the deposition rate can be varied to give high rates. Also the problem of oxygen contamination seen with the ion sources can be eliminated. The disadvantage is that it is difficult to make the deposition quantitative with precalibration since in the monolayer range of interest (1-2 monolayers) most of the techniques, such as Auger electron spectroscopy or work function measurements, do not allow unambiguous interpretations. Also, because of the chemical nature of the source it is very difficult to outgas. This problem is usually minimized by "flashing" the channel so that it is hot for only a short period.

Although both techniques were attempted it was felt that the ion source advantages outweighed the drawback of a slight oxygen contamination and thus the ion source was used throughout this study. The deposited cesium overlayer was shown to be clean (except for the small oxygen contamination) by Auger spectroscopy.

The optimum photocathode was investigated as a function of surface treatments. The standard treatment was to deposit ~ 1.3 monolayers of cesium onto the surface and to optimize to white light with oxygen. A series of spectral yields is shown in Fig. 16. For reference the spectral yield from Si(100)-100 Ω cm-n-type (Ref. 16) with 0.5 monolayers of cesium then optimized with oxygen is also shown.

Curve A was obtained from a surface that had been sputtered and annealed from 950°C. AES showed carbon to be still present. Upon activation the white light response increased four fold. As the sample was cleaned further and again annealed from 950°C the carbon contamination decreased giving a yield similar to curve C. At this point photo electron energy distributions showed a sharp low energy peak characteristic of thermal electrons. The residual carbon was decreased further by sputtering and the corresponding yield of the activated surface increased in the threshold region (Curve D). The yield could be further increased by annealing from 1050°C (Curve E). At this point the white light sensitivity of the cesiated surface increased fifteen-fold upon activation with oxygen. The yield could not be increased beyond this point by further sputtering or annealing. The LEED pattern of the surface was very sharp, suggesting good surface order.

As previous studies with cesium ion sources had shown that oxygen contamination could occur during cesiation, the freshly cesiated surface was studied before activation. It was found that $\sim 6\%$ monolayer of oxygen was present. This contamination was minimized by increasing the ion flux and running the gun in a space-charge-limited mode. The spectral yield increased dramatically as the oxygen contamination was decreased. (Curves F, G and H). The main differences among the three curves lie in the degrees of uniformity. This arises because the increased cesium flux necessitated some sacrifice of uniformity, although the migration of alkali ions with high coverages (Ref. 17) would minimize this effect. Also shown in Fig. 16 is the spectral yield recorded by Martinelli (Ref. 12). Although the removal of carbon, the attainment of a well-ordered surface, and the minimization of oxygen on the fully cesiated surface resulted in a photocathode with the response shown in Fig. 16, Curve H, the sensitivity was only $340 \mu\text{A/lumen}$ as opposed to the $700 \mu\text{A/lumen}$ reported by Martinelli (Ref. 12) and later by King (Ref. 14).

The work function changes of the activated surfaces were determined from the shifts in the retarding potential characteristics using the Farnsworth gun. Typical data is shown in Fig. 17. The cesiation to 1.2 monolayer coverage gave a work function shift of $\sim 3.35 \text{ eV}$. Although initial cesiation was non-uniform the fully cesiated surface was fairly uniform, with a work function variation of only 200 meV . Oxidation of the cesiated surface caused a further 0.65 eV drop in work function to give an overall change of $\sim 4.0 \text{ eV}$. The final value of the work function change had little correlation with the spectral yield achieved. A surface with a sensitivity of $< 10 \mu\text{A/lumen}$ gave a retarding potential characteristic identical (within 100 meV) to that obtained for a surface with a sensitivity of $200 \mu\text{A/lumen}$.

AES of the activated photocathode showed a very reproducible ratio of oxygen to cesium which gradually increased with increased sensitivity of the photocathode. (Oxygen KLL (505 eV) was between 0.75 and 1.05 of the cesium MNN (560 eV) doublet.) The ratio of the silicon LVV (91 eV) peak to the cesium ONN (47 eV) peak depended on the amount of cesiation and for the optimum photocathode was 0.7.

Photoelectron energy distributions from the negative electron affinity photocathodes showed a sharp low energy peak which, by comparison with an energy analysis of the dark current, could be identified as thermalized photoelectrons which have diffused towards the surface as thermal carriers (Fig. 18). This peak was present with energy distributions from surfaces represented by yields C, D, E, F, G and H in Fig. 16. Furthermore, work function measurements using the retarding potential characteristics indicated

a work function change of > 4.0 volts from the clean surface to the optimum photocathode (Fig. 17). If the clean surface has a work function of 4.6 eV (Ref. 16) then the work function of the cathode should be 0.6 eV. Both the observation of the thermalized photoelectrons and the low work function confirm that we have indeed a negative electron affinity photocathode.

It was also of prime interest in this study to determine the amount of cesium necessary for the optimum photocathode. Previous studies (Ref. 12,13,14) had used molecular cesium sources. The optimum photocathode was produced with an ion current of 2.2×10^{-7} amps (sample area was 0.4 cm^2) for 300 secs. A calculation assuming uniform deposition and a sticking probability of 1.0 suggests that the optimum coverage is 1.3 monolayers. [One monolayer here is defined with respect to the number of atoms in the unreconstructed Si(100) plane.] Activation of a surface with less cesium than one monolayer resulted in much inferior yields. The upper limit is somewhat uncertain, since oxygen contamination increased with increasing cesium coverage and this effect could be related to the observed decrease in sensitivity.

The stability of the activated cathode was good (studied over periods up to 60 hours) as long as care was taken in the initial activation. If the cesiated surface was activated with oxygen to the peak sensitivity (white light response) and then left for one hour the sensitivity would decrease. However, the photocathode could be reactivated to its original sensitivity with $\sim 10^{-8}$ Torr secs oxygen exposure [Typical initial oxygen exposures were $\sim 1 \times 10^{-7}$ Torr secs.] This photocathode would again decay in sensitivity but with a much longer time constant than previously and could be reactivated with oxygen. After three such cycles the photocathode was very stable with time. It was also of interest that if the photocathode was overexposed to oxygen (up to 3×10^{-7} Torr secs) during activation the resulting poor photocathode would recover with time. The recovery time was proportional to the degree of overexposure.

2.3.4 Discussion

In a state of negative electron affinity the vacuum level at the surface is below the bulk conduction band minimum. The electron emission process can be characterized as a diffusion process in which electrons produced in the conduction band quickly thermalize

and diffuse towards the surface as thermal carriers. The diffusion process is thus characterized by the minority carrier diffusion length L . If any band bending exists at the surface then the thermalized electrons have a probability of escape (B) through the bent band region into vacuum. On the basis of a simple model the yield is

$$Y = \frac{B\alpha}{(\alpha + L^{-1})} \quad \text{photoelectrons/absorbed electrons}$$

where α is the photon absorption coefficient. In the threshold region $L^{-1} \sim \alpha$

$$Y = B \cdot L$$

and at higher photon energies where $L^{-1} \ll \alpha$

$$Y \approx B$$

In the photon energy range above 2 eV (for silicon) α becomes much greater than L^{-1} and the yield is fairly constant providing a measure of the thermal electron escape probability. It can be seen from Fig. 16 that it is the thermal escape probability (B) that is changing as the surface become cleaner. It is also to B that we must turn to explain the deficiency of our photocathode with respect to that of Martinelli. Martinelli value of B was 18% whereas our value is only 8%. The value of the diffusion length (L) in both cases is $\sim 5\mu$.

For a negative electron affinity photocathode the thermal escape probability is a function of the electron affinity, the band bending width and uniformity of the surface. The electron affinity affects the escape probability in that it determines the surface barrier. Uniformity of the surface is essential for efficient collection of the low kinetic energy thermalized electrons. However perhaps the most important term is the band-bending width (w). The latter is a function of the difference in the position of the bands at the surface and in the bulk (V_{BB}) and the bulk doping concentration, i.e.

$$w = \frac{2e V_{BB}}{qN_A}$$

Thus for a fixed doping concentration, surface treatments could decrease the width (w) by decreasing the band bending

(V_{BB}) at the surface. This would cause B to increase as the width of the space charge region is directly related to w . Unfortunately, with a p-type sample of the high doping concentration employed it was impossible to employ photoelectric techniques to measure V_{BB} .

The observation that the work function of the activated photocathode was fairly independent of the sensitivity would suggest that the electron affinity was not the parameter responsible for the lack of sensitivity of some photocathodes. Evidence for non-uniformity of the activated photocathode can be seen in the retarding potential characteristic from the activated surface (Fig. 17). Increasing the collection field by an order of magnitude caused a slight increase in yield (~ 1.2) but not sufficient to account for any major discrepancies.

The only definite cause of a decreased sensitivity was oxygen contamination prior or during cesiation. This invariably caused a decrease in the sensitivity of the activated photocathode. Carbon contamination had a similar effect as did disordering at the surface. This observation has been explained by Levine as the blocking of effective cesium sites by the contaminant. This does not allow the optimum cesium/oxygen arrangement on the (100) surface and reduces the sensitivity. Levine (Ref. 15) suggests the lack of sensitivity is due to a higher work function and hence a higher surface barrier. The present data are not consistent with this interpretation since the work function of the activated surface was not a major parameter. It is felt that the postulated role of the contaminant in blocking cesium sites may be correct but that the mechanism responsible for decreased sensitivity is more complex.

2.4 A Study of Electron Scattering From Germanium (100)

Energy and angular distributions of the secondary electrons from a Ge(100) surface were obtained using the apparatus as shown in Fig. 19. A standard LEED electron gun was used with a directly heated tungsten ribbon as the electron source. The energy analyzer was a 127° cylindrical, electrostatic velocity selector which was rotatable through 55° about the scattering chamber. In addition the sample could be rotated about the primary electron beam axis. Primary electrons were incident on the sample surface at a fixed angle of 45° .

The intent of this study was to characterize the low energy electron scattering from a clean, well ordered surface. Thus care was exercised in assuring that these conditions pertained at

all times. Ion bombardment and annealing procedures were used to obtain and maintain clean, atomically ordered surfaces. Periodic checks of the surface cleanliness were made with Auger spectroscopy and the surface order was monitored continuously by LEED measurements. Degradation of either the surface order or cleanliness was found to alter the experimental results, indicating that the sample surface plays an important role in the scattering processes. The effect of surface ordering on the inelastic electron spectrum is illustrated by the curves in Fig. 20. Curve B is the inelastic spectrum for the case where the sample surface has been sputtered with 70eV argon ions and curve A shows the inelastic spectrum for the subsequently annealed surface. In the former curve there are characteristic loss peaks at 16.5eV and 7.5eV; the 16.5eV peak is due to excitation of a bulk plasma oscillation and the 7.5eV peak is felt to be associated with a loss mechanism involving argon ions embedded in the surface. In the case of the annealed surface there is a large increase in elastic intensity due to the diffraction of electrons and the inelastic spectrum intensity is also correspondingly larger, but in addition a number of new characteristic loss peaks appear at energies below the bulk plasmon loss. These losses are attributed to electron interband excitations and correlate reasonably well with the principal direct energy gaps determined from optical measurements. These interband loss peaks only appeared in the data when the surface was well ordered and then only in the immediate angular vicinity of the LEED beams.

As mentioned already, inelastic electron diffraction effects were the main cause of structure in the data. Inelastic peaks were observed that corresponded closely to the conditions that gave rise to elastic intensity peaks. This effect is illustrated by Fig. 21, where inelastic spectra are shown that were measured with the energy analyzer set in the position where an elastic intensity maximum was obtained for the (01) beam at $E_p = 36\text{eV}$. It can be seen that as E_p is raised above 36 eV an enhanced intensity region occurs in the inelastic spectrum centered about a secondary energy of 36 eV i.e. at $\Delta E = E_p - 36$ as indicated by the rightmost arrows in Fig. 21. This enhancement is the result of inelastic electrons with energies of 36 eV, which have been scattered from the primary electron beam, satisfying the same diffraction condition as the original 36 eV primary electrons. Also shown in the figure is a peak that remains fixed at a secondary energy of 23 eV (i.e. at $\Delta E = E_p - 23$). This corresponds to another strong (01) beam intensity maximum, but involves electrons scattered $\sim 10^\circ$ from the primary beam direction; more will be said about this particular peak later.

If the primary energy is fixed near a Bragg energy and the detector angle is varied about the diffraction beam then the inelastic diffraction effects give rise to strong asymmetries in the measured inelastic intensity for opposite angular deflections in the plane of incidence. Measurements made about the (00) diffraction beam are shown in Fig. 22, where the primary energy of 120 eV corresponds to a (00) beam Bragg energy. It may be observed that as the detector is moved toward the surface normal (+2°) the inelastic spectrum becomes much larger while the opposite detector deflection gives a reduction in inelastic intensity. This behavior can be accounted for by an inelastic diffraction process which obeys the same kinematical Bragg condition as the 120 eV elastic maximum. The scattering conditions for these particular spectra are illustrated in Fig. 23. For a +2° deflection, electrons with energies of about 110 eV can satisfy a Bragg scattering condition and this accounts for the increased intensity centered about $\Delta E = 10$ eV. For the opposite angular deflection, however, none of the electrons have sufficient energy to satisfy a Bragg condition and so the intensity is lower.

A similar analysis can be applied when the primary energy is raised to 130 eV. For this primary energy the elastic electrons no longer satisfy a Bragg relation but electrons which lose 10 eV energy and scatter in the forward direction can satisfy the Bragg condition and as shown in Fig. 24 this gives rise to increased intensity around $\Delta E = 10$ eV as measured in the (00) beam direction. The wave vector diagram depicting this scattering process as well as for the other two spectra is shown in Fig. 25. When the detector is displaced by +2° the Bragg relation is satisfied for electrons with 117 eV energy and this gives rise to the enhancement in intensity in the vicinity of $\Delta E = 13$ eV. As before, when the detector is displaced by -2° none of the electrons are energetic enough to satisfy the Bragg condition leading to the relatively weak inelastic spectrum.

Angular distributions of the inelastic electrons also show a pronounced effect of inelastic diffraction. Figures 26 and 27 show the angular intensity plots measured in the plane of incidence for a loss energy of 10 eV. The angle θ in these figures is measured relative to the surface normal and the dots on the curves indicate the locations of the (00), (0 1/2), (01) and (0 3/2) diffraction beams; the (00) beam being located at $\theta = 45^\circ$. It can be seen that there is the equivalent of a diffraction pattern for the inelastic electrons but the peaks are shifted somewhat from the LEED beam positions. For the (00) beam, there are elastic

intensity maxima at 77 eV and 120 eV, whereas the inelastic intensity near the (00) beam maximizes for primary energies of about 87 eV and 120 eV. This indicates that the predominant process in the former case is one of energy loss before diffraction while in the latter case it is one of diffraction before energy loss. In the case of the (01) diffraction beam the loss before diffraction process can be seen by the increased inelastic intensity at $\theta \approx 26^\circ$ for the 130 eV curve. This corresponds to an elastic intensity maximum around 120 eV for the (01) diffraction beam.

Measurements of the low energy secondary electron energy distributions (SED's) also indicated structure related to diffraction of the secondary electrons. Figure 28 shows the SED's measured in the specular scattering (i.e. (00) beam) direction. The peaks which occur at 3.5, 6.0 and 11.5 eV all correlate with elastic intensity maxima for the (00) diffraction beam, and are localized to the specular direction. Also, the peaks tend to be sharpest when the primary energy is near to the peak energy as would be expected for a diffraction process. Similar measurements made in the direction of the surface normal are shown in Fig. 29. Two peaks are found in this data, one at about 9 eV and the other at 21.5 eV. The latter peak corresponds to a very strong (01) diffraction beam intensity maximum that occurs at 21.5 eV and appears normal to the surface. The other peak seems to be related to diffraction of inelastic electrons directed normal to the sample surface. Elastic intensity measurements made normal to the surface show an intensity maximum at about 8.5 eV, in agreement with this idea. Measurements of the variation of peak energy with detector angle for these two peaks were compared with calculations based on the two assumed diffraction conditions and the results are shown in Fig. 30; the wave vector diagrams for each case are shown at the bottom of the figure. In each case the agreement between measured and calculated energies is reasonably good, giving confidence in the diffraction model for these peaks. In referring to Fig. 21, the peak at about 23 eV was mentioned previously as being due to a (01) diffraction condition. This peak is the same as the one described by the right hand curve of Fig. 30.

2.5 Auger Spectra of Cleaved Alkali Halides

2.5.1 Experimental Procedure

All experiments were carried out in an ultra-high vacuum system. The optical quality samples of LiF, NaCl, NaBr, KCl, KBr, KI and RbI were obtained from Semi-Elements Inc. already cleaved to 5mm x 5mm x 15mm

along (100) planes. In order to accomplish repeated vacuum cleaving of the crystal a special sample holder was constructed (Fig. 31). The sample was held by a cradle which rested on a knife edge, thus allowing uniform support of the sample. The sample was clamped into place with a lever by turning the clamping nut. To allow for initial outgassing of the sample holder and to provide for possible elevated temperature studies, one half of a type BEJ 200 W projection lamp filament was installed in a 6mm diameter cavity in the holder. The cleavage apparatus was a tungsten knife mounted on a 8-32 stainless steel threaded rod and suspended from a stainless steel auxiliary bellows mounted on the manipulator flange. For cleavage the blade was placed on the sample and the bellows assembly sharply tapped. The cleavage face was in general of good quality with few steps.

The AES apparatus was a 4-grid conventional LEED system operated in the manner described by Weber and Peria (Ref. 18).

2.5.2 Dissociation and Surface Charging

In obtaining the characteristic Auger spectra of insulating compounds such as the alkali halides, two additional problems arise that are not present for conducting or semiconducting materials.

The first of these problems is dissociation of the sample near the surface exposed to the electron beam. O'Bryan and Skinner (Ref. 19) observed that the decomposition of alkali halides in the presence of an electron beam resulted in the evolution of a halogen gas and accumulation of alkali metal near the surface. They also observed that the decomposition was most severe for small, mobile ions, such as in LiF.

In early attempts to obtain Auger spectra of some alkali halides with a focussed electron beam (less than 1 mm diameter) dissociation was evident. After a short time from the initiation of the electron beam (about 1 minute), the spectrum would suddenly break up, the lock-in amplifier (phase-sensitive detector) would indicate an overload condition at the input, and the phosphor-coated collector of the LEED chamber would display relatively bright, amoeboid patterns. Furthermore, the originally transparent crystal had a sharply-defined, opaque spot, usually white or light gray, on the cleaved surface that was the same diameter as the electron beam. Exposing the sample to air caused the spot to disappear leaving only a very faint outline.

Since the time before the onset of serious decomposition was lengthened by using small electron beam currents and low electron energies, a primary beam energy of 1000 eV and beam currents of 10 microamperes or less (approximately 1.5 microamperes for LiF) were used whenever possible. Furthermore, the electron beam was intentionally defocused to approximately 2 mm diameter in order to reduce the beam current density. With these precautions, Auger spectra of the alkali halide sample could be obtained without significant decomposition. Long exposure times (usually one hour or more) were needed to produce a noticeable spot on the sample surface. The same precautions, however, made it necessary to use sinusoidal modulating voltages as high as 10 volts peak-to-peak to observe the Auger signals, thus reducing resolution. In some cases, weak signals from expected transitions could not be detected at all.

The second of the problems encountered in obtaining Auger spectra of alkali halides is peculiar to insulating samples, viz. charging of the sample surface due to a secondary electron yield (the number of secondary electrons emitted per incident electron) different from unity. At a primary energy of 1000 eV, the secondary yield is near its maximum value of 5.5 to 7.5 for alkali halides (Ref. 20). The sample surface will charge positively until, at a potential nearly that of the inner grid, a sufficient number of the slower secondary electrons are returned to the sample to reduce the effective yield to unity. The surface charging, can thus be adjusted by the potential on the inner grid.

2.5.3 Auger Spectra

2.5.3.1 Lithium

Since the lithium atom (atomic number 3) has two K electrons and one L_I electron, the only possible Auger transition would be the result of the ionization of the K level with neutralization and ejection from the valence bond formed by pooling the L_I electrons of the metal. The common designation for such a Auger transition would be KVV, where the first letter designates the originally ionized level, the second letter designates the level from which the neutralizing electron originates, and the third letter designates the origin of the electron ejected into the vacuum and detected. An isolated lithium atom can not have any characteristic Auger peaks since the transition proposed above for the lithium metal (KVV) would be designated $KL_I L_I$. However, the one electron in the L_I level cannot both neutralize the ionized K level and be ejected into the vacuum. Similarly, the characteristic Auger spectrum of the lithium ion in a lithium halide crystal must contain no peaks since the single lithium L_I electron has been transferred to the halogen.

As expected, the Auger spectrum of vacuum-cleaved lithium fluoride (LiF) contains no peaks attributable to the Li^+ ion. However, exposure to a 1000 eV, 1.3 microampere primary electron beam with the sample holder heated to 175°C for approximately 90 minutes resulted in a peak at a retarding voltage of 49 volts. This peak was due to the metallic lithium which resulted from the dissociation of the LiF. All peak locations quoted refer to the retarding voltage at which the largest negative excursion of $\frac{d(N(E))}{dE}$ occurred, adjusted to account for the work function of the collector.

2.5.3.2 Fluorine

Since fluorine (atomic number 9) has essentially the same electronic structure as oxygen (atomic number 8), the fluorine Auger spectrum was expected to be similar to that of oxygen, a common surface contaminant. Thus, the transitions predicted were those involving an ionized K level with neutralizing and ejected electrons originating from some combination of L_{II} and L_I levels.

In obtaining the Auger spectrum due to the F^- ion in vacuum-cleaved LiF, it was necessary to minimize incident beam current density, primary voltage, and exposure time. The primary beam was defocussed to 2 mm diameter and a relatively large (10 volts peak-to-peak) modulating voltage was used. Even with the primary beam current reduced until the fluorine Auger signal was barely distinguishable from the background noise ($I_p = 1.5$ microamperes), the signal could be maintained for only 15 minutes.

Probably due to the relatively small primary current only one fluorine Auger peak was detected. The energy observed for this peak within one minute after the primary beam was turned on, taking into account the 5 eV work function of the grids, was 652 eV. However, the location of the fluorine peak shifted to a maximum of 655 eV before disappearing into the background noise. The shift and disappearance of the fluorine signal is attributed to severe dissociation of the sample and subsequent evolution of fluorine due to the primary electron beam.

Since the $KL_{II}L_{II}$ Auger transition is the most prominent in the oxygen spectrum and since this transition involves only the more populated L_{II} level (6 electrons in the F^- ion) instead of the L_I level (2 electrons), the only observed fluorine peak is undoubtedly due to a $KL_{II}L_{II}$ transition. The observed energy, taking into account the work function of the retarding grids, is compared in Table 2 to that calculated from X-ray data (Ref. 21).

TABLE 2

F and F⁻ Transition Energies

Fluorine Transition	Atomic (calculated) (eV)	LiF (observed) (eV)
KL _{II} L _{II}	668	652
KL _I L _{II}	646	
KL _I L _I	624	

2.5.3.3 Sodium

Since the electronic structures of the F⁻ ion and Na⁺ ion are identical, it is reasonable to expect the Auger spectra to be similar. The Auger spectrum observed for the Na⁺ ion in vacuum-cleaved NaBr and NaCl showed only two high energy peaks. The expected peak due to the KL_IL_I transition could not be distinguished from the background noise. The observed energies of these peaks, taking into account the work function of the retarding grids, are compared in Table 3 to energies calculated using X-ray (Ref. 21) data for the atomic Na.

TABLE 3

Na and Na⁺ Transition Energies

Sodium Transitions	Atomic (calculated) (eV)	NaBr (observed) (eV)	NaCl (observed) (eV)
KL _{II} L _{II}	1010	996	996
KL _I L _{II}	978	956	956
KL _I L _I	946		

Although not as serious a problem as in the case of LiF, the dissociation of NaBr and NaCl from exposure to the electron beam can be observed by the gradual appearance of a small peak at an energy of 31 eV ($V_{ret} = 26$ volts) characteristic of metallic sodium. This peak is either a $L_{IV} V$ or $L_{III} L_I V$ transition, which, using X-ray data, (Ref. 21) would yield Auger peaks at 31 eV and 32 eV respectively. The pool of electrons forming the valence band are not available for Na^+ since the single M_I electron was removed. Therefore, these transitions are not possible in the ionic spectrum. The very close agreement between the observed location of the 31 eV metallic peak and that calculated from X-ray data supports the conclusion that charging of the sample surface is negligible for $V_{GT} = 0$.

2.4.3.4 Chlorine

The Auger spectrum observed for the Cl^- ion in both NaCl and KCl consisted of three peaks involving the ionization of the L_{II} level. Although a 1.6 eV splitting of this level into L_{II} and L_{III} was observed for atomic chlorine in X-ray data (Ref. 21), this splitting was not observed in the Auger spectra. No peaks involving the L_I level were observed. The observed energies of the Cl^- peaks, taking into account the work function of the retarding grids, are compared in Table 4 to energies calculated from X-ray data (Ref. 21) for atomic chlorine. The value used for the energy of the split $L_{II,III}$ level was the average of the tabulated energies.

TABLE 4

Chlorine Transitions	Cl and Cl^- Transition Energies		
	Atomic (calculated)	NaCl (observed) (eV)	KCl (observed) (eV)
$L_{II} M_{II} M_{II}$	187	176	180
$L_{II} M_I M_{II}$	177	162	165
$L_{II} M_I M_I$	166	154	156

2.5.3.5 Potassium

Since the Cl^- ion and the K^+ ion have the same electronic structure, it is expected that their Auger spectra would be similar.

The spectra observed for the K^+ ion in KCl, KBr and KI all consist of three peaks involving ionization of the L_{II} level. Although a 3 eV splitting of this level into L_{II} and L_{III} was reported for atomic potassium in the X-ray Table (Ref. 21) no attempt was made to split the ionic Auger peaks. No peaks involving the L_I level were observed. The observed energies of the K^+ peaks, taking into account the work function of the retarding grids, are compared in Table 5 to the energies calculated from X-ray tables (Ref. 21) for atomic potassium and to the observed energies of atomic potassium peaks for one-fourth monolayer of potassium on indium. The value used for the energy of the split L_{II}, L_{III} level was the average of the tabulated energies.

TABLE 5

K and K^+ Transition Energies

Potassium Transitions	Atomic (Calc.) (eV)	Atomic (Obs.) (eV)	KCl (Obs.) (eV)	KBr (Obs.) (eV)	KI (Obs.) (eV)
$L_{II} M_{II} M_{II}$	259	259	250	250	249
$L_{II} M_I M_{II}$	243	241	230	230	231
$L_{II} M_I M_I$	227	227	218	217	216

2.5.3.6 Bromine

The Auger transitions observed for the Br^- ion in both NaBr and KBr consist of low energy peaks from the ionization of the split M_{II}, M_{III} level and the M_{IV} level. Auger peaks due to the ionization of the deep-lying L_{II}, M_{III} (approximately 1550 eV below the Fermi level) could not be observed. While the transition identification in the NaBr and KBr spectra is not entirely obvious, the system presented is the only one consistent with the spectra of both Br^- and Rb^+ (Section 2.5.3.7, same electronic structure as Br^-) that yielded reasonable ionic energy levels for both ions. The observed energies of the Auger peaks, taking into account the work function of the retarding grids, are compared in Table 6 to energies calculated from X-ray data (Ref. 21) for atomic bromine.

TABLE 6

Br and Br⁻ Transition Energies

Bromine Transitions	Atomic (calculated) (eV)	NaBr (observed) (eV)	KBr (observed) (eV)
M _{II} M _{IV} N _{II}	115	103	104
M _{III} M _{IV} N _{II}	107	96	98
M _{II} M _{IV} N _I	93	89	
M _{III} M _{IV} N _I	85	84	
M _{IV} N _{II} N _{II}	60	51	52
M _{IV} N _I N _{II}	37	38	40
M _{IV} N _I N _I	15		

2.5.3.7 Rubidium

Since the Br⁻ ion and the Rb⁺ ion have the same electronic structure, it is expected that their Auger spectra would be similar. The spectra of vacuum-cleaved RbI consists of low energy peaks from the ionization of the split M_{II,III} level and the M_{IV} level. Auger peaks due to the ionization of the deep-lying L_{II,III} level (approximately 1800 eV below the Fermi level) could not be observed. The observed energies of the Auger peaks, taking into account the work function of the retarding grids, are compared in Table 7 to energies calculated from X-ray data (Ref. 21) for atomic rubidium.

TABLE 7

Rb and Rb⁺ Transition Energies

Rubidium Transitions	Atomic (calculated) (eV)	RbI (observed) (eV)
$M_{II}M_{IV}N_{II}$	122	108
$M_{III}M_{IV}N_{II}$	113	100
$M_{II}M_{IV}N_I$	107	
$M_{III}M_{IV}N_I$	98	
$M_{IV}N_{II}N_{II}$	82	72
$M_{IV}N_I N_{II}$	67	54
$M_{IV}N_I N_I$	52	

2.5.3.8 Iodine

The Auger transitions observed for the I⁻ ion in both KI and RbI consist of two low energy peaks due to the ionization of the N_{IV} level and a series of weaker peaks at higher energies from the ionization of the split M_{IV,V} level. No peaks due to ionization of the deeper M_I, M_{II}, or M_{III} levels were observed. Although the use of higher primary electron beam energies would have most likely increased the ionization efficiency (Ref. 22) of the M_{IV,V} level (approximately 520 eV below the Fermi level) and resulted in larger high energy peaks, a primary energy of 1000 eV was used along with a beam defocused to 2 mm to minimize dissociation. The M_{IV,V}N_{II}N_{IV} and M_{IV,V}N_IN_{IV} doublets were sufficiently weak that their splitting could not be resolved. The observed energies of the I⁻ Auger peaks, taking into account the work function of the retarding grids, are compared in Table 8 to energies calculated from X-ray data (Ref. 21) for atomic iodine.

TABLE 8

I and I⁻ Transition Energies

Iodine Transitions	Atomic (calculated) (eV)	KI (observed) (eV)	RbI (observed) (eV)
$M_{IV}N_{IV}N_{IV}$	532	519	519
$M_{V}N_{IV}N_{IV}$	521	509	509
$M_{IV}N_{II}N_{IV}$	459		
$M_{V}N_{II}N_{IV}$	448		432
$M_{IV}N_{I}N_{IV}$	395		
$M_{V}N_{I}N_{IV}$	384		362
$N_{IV}O_{II}O_{II}$	43	35	35
$N_{IV}O_{I}O_{I}$	22	18	18

2.6 The Use of Auger Electron Spectroscopy for the Chemical Analysis of Solutions

As previously stated, this investigation had a twofold purpose, viz., the development of means of quantifying the Auger method and the evaluation of Auger spectroscopy as a means of analyzing aqueous solutions. Since both objectives require the quantitative transfer of the species of interest to a substrate, considerable effort was devoted to this aspect. Three methods were employed, all of which are discussed separately in the following sections.

Throughout the investigation attention was focused on a particular system, viz. Ag on Au. The silver solutions were prepared by first dissolving a known weight of AgNO₃ in distilled water and then performing dilution in several stages until the desired concentration was attained.

2.6.1 Adsorption from Solution

This method depends on the fact that, when a metal is immersed in an aqueous solution, an equilibrium will be established between the competing processes of cation adsorption on the substrate, and cation return to solution. Standard volumes (~ 1 ml.) of known concentration of AgNO_3 in distilled water were prepared. A preliminary experiment indicated that the equilibrium surface Ag concentration was achieved within a few minutes of the time of substrate immersion. By dipping several substrates in turn in the same container of solution, it was determined that, for the solution volume and substrate area employed, approximately one-half of the silver ions remaining in solution were adsorbed on each immersion. After several substrates had been dipped in this way no further adsorption occurred, i.e., all the Ag ions had been removed from solution.

The original plan assumed that, providing the surface Ag concentrations were in the submonolayer range, the Auger signal would be proportional to the concentration. Thus the sum of the Auger signals from the several substrates would correspond to a surface concentration readily calculable from the initial, known, solution concentration. None of the data obtained contradicted this assumption. However, it was observed that the Ag Auger signal obtained from the first substrate dipped in solution of a given concentration could vary by as much as a factor 4 among attempts. The signal was smaller the larger the substrate contamination level.

There are two possible interpretations which can be made from the above result. First, the contamination level no doubt influences the equilibrium Ag surface concentration. This effect, by itself, would not invalidate the method, since we depend only on eventually extracting all of the Ag from solution onto whatever number of substrates is required. The second possibility however is that the lack of reproducibility on a single dip is due to the "dilution" effect of the contaminant. The latter effect occurs because the Auger signal is generated only in the top several atomic layers of the specimen. If a substantial fraction of the atoms in these layers are not Ag, the Ag signal will be reduced accordingly.

Of course the dilution effect can occur in any case, independent of the method of deposition used, but it will be most detrimental to the adsorption method where each of several substrates holds only a fraction of the Ag to be determined. For this reason the method was abandoned, although further work would be desirable. For example, the method might present some advantages in the analysis of multicomponent systems for a specific component, if a substrate can be found on which preferential adsorption of the desired component occurs.

2.6.2 The Electroplating Method

Silver was electroplated from AgNO_3 solutions, prepared as previously described, onto Au substrates. Again, deposition onto several substrates from the same container of solution ensured that all Ag was removed. The substrates were supported horizontally so that only one side contacted the solution. The surface Ag concentration was found to be very non-uniform, being small in the center and large on the edges. This deposition method was abandoned. Later it was discovered that gas bubbles collecting under the substrate had caused a nonuniform current density. Thus the method may still have potential, provided that the substrates are maintained vertical during the electroplating procedure.

2.6.3 The Solvent Evaporation Method

Most of the work on this phase of the project was carried out by allowing a drop (known-mass) of aqueous solution of known Ag concentration to dry on a precleaned substrate. Since preliminary work showed that the resulting surface concentration of Ag was uniform (on a macroscopic scale), the method leads in a straightforward way to a calibration curve (Fig. 32). Here the magnitude of the major Ag Auger peak (360 eV) is plotted against the Ag concentration expressed in monolayers equivalent (i.e., as if the Ag were present in metallic form and contamination-free). The conditions of measurement are, of course, identical for all points on the curve.

Figure 32 also shows the Auger signal levels obtained from clean bulk Ag and from a substrate carrying a large Ag concentration (100 monolayers equivalent). That the saturation which appears to be approached by the curve falls short of the former is understandable, in terms of the "dilution" effect of the NO_3^- ions. But the extremely slow approach to saturation (if any) and the low value of the latter both suggest that dilution of the solute by unavoidable contamination is a problem. Indeed the Auger spectrum (Fig. 33) shows that substantial contamination, presumably present in the water used, exists.

Figure 34 shows that, for low Ag concentrations, the calibration curve is linear as expected. However, because of the dilution effect the slope shown must be regarded as a lower limit.

A further demonstration of the importance of the solute dilution effect is provided by Fig. 35 which is the Auger spectrum corresponding to Minneapolis tap water with a known concentration of Ag. Also shown on the figure is the Ag peak height which would have been measured for the same concentration of Ag in distilled water.

Even though the dilution effect affects the sensitivity of detection of a given species, the analysis can still be made quantitative by the use of internal standards. For example, if the spectrum shown in Fig. 35 (including the Ag peak) were to correspond to our unknown, we could determine its Ag concentration by adding known amounts of Ag to it and observing the effect on the Ag Auger peak height.

2.7 A System for Studying Complex Photocathodes

2.7.1 The Vacuum System

The system for the study was developed under this contract and under another contract. The system is a 12" Ultek stainless steel vacuum system with rough pumping facilities (two sorption pumps) and a 200 liter sec^{-1} ion pump. System pressures below 2×10^{-10} Torr were routinely obtained and maintained. A quadrupole (EAI 150) mass spectrometer was used to analyze the gaseous content of the system both residual and during film formation. The system was equipped with a cylindrical analyzer for determining the chemical composition at the surface by monitoring characteristic Auger electrons. A three-grid hemispherical photoelectron analyzer (Ref. 9) was employed for determining the spectral yield and the energy distribution of photoelectrons. A flange-mounted film deposition chamber was constructed capable of forming alkali antimonide films.

2.7.2 Cylindrical Analyzer for Auger Spectroscopy

A cylindrical analyzer was employed to determine the energies of electrons backscattered from the electron bombarded sample. A diagram of the cylindrical analyzer is shown in Fig. 36; its operation and application in Auger spectroscopy has been described in some detail by Palmberg (Ref. 22). Changing the inter-cylinder bias of the analyzer changed the allowed energy of electrons collected by the electron multiplier. Hence a sweep was made through the range of electron energies of interest. In the normal fashion, use of ac modulation of the bias and phase sensitive lock-in techniques to monitor the multiplier output produced a plot of the derivative of the electron energy distribution as a function of electron energy.

2.7.3 Film Deposition

A flange mounted chamber for deposition of alkali antimonide films was constructed for use in this study (Fig. 37). Moving the substrate into the deposition position prevented the escape of sample constituents from the chamber during film deposition. A tungsten filament was a source of white light used to monitor the

light transmission of the initial antimony layer and to monitor photoemission during subsequent constituent deposition.

Current to the alkali dispensers or Sb evaporator was controlled manually. A Pt-Pt+10%Rh thermocouple installed inside the deposition chamber close to the front of the substrate, and another placed on the back of the substrate, were used to determine substrate temperatures due to operation of the heater ring and/or the constituent sources. The original Sb deposition was made at room temperature. Depositions of the alkali metals and subsequent Sb depositions were made as follows: K, 160°C and 25°C; Na, 220°C and 25°C, Cs, 160°C and 25°C; and Sb, 60°C and 25°C. Sources of Na, K and Cs were ordinary commercial dispensers containing the alkali metals in compound form sealed in a metal tube. Resistive heating of the dispenser opened a crack in the metal tube wall and allowed action of a reducing agent in the dispenser to release the alkali metal in vapor form from the original compound. The crack in the dispenser tube was oriented to have line of sight position with respect to the sample. The dispensers used were manufactured by SAES Getters of Milano, Italy. Specific information about the composition and manufacture of the dispenser was considered proprietary information by the manufacturer.

Source of the antimony was very pure bulk antimony which was ground from large crystal form into fine powder just before placement in an evaporator. The Sb evaporator was constructed of tantalum metal. Orientation of the opening in the Sb cup in the evaporator was line-of-sight to the sample position. The Sb evaporator and the alkali metal dispenser were hot enough to glow red during their depositions. The alkali dispensers required 7.5 amperes maximum and the Sb evaporator 20 amperes for operation.

A flange-mounted sample manipulator was constructed for this study with facilities for vertical motion of 4 cm and a rotation of $\pm 180^\circ$. The substrates were either clear glass with contact electrodes (aluminum) deposited upon them or tantalum sheet.

2.7.4 Results

The apparatus was tested and found to operate satisfactorily. Five Na₂KSb[Cs] films were attempted. No film comparable to commercially produced S-20 photocathodes was obtained. The alkali metals were found to react with the Sb layer (and subsequent compounds) at 25°C as well as at the normally-used elevated temperatures. There was no definite evidence of a reaction temperature which was optimum with respect to the resulting photoyield.

The alkali channel dispensers were found to generate large quantities of CO during operation. On some occasions chlorine was also observed. Extensive outgassing procedures were developed to reduce this gas generation during cathode activation.

The main purpose of the investigation was the correlation of surface chemical composition and photoelectric efficiency. This objective has, however, so far been thwarted by sample inhomogeneities and damage to the surface by the probe electron beam used in AES.

SECTION III

CONCLUSIONS AND SUGGESTIONS FOR FURTHER STUDY

3.1 Deposition of High Energy Alkali Ions on Semiconductor Surfaces

The energy dependence of the zero coverage sticking probability was measured for the Ge(100)-Cs system using Auger electron spectroscopy. A faster than linear dropoff was observed in the 0-200 eV range, varying from unity at 2 eV to approximately 0.7 at 200 eV incident ion energy. The proposed measurement of structural damage using specular electron reflectivity was not attempted because of deposition nonuniformity. The experiment has been suspended until techniques are developed for highly uniform alkali ion deposition.

3.2 A Study of the Cesium-Oxygen Overlayer on Germanium

A preliminary investigation of the Ge(100)-Cs-O system has been completed and an optimization procedure has been established which consistently results (for an intrinsic sample) in a photoelectric threshold of $1.20 \pm .10$ eV and a work function of $0.95 \pm .15$ eV. The procedure consists of oxidizing a Cs-saturated layer which has been deposited on the clean surface. The role of the oxygen is uncertain, but a strong ordering of the Cs layer is observed during oxidation. Oxygen contamination of the clean surface was found to degrade the ultimate photoelectric response. Also any heating of the Cs layer was observed to produce irreversible structural changes which inhibited optimization. These structural changes may occur to some extent at room temperature, the temperature at which the cathode is formed.

A more complete photoelectric study of the surface should be pursued using photoelectric energy distribution measurements. The inclusion of a molecular source for Cs deposition is desirable, allowing uniform, oxygen-free layers to be formed. The uniformity would permit a more definitive study of the cathode formation process.

3.3 The Silicon Negative Electron Affinity Photocathode

The study of the activated silicon (100) photocathode showed that a clean well-ordered surface is essential for an efficient photoemitter. The negative electron affinity surface produced in this study had a sensitivity of $320 \mu\text{A lumen}^{-1}$ as compared to that of Martinelli of $700 \mu\text{A lumen}^{-1}$. Analysis of the data showed that the most important parameter was the escape probability of the thermalized electrons. This parameter is very sensitive to band bending, in particular to the width of the space charge region. The study showed

that the work function of the activated surface was ~ 0.6 eV and that ~ 1.2 monolayers of cesium ($\sim 9 \times 10^{14}$ atoms cm^{-2}) were present on the optimum photocathode.

Although use of a p^{++} sample is essential for observing the negative electron affinity photocathode the use of such heavy doping and the small band bending region severely limits the interpretation of data. Of prime interest would be to determine the amount of band bending at the surface of the photocathode. The normal technique for this purpose is the use of the high energy edge of the photoelectron energy distributions to determine the position of the valence band maximum at the surface. Unfortunately, in the case of the negative affinity cathode, photoemission from this edge is masked by emission from the bulk.

Two solutions to this dilemma appear to be available. One involves the measurement of the energy distributions of secondary electrons excited by low-energy primaries. Such primaries should not penetrate the space charge region substantially and thus the highest energy secondaries should be those excited from the valence band maximum at the surface. Shifts in such distributions should reveal changes in band bending as was the case for the photoelectron distributions used in Sections 1.8 and 1.9.

A second possibility is to repeat the photoelectric work using higher resistivity material. In such a case the space charge thickness is sufficient so that surface and volume contributions to the valence band emission can be distinguished.

Having determined the nature of the band bending extant in current cathodes, surface treatments which will ensure a more suitable bending should be sought. As discussed by Riach (Ref. 3) the best condition would be no band bending, i.e., the flat band condition. It is thus proposed that surface treatments, (possibly deposition of submonolayer quantities of "impurities") prior to activation, be studied. The information and processing technique gained from such studies of the near-intrinsic material would then be applied to degenerate p-type material.

3.4 A Study of Electron Scattering from Ge(100)

Low energy electron scattering measurements were carried out on a clean, atomically ordered Ge(100) surface for primary energies below 150 eV. These measurements indicated that the major cause of structure in the inelastic electron energy and angular distributions was the diffraction of inelastic electrons. In some instances the

behavior was accountable by applying kinematical diffraction conditions to the inelastic electrons. Surface cleanliness and atomic ordering was necessary for the observation of any inelastic structure as expected when electron diffraction is involved in the scattering process.

3.5 Auger Spectra of Cleaved Alkali Halides

The purpose of the study, the characterization of the Auger spectra of the alkalis was achieved. Two difficulties in using insulators such as the alkali halides were overcome. The first, that of electron beam dissociation, was minimized by minimizing primary current and diffusing the electron beam to cover a large area on the sample. The second, that of the surface charging of an insulator due to a secondary emission yield different from unity was controlled by the potential on the inner grid of the four-grid LEED apparatus.

3.6 The Use of Auger Spectroscopy for the Chemical Analysis of Solutions

The most straightforward means of making a quantitative transfer of the unknown from solution is by the solvent evaporation method. From the point of view of absolute calibration, however, cleaner water than was available to us should be used. In fact the use of cleaner water would be desirable for all three methods and should be investigated.

For the analysis of real water samples for a specific constituent, further investigation of the adsorption and electroplating methods should be carried out. Of particular interest would be to determine whether the element of interest could be selectively deposited on the substrate by suitably choosing the conditions i.e., the adsorption time and temperature, and the nature of the substrate.

3.7 A System for Studying Complex Photocathodes

This portion of the program was unsuccessful in that the expected correlations between surface chemical composition and photoelectric efficiency were not observed. The failure is believed to be related to deficiencies in the processing procedure and to damage of the surface by the probe electron beam. Solutions to both problems are now apparent and progress in this area may still be possible.

REFERENCES

1. W.T. Peria, Physics of Electron-Electron and Electron-Photon Interaction, AFAL-TR-69-177, Contract No. AF33615-3561, April 1969.
2. H.S.W. Massey and E.H.S. Burhop, Electronic and Ionic Impact Phenomena, Oxford (1952).
3. G.E. Riach, Photoemission Studies of the Alkali Covered Germanium (111) Surface, AFAL-TR-71-235, Contract Nos. F33615-69-C-1053 and AF33615-3561, March 1971.
4. D.E. Anderson, A.B. Laponsky, and W.T. Peria, Research in Physics of Electron Emission and Electron Tube Technology, Contract No. AF33657-10475, October 16, 1962 to October 15, 1965, Vol. III.
5. R.J. Zollweg, J. Appl. Phys. 34, 2590 (1963).
6. R.L. Erickson, University of Minnesota, Private communication.
7. J.J. Lander and J. Morrison, J. Appl. Phys. 34, 1403 (1963).
8. R.E. Schlier and H.E. Farnsworth, J. Chem. Phys. 30, 917 (1959).
9. R.E. Weber and W.T. Peria, Surf. Sci. 14, 13 (1969).
10. M.R. Jeanes and W.M. Mularie, A Photoelectric Study of Clean and Cesium Si(100) and Ge(100), AFAL-TR-72-242, Contract Nos. F33615-69-C-1053 and AF33615-3561, August 1972.
11. J.J. Uebbing and L.W. James, J. Appl. Phys. 41, 4505 (1970).
12. R.U. Martinelli, Appl. Phys. Letts, 16, 261 (1970).
13. R.U. Martinelli, Conf. on Photoelectric and Secondary Electron Emission, Minneapolis, Minn., August 1971.
14. King, Physical Electronics Conference, Washington, D.C., March 1971.
15. J. Levine, RCA Laboratories, private communication.
16. M.R. Jeanes and W.M. Mularie, A Photoelectric Study of Clean and Cesium Si(100) and Ge(100), AFAL-TR-72-242, Contract Nos. F33615-69-C-1053 and AF33615-3561, August 1972.

17. L. Cordes, Ph.D. Thesis, University of Minnesota, 1967.
18. R.E. Weber and W.T. Peria, J. Appl. Phys. 38, 4355 (1967).
19. H.M. O'Bryan and H.W.B. Skinner, Proc. Roy. Soc. A, 176, 229 (1940).
20. H. Bruining, Physics and Applications of Secondary Electron Emission, McGraw-Hill, N.Y. (1954).
21. J.A. Bearden, X-ray Wavelengths and X-ray Atomic Energy Levels, NSRDS-NBS 14, (1967).
22. P.W. Palmberg, Appl. Phys. Letters 13, 183 (1968).
23. P.W. Palmberg and W.T. Peria, Surface Science 6, 57 (1967).
24. P.W. Palmberg, J. Appl. Phys. 38, 2137 (1967).
25. J.M. Chen, Ph.D. Thesis, University of Minnesota (1968).
26. F.G. Allen and G.W. Gobeli, Phys. Rev. 144, 558 (1966).
27. T.E. Fischer, Surface Science 13, 30 (1969).
28. T.E. Fischer, F.G. Allen and G.W. Gobeli, Phys. Rev. 163, 703 (1967).
29. T.E. Fischer, Helv. Phys. Acta 41, 487 (1968).
30. R.E. Eden, Technical Report No. 5221-1, Solid State Electronics Laboratory, Stanford University (1967).
31. J. van Laar and J.J. Scheer, Philips Res. Rept., 17, 101, (1962).
32. J.R. Arthur, Jr., Surface Sci. 2, 289 (1964).
33. (a) W.B. Shepherd, An Observation of Surface State Emission in the Energy Distribution of Electrons Field Emitted from Ge(100), AFAL-TR-71-268, Contract No. F33615-69-C-1053, October, 1971.
(b) D.P. Smith, A Study of Surface States on Ge(111) Using Field-Electron Emission, AFAL-TR-72-241, Contract No. F33615-69-C-1053, July 1972.
34. H.D. Hagstrum, Phys. Rev. 150, 495 (1966).
35. H.D. Hagstrum, Phys. Rev. 96, 336 (1954).
36. H.D. Hagstrum, Phys. Rev. 122, 83 (1960).

37. H.C. Feng, "An Ion Neutralization Study of Sodium Covered Ge(111)", AFAL-TR-72-296, Contract No. F33615-69-C-1053, August 1972.
38. R.E. Weber and W.T. Peria, J. Appl. Phys. 38, 4355 (1967).
39. P.W. Palmberg and T.N. Rhodin, J. Appl. Phys. 39, 2425, (1968).
40. R.E. Weber and A.L. Johnson, J. Appl. Phys. 40, 314 (1969).
41. R.C. Oswald and R.E. Weber, Auger Spectra of the Elementary Constituents of the III-V and II-VI Compounds, AFAL-TR-70-12, Contract No. F33615-69-C-1053, February, 1970.

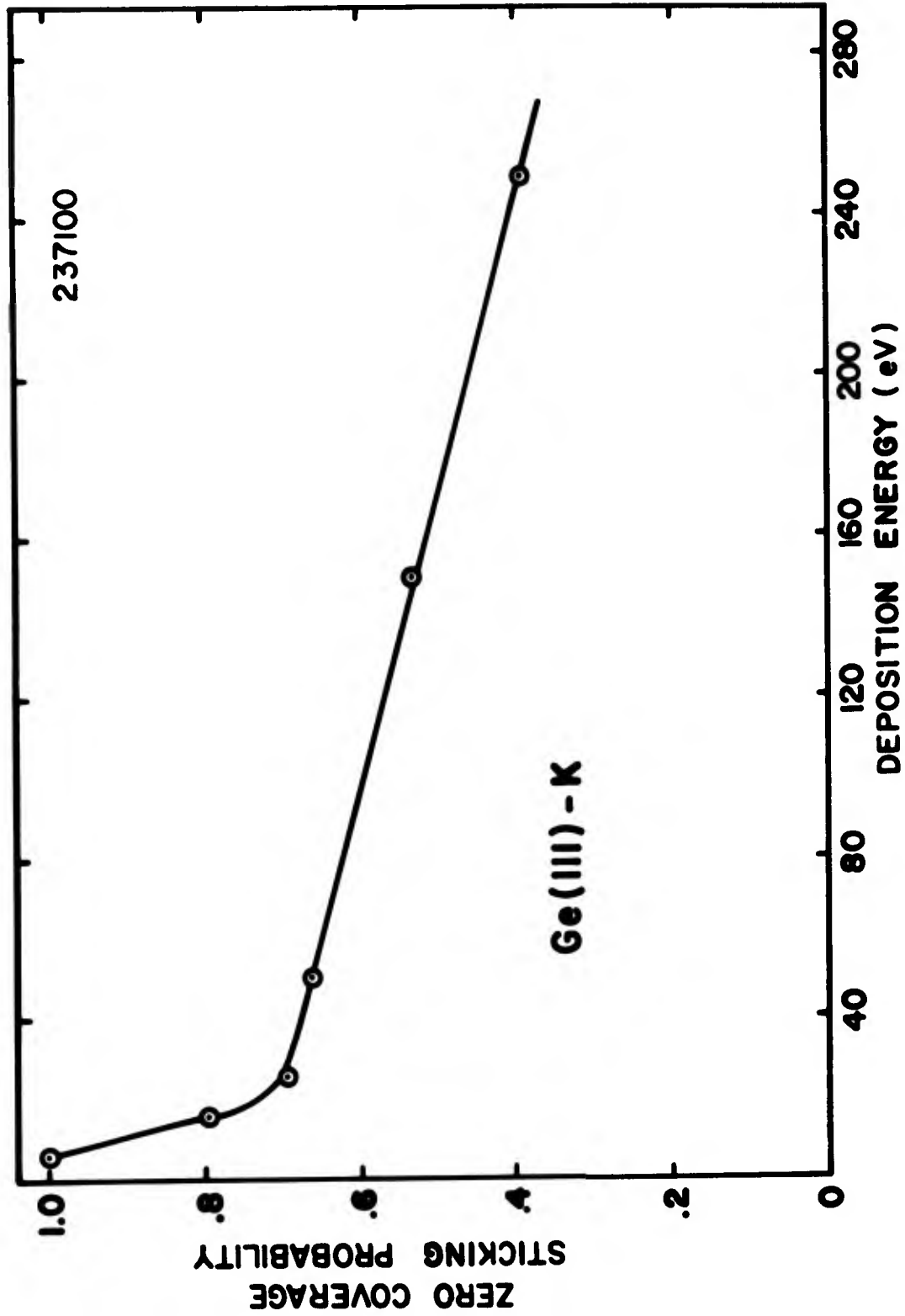


Figure 1 Sticking probability at zero coverage for K ions incident on Ge(111)

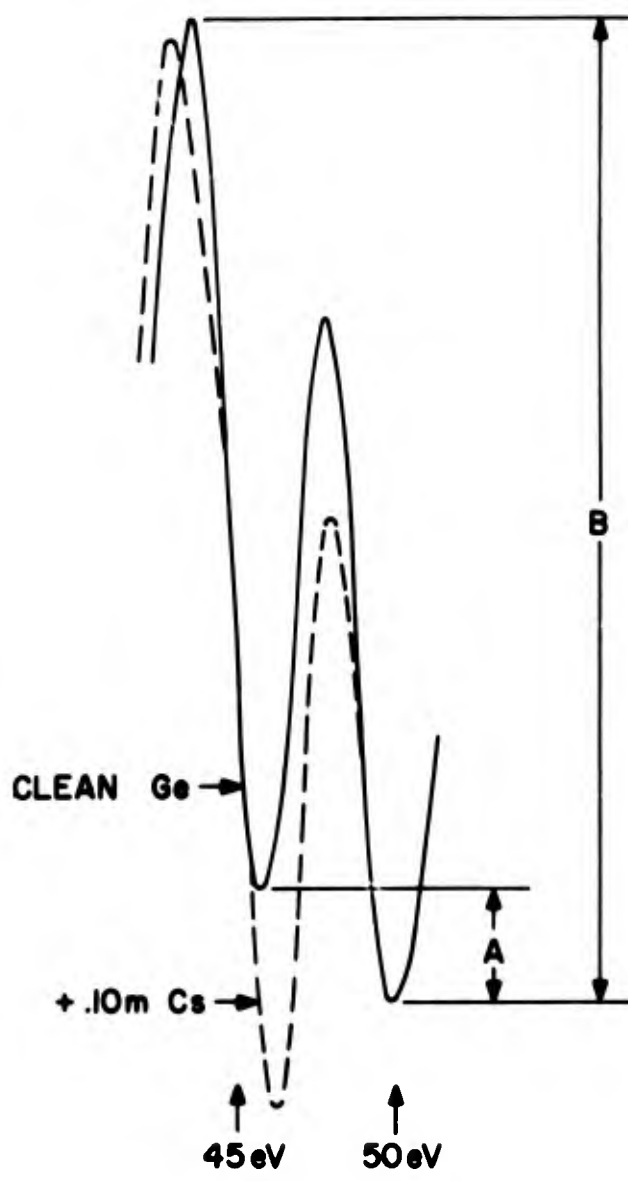


Figure 2 Features in AES spectrum used for Cs coverage determination

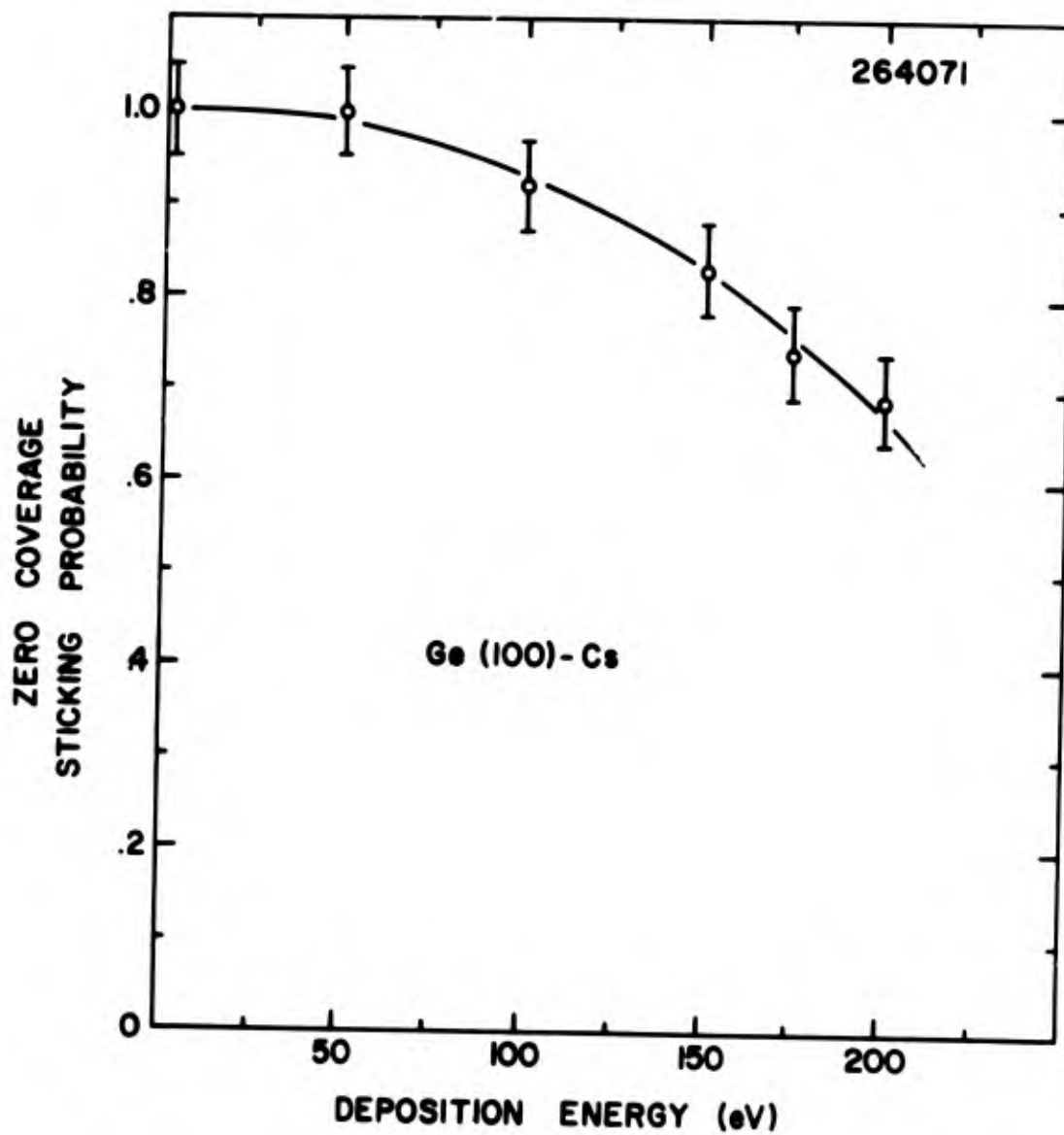


Figure 3 Sticking probability at zero coverage for Cs ions incident on Ge(100)

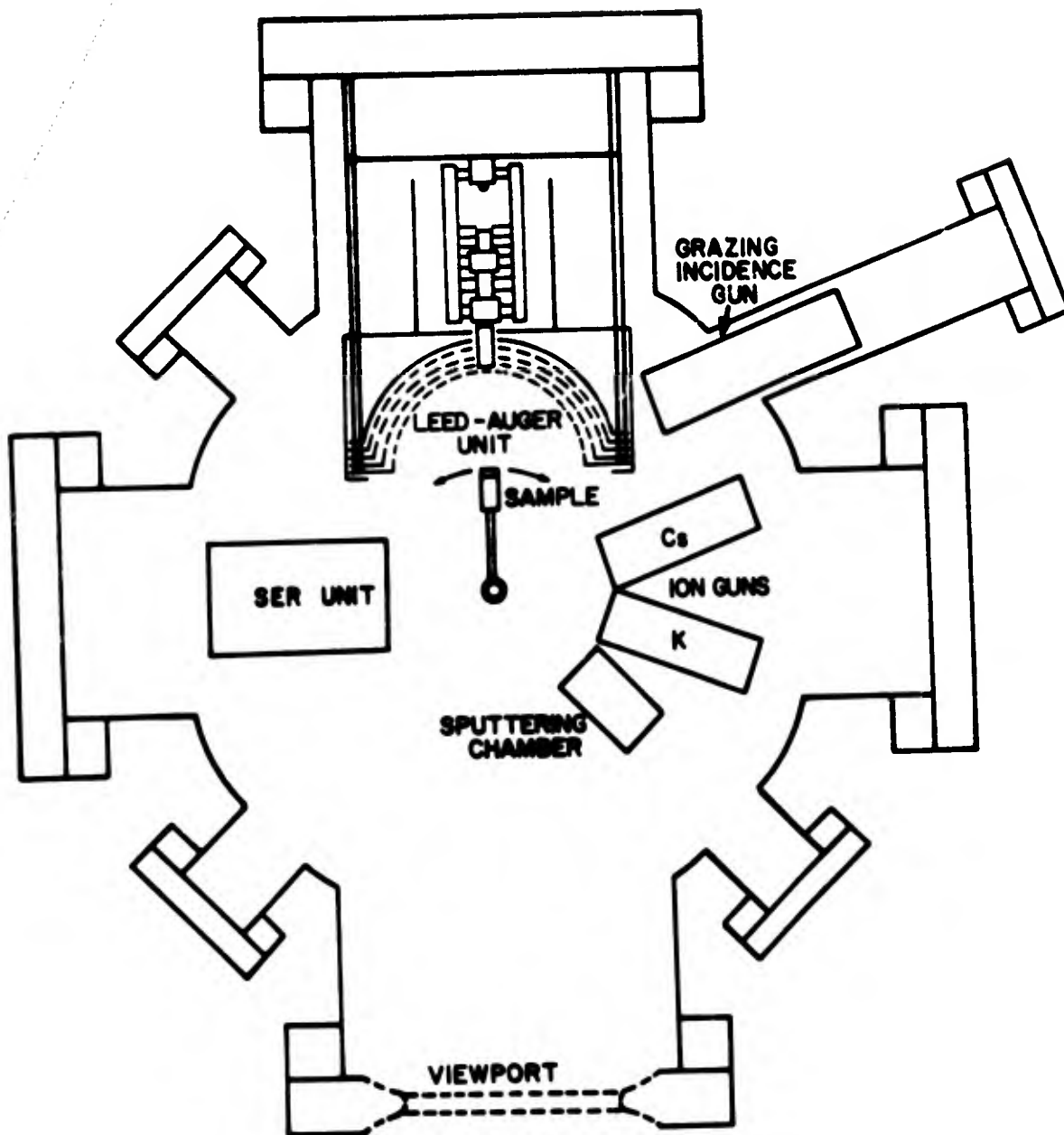
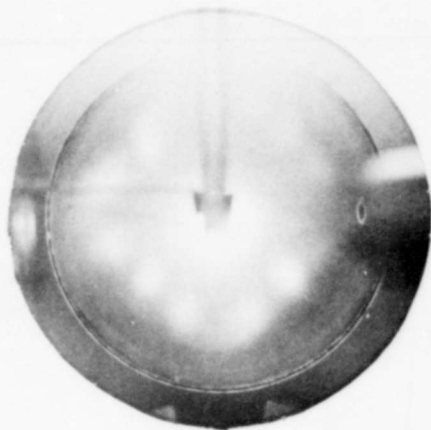
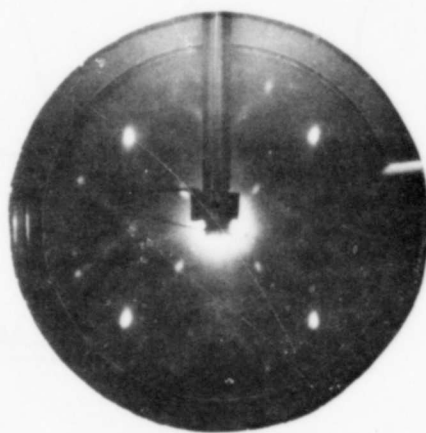


Figure 4 Cross-section of vacuum system used for Ge(100)-Cs-O study



a) CLEAN Ge(100), 4eV



b) CLEAN Ge(100), 21eV

Figure 5 LEED pattern from clean Ge(100) at a) 4 eV and b) 21 eV incident electron energy

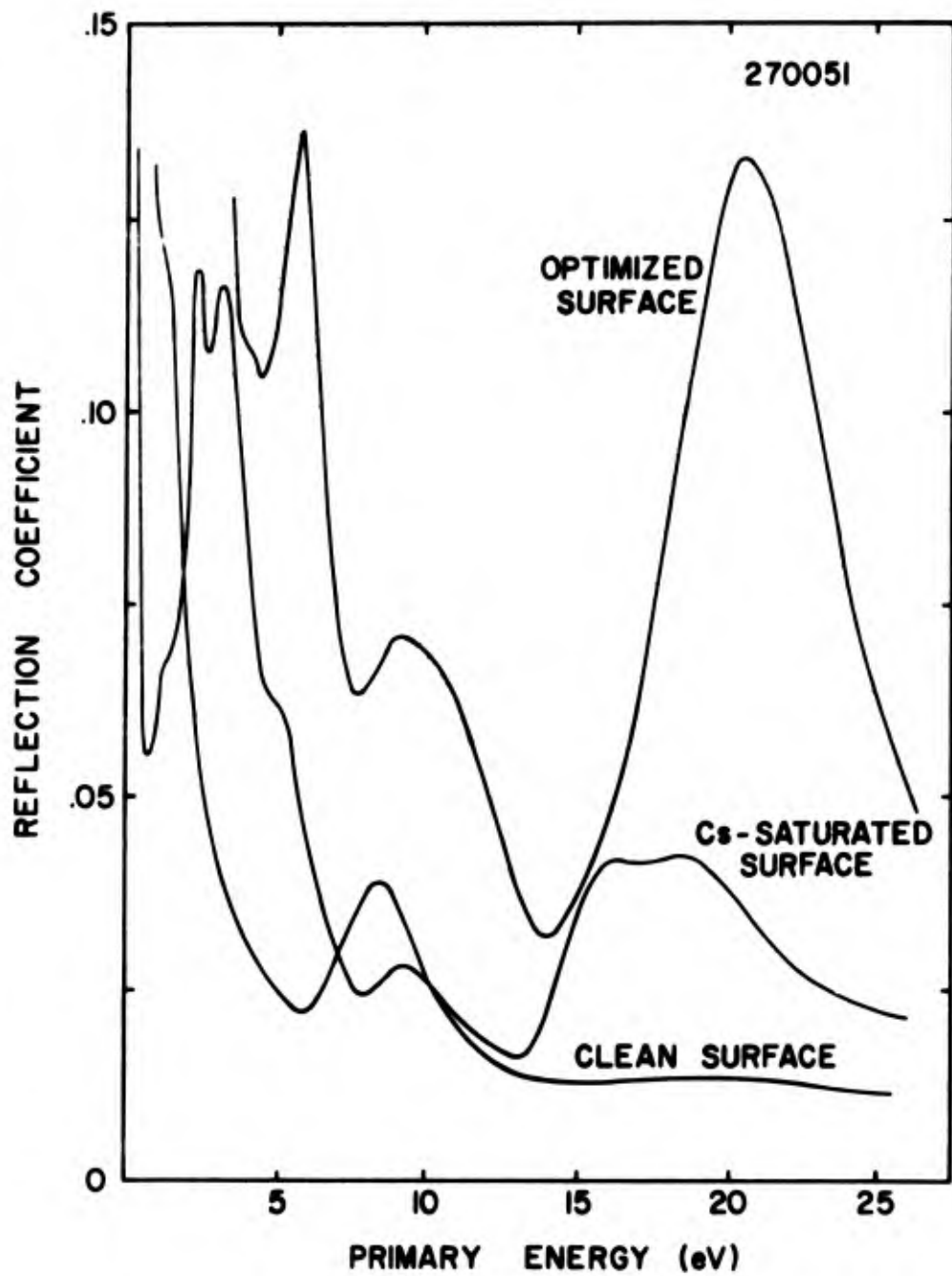


Figure 6 SER from clean, Cs-saturated, and optimized surfaces of Ge(100)

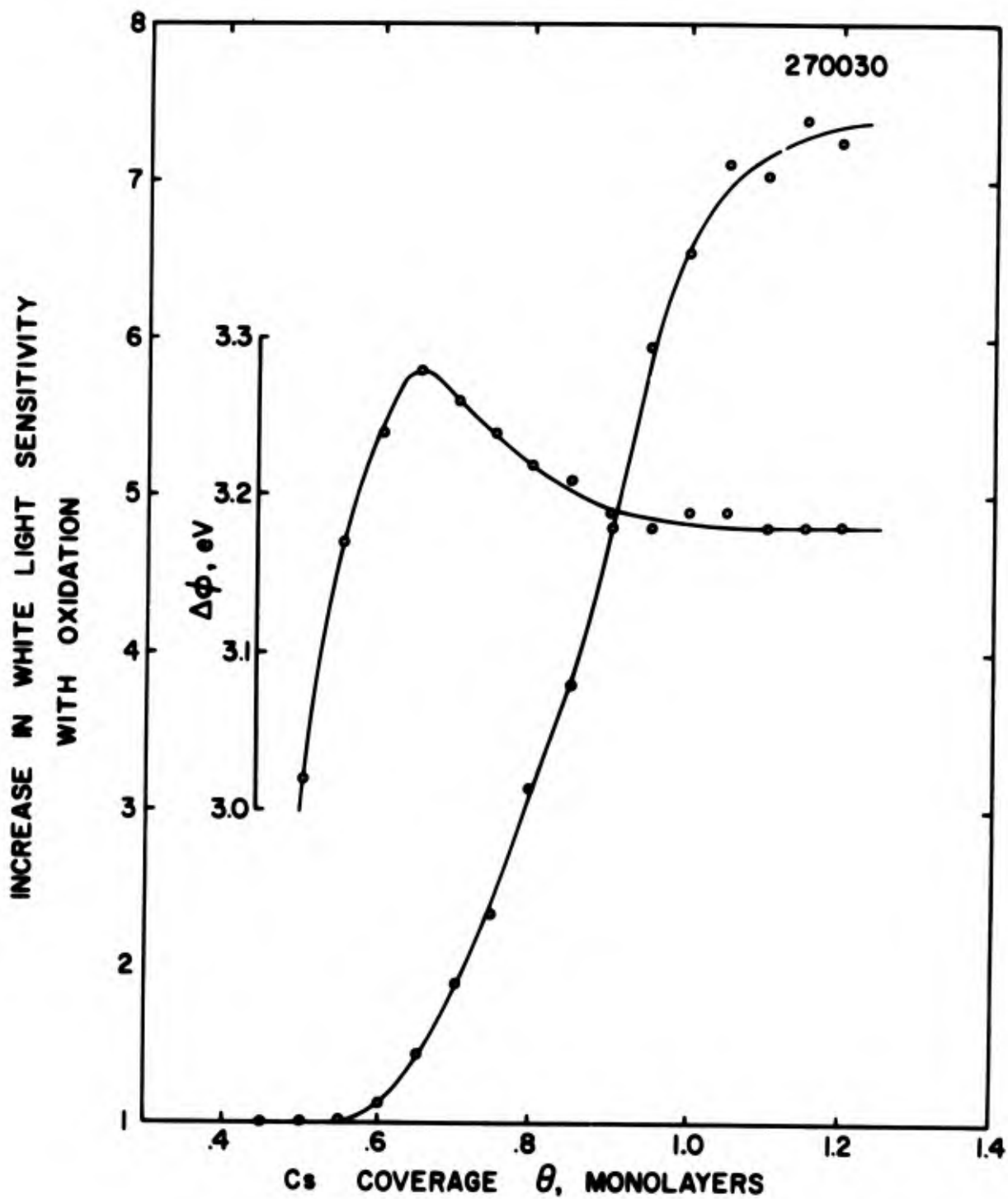


Figure 7 Initial work function change and increase in white light sensitivity with oxidation vs. Cs coverage on Ge(100)

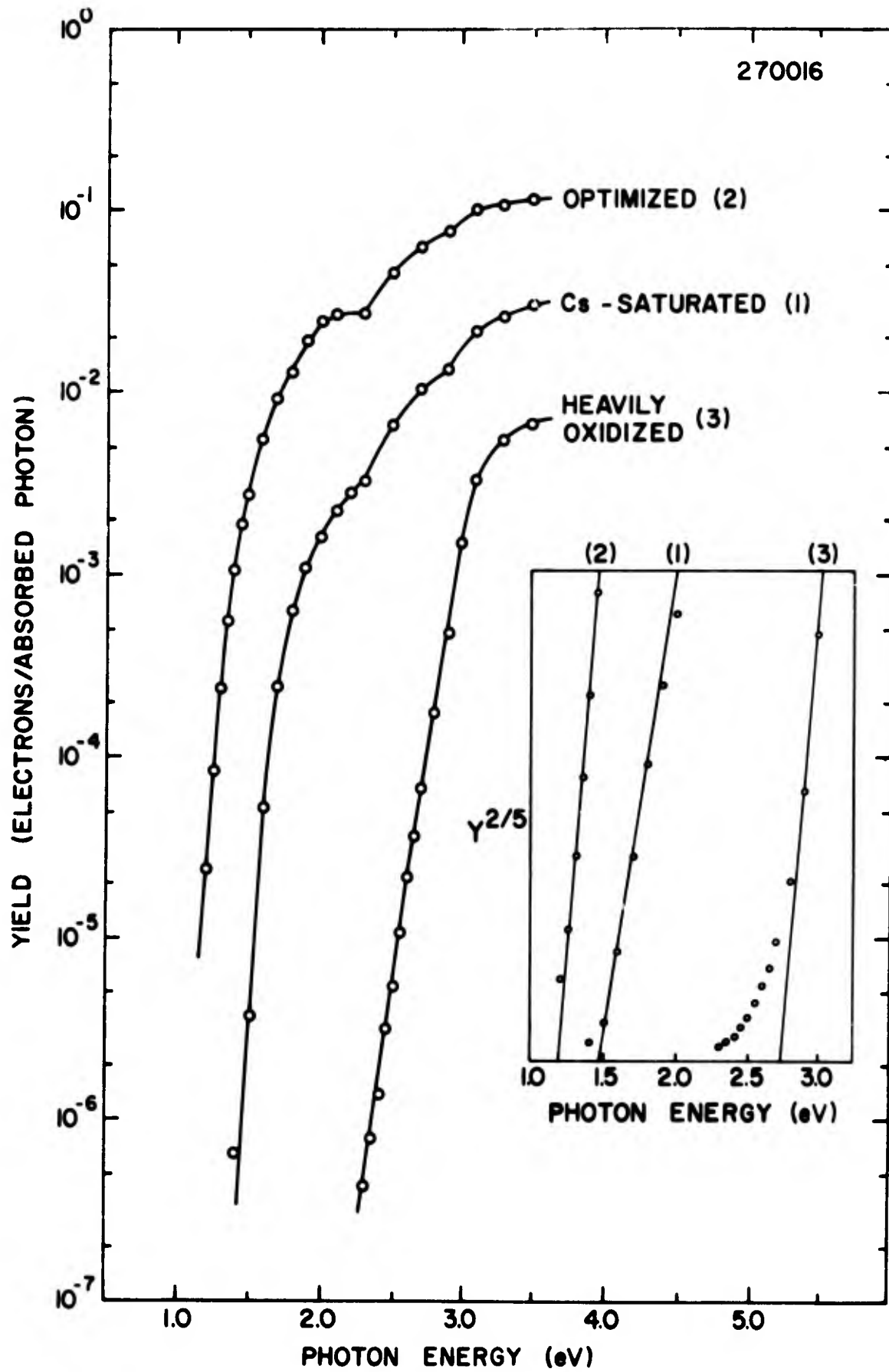


Figure 3 Photoelectric yield from Cs saturated, optimized, and heavily oxidized surfaces

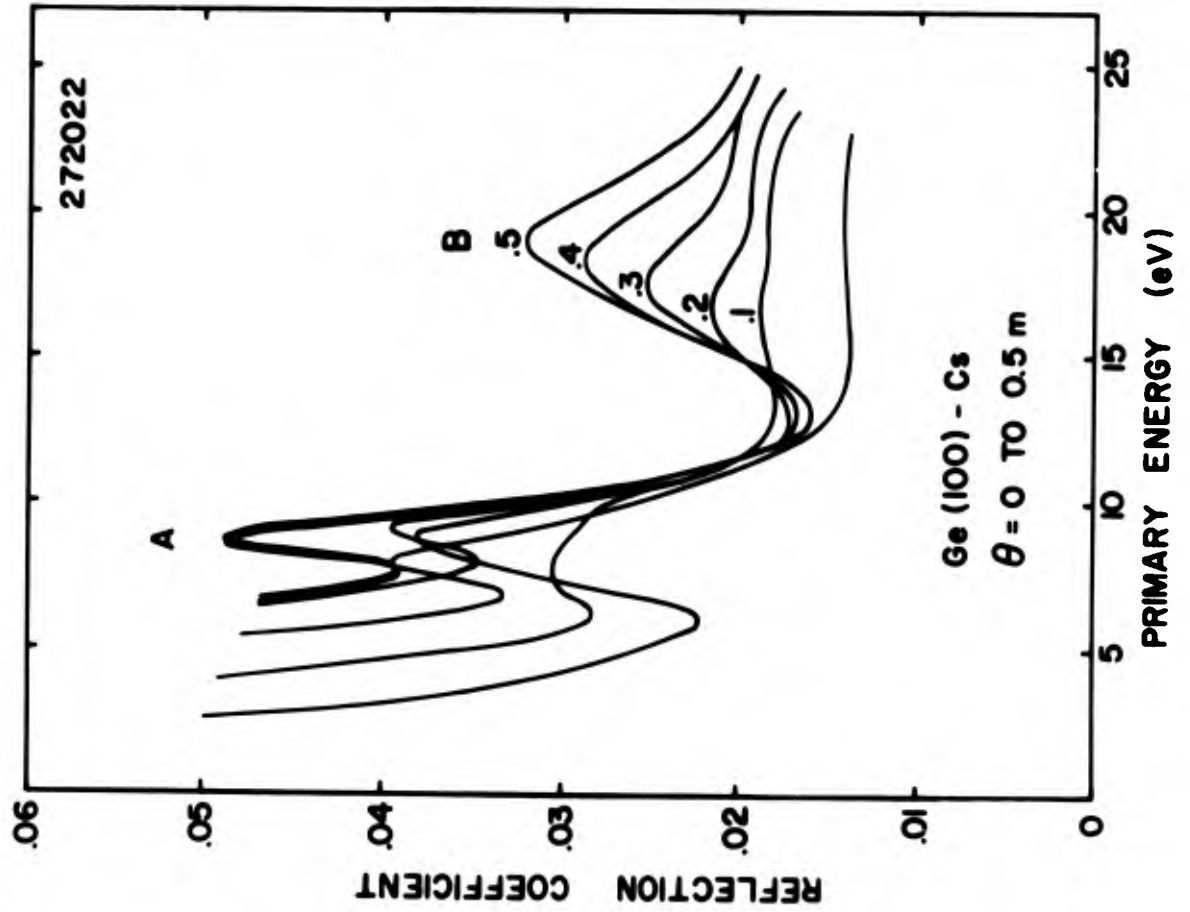
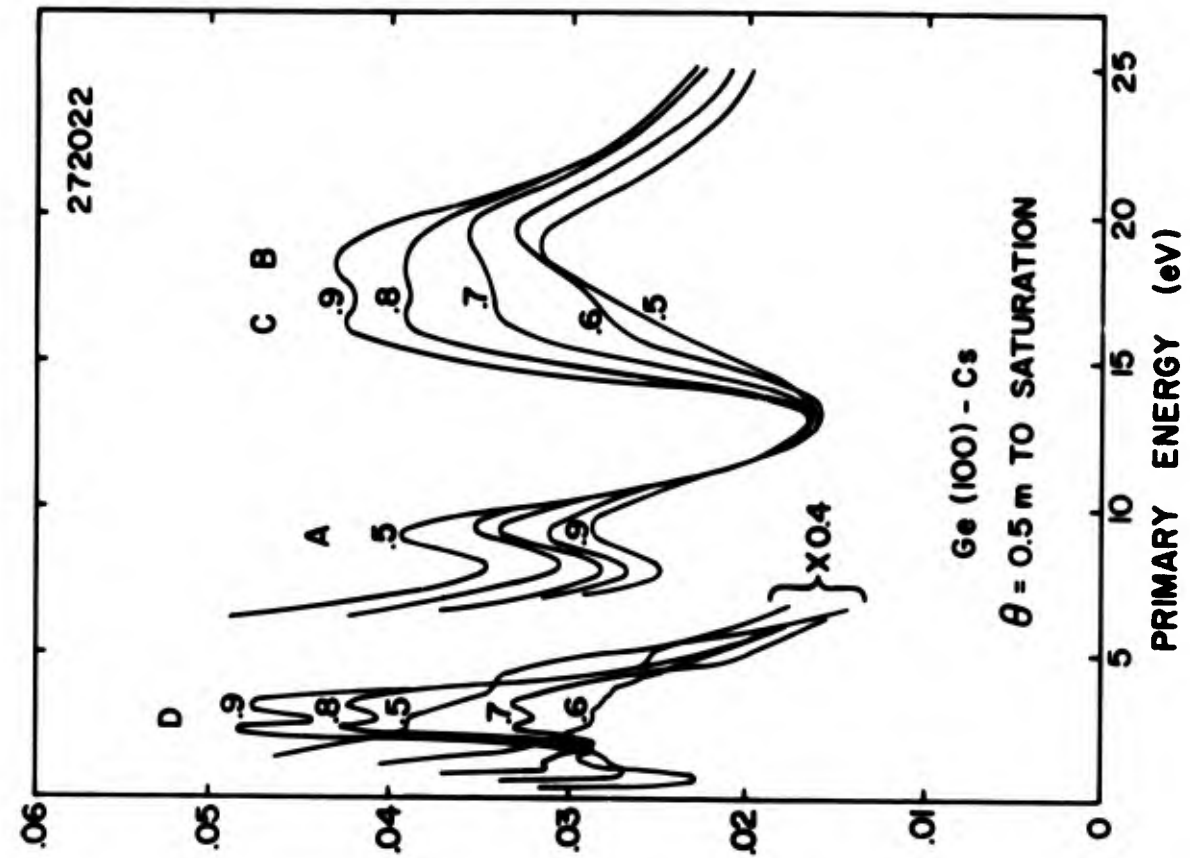


Figure 9 SER vs. Cs coverage on Ge(100)

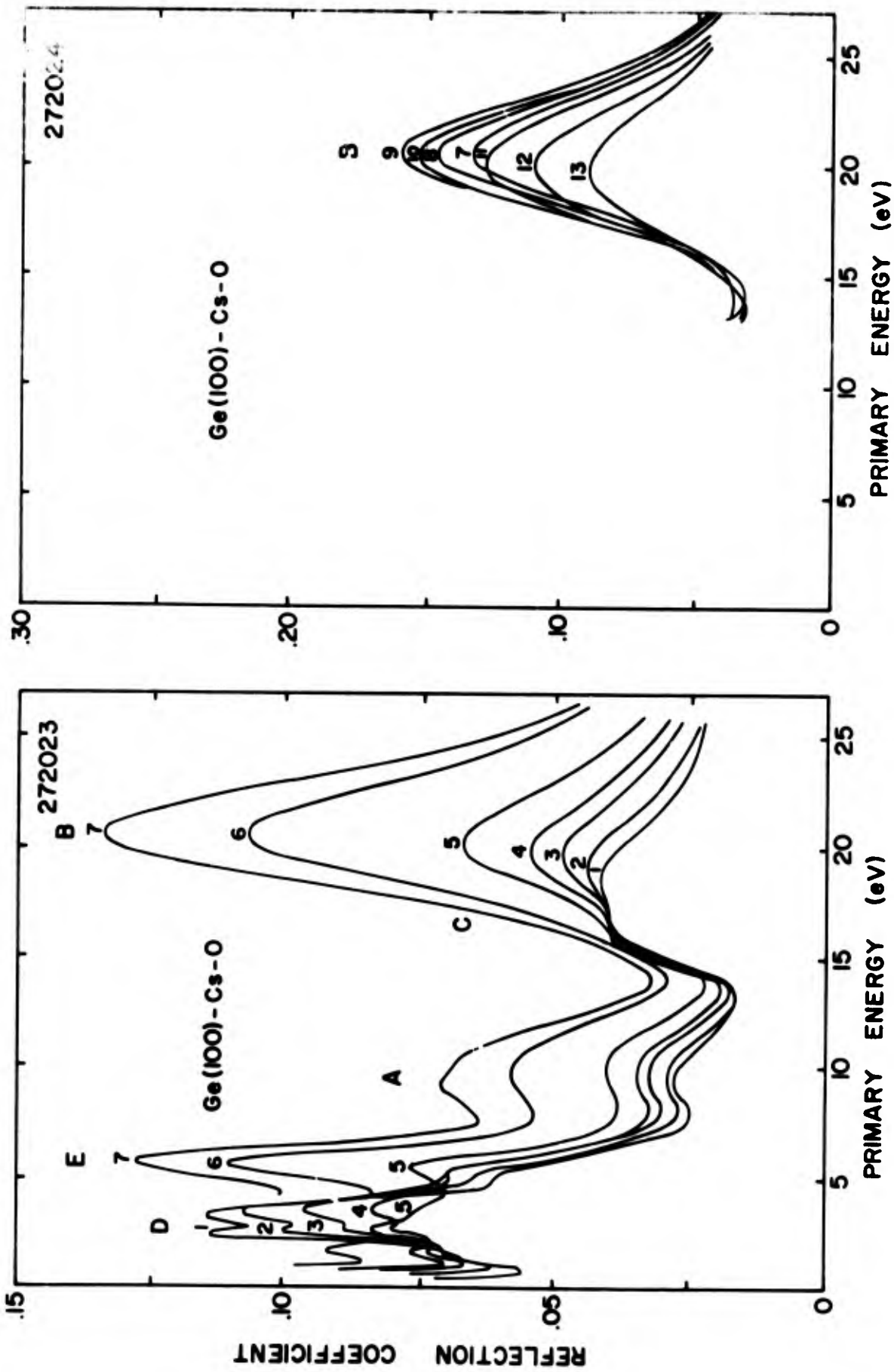
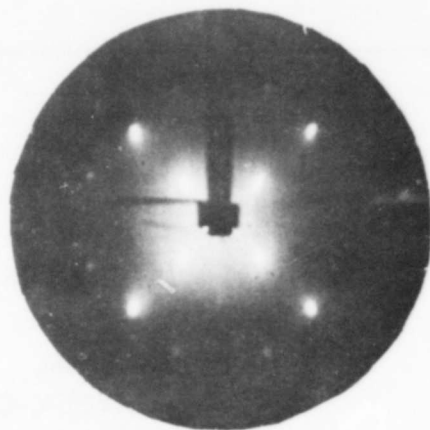
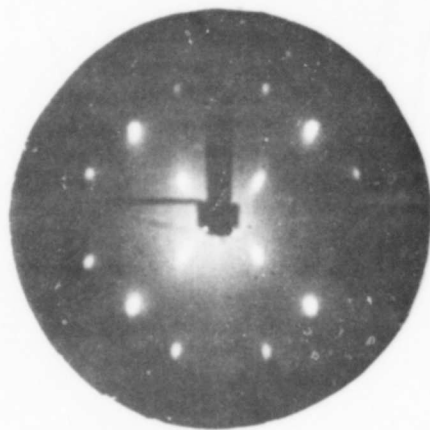


Figure 10 SER vs. oxidation for Ge(100)-Cs



a) Ge(100)-Cs, 16 eV



b) Ge(100)-Cs-O, 16 eV

Figure 11 LEED patterns from Cs-saturated and optimized surfaces of Ge(100) at 16 eV incident electron energy

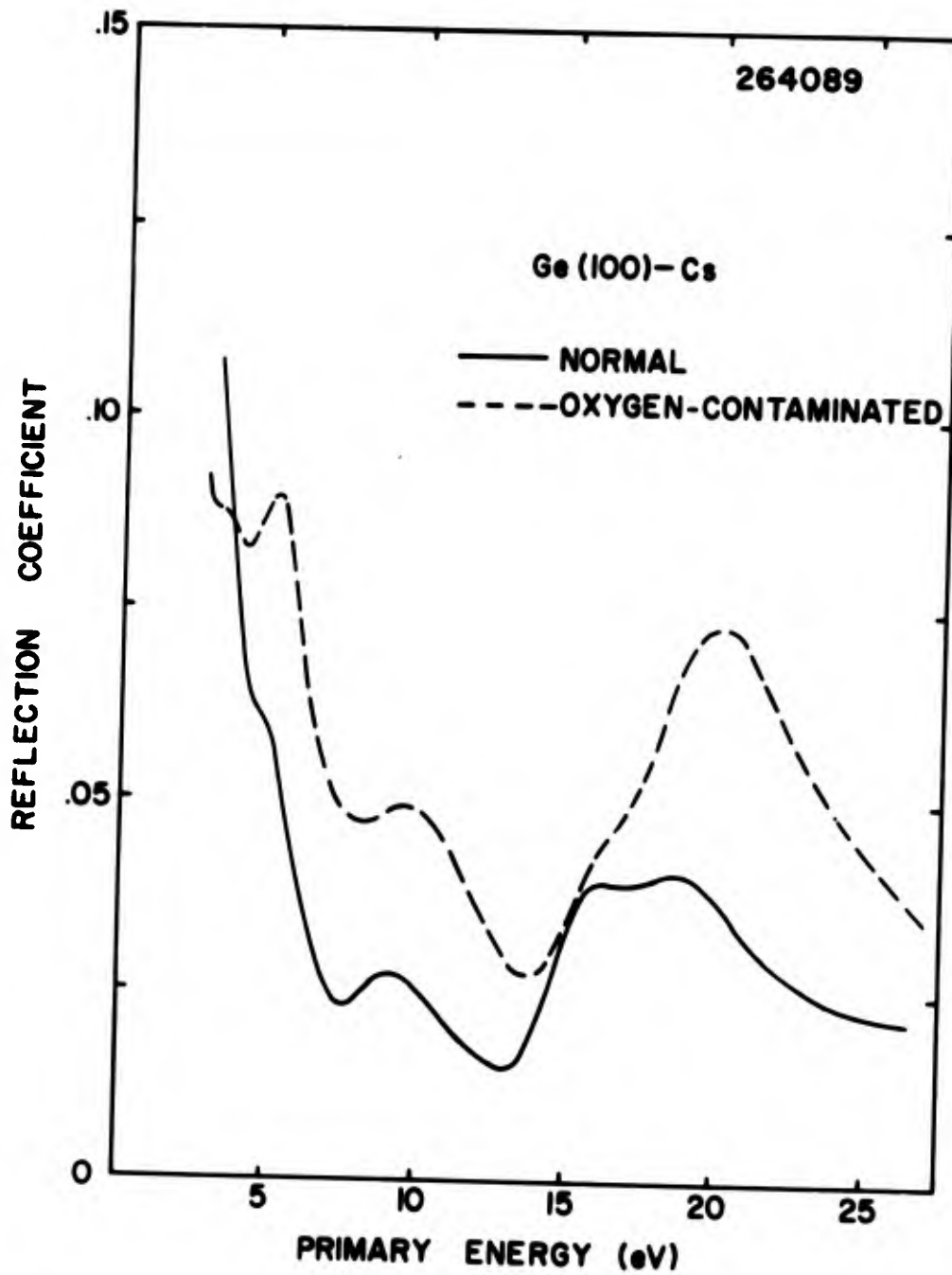


Figure 12 SER from Ge(100)-Cs following normal and oxygen contaminated Cs depositions

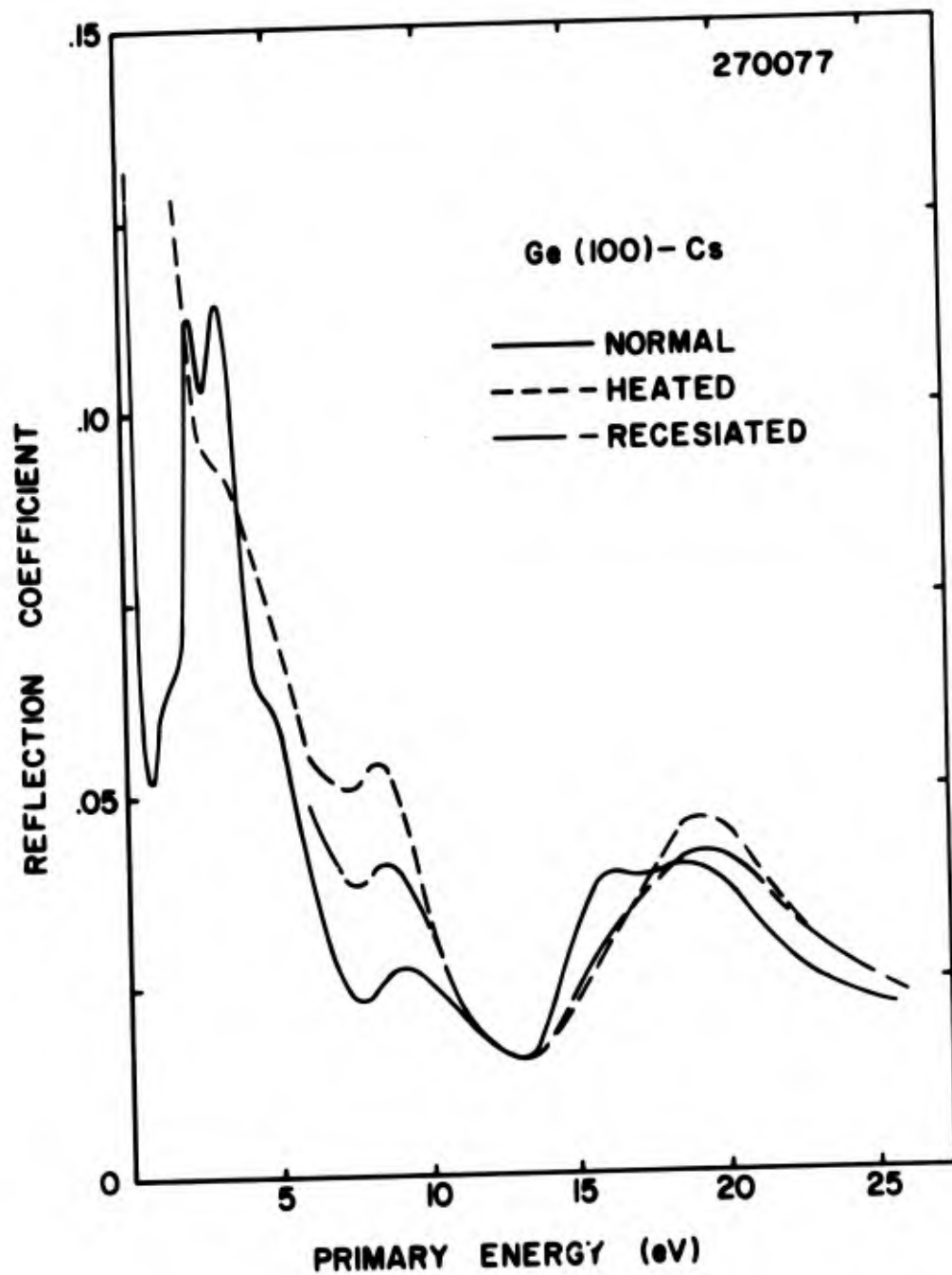


Figure 13 SER from Ge(100)-Cs for normal, heated, and recesiated surfaces

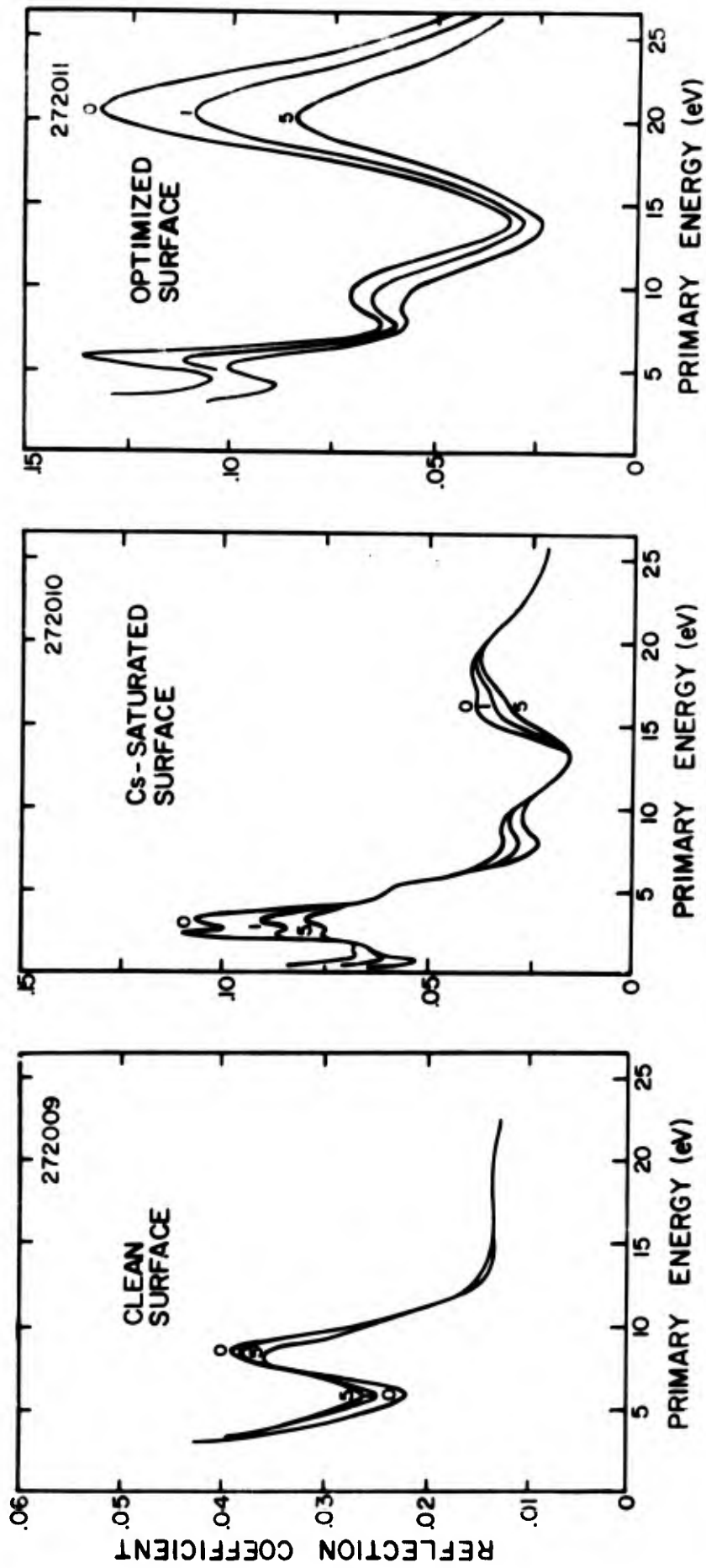


Figure 14 SER from clean, Cs-saturated and optimized surfaces of Ge(100) following 0,1, and 5 Larmuir initial oxygen exposures

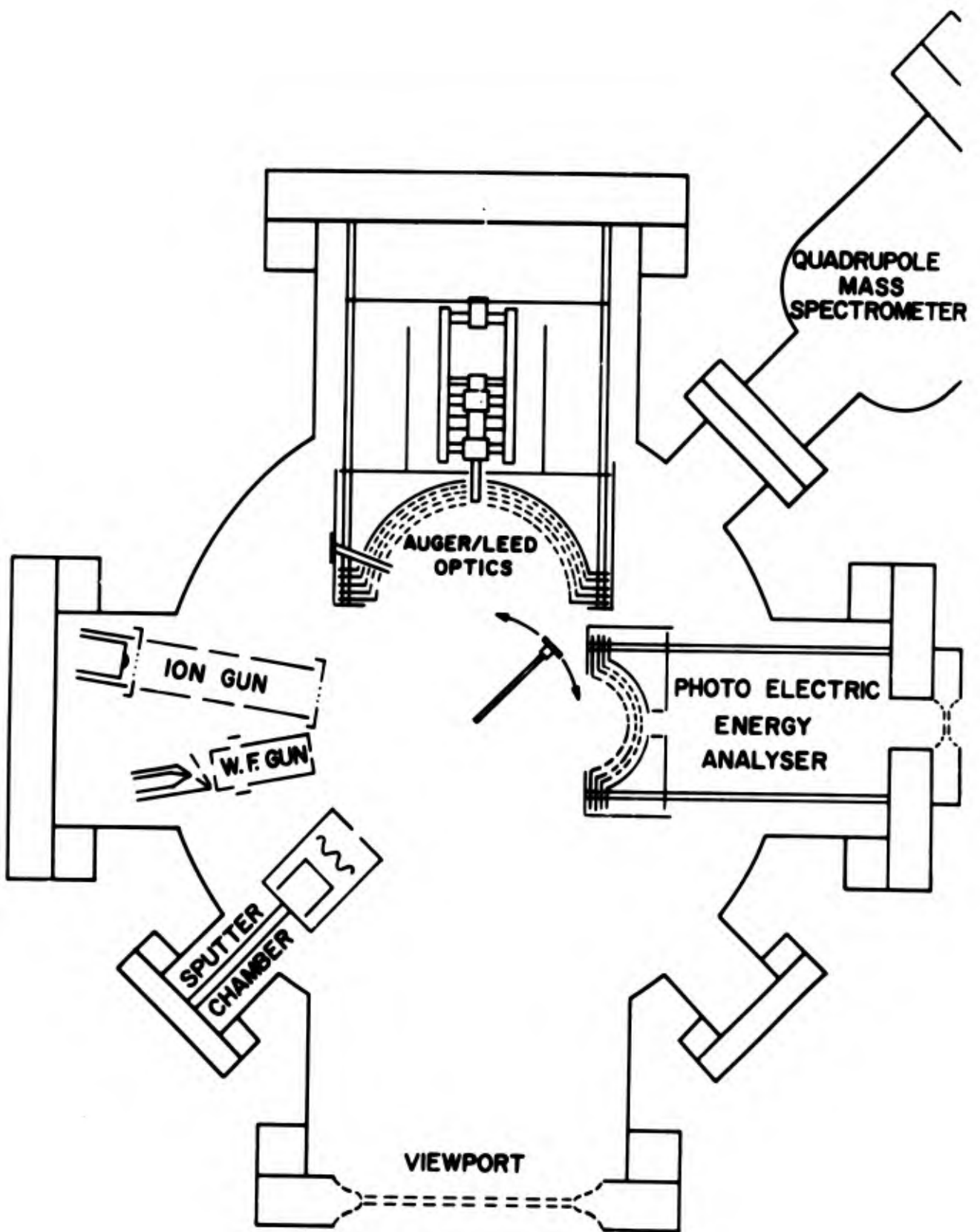


Figure 15 Vacuum system for photoemission studies

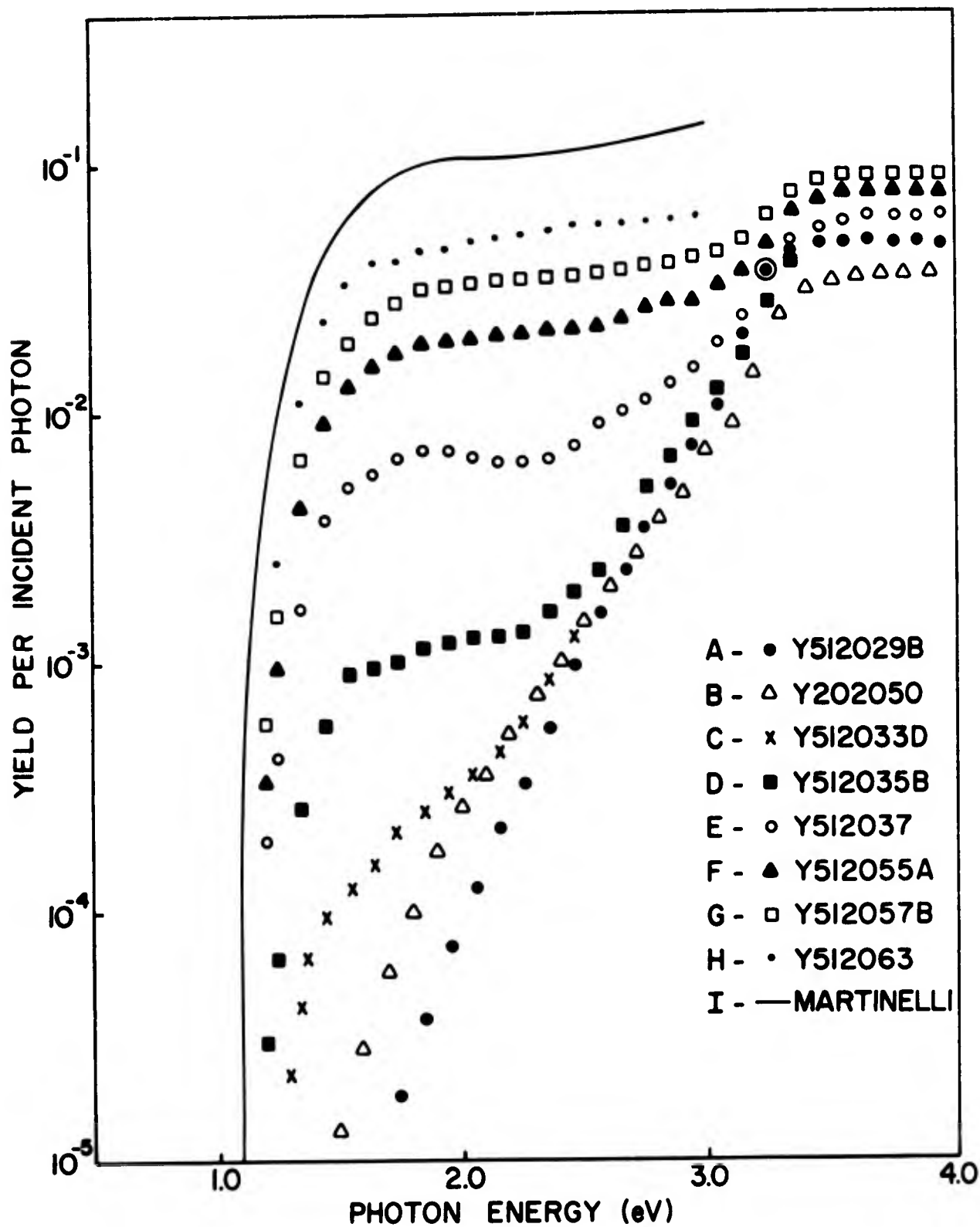
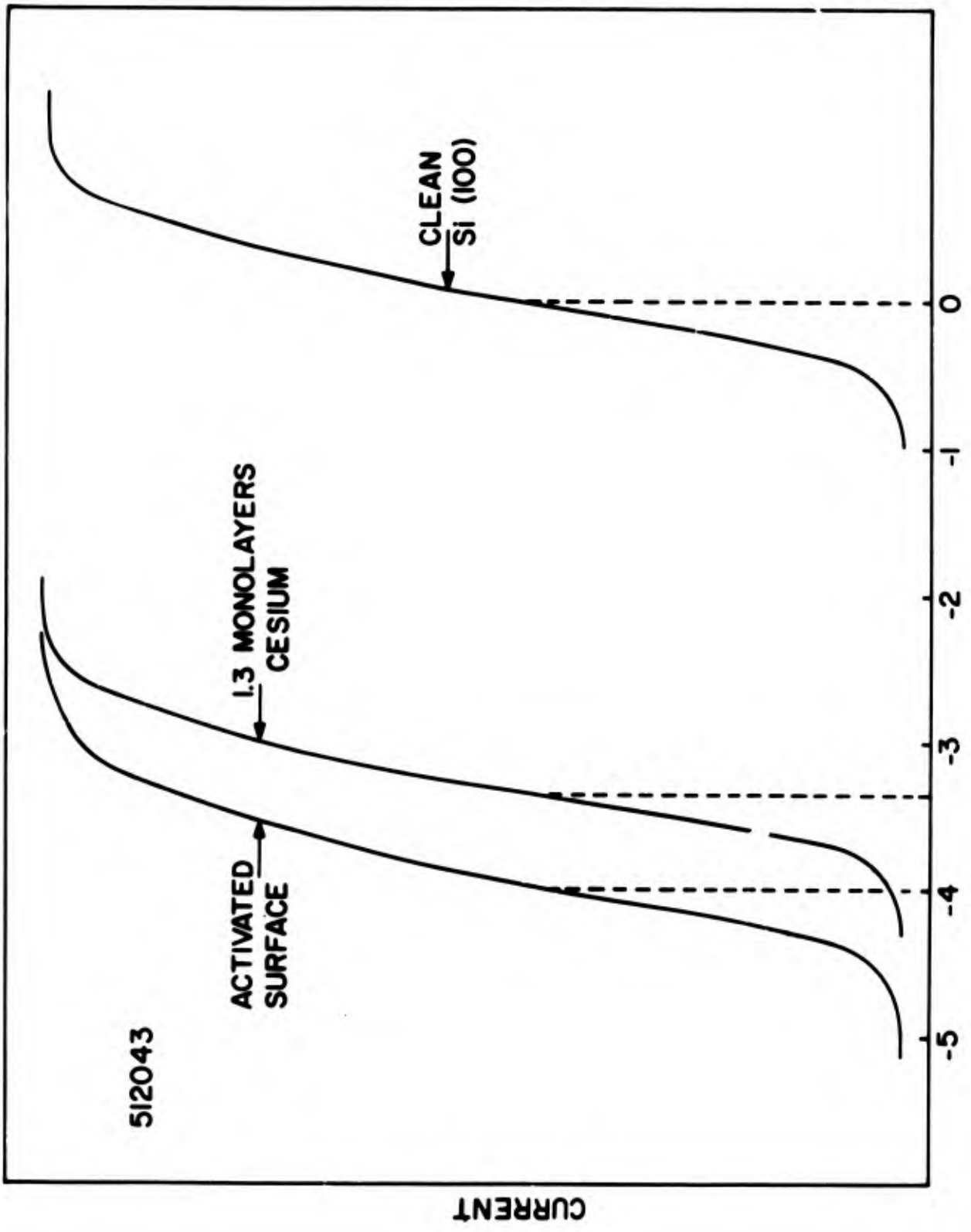


Figure 16 Spectral yield of activated Si(100) as a function of surface treatment



WORK FUNCTION CHANGE (eV)

Figure 17 Retarding potential characteristics of clean, cesiated and activated Si(100)

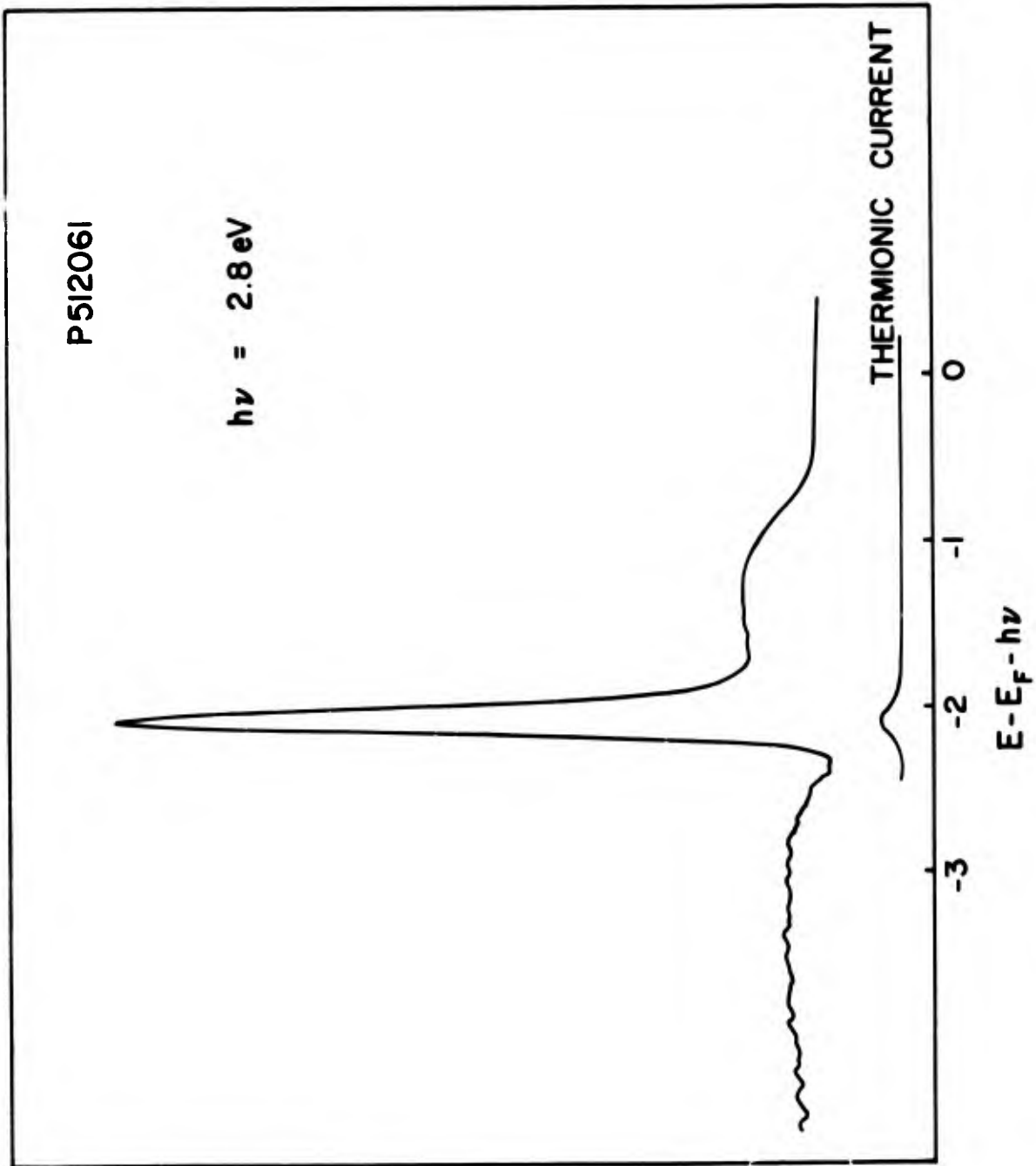


Figure 18 Photoelectron energy distributions for activated Si(100)

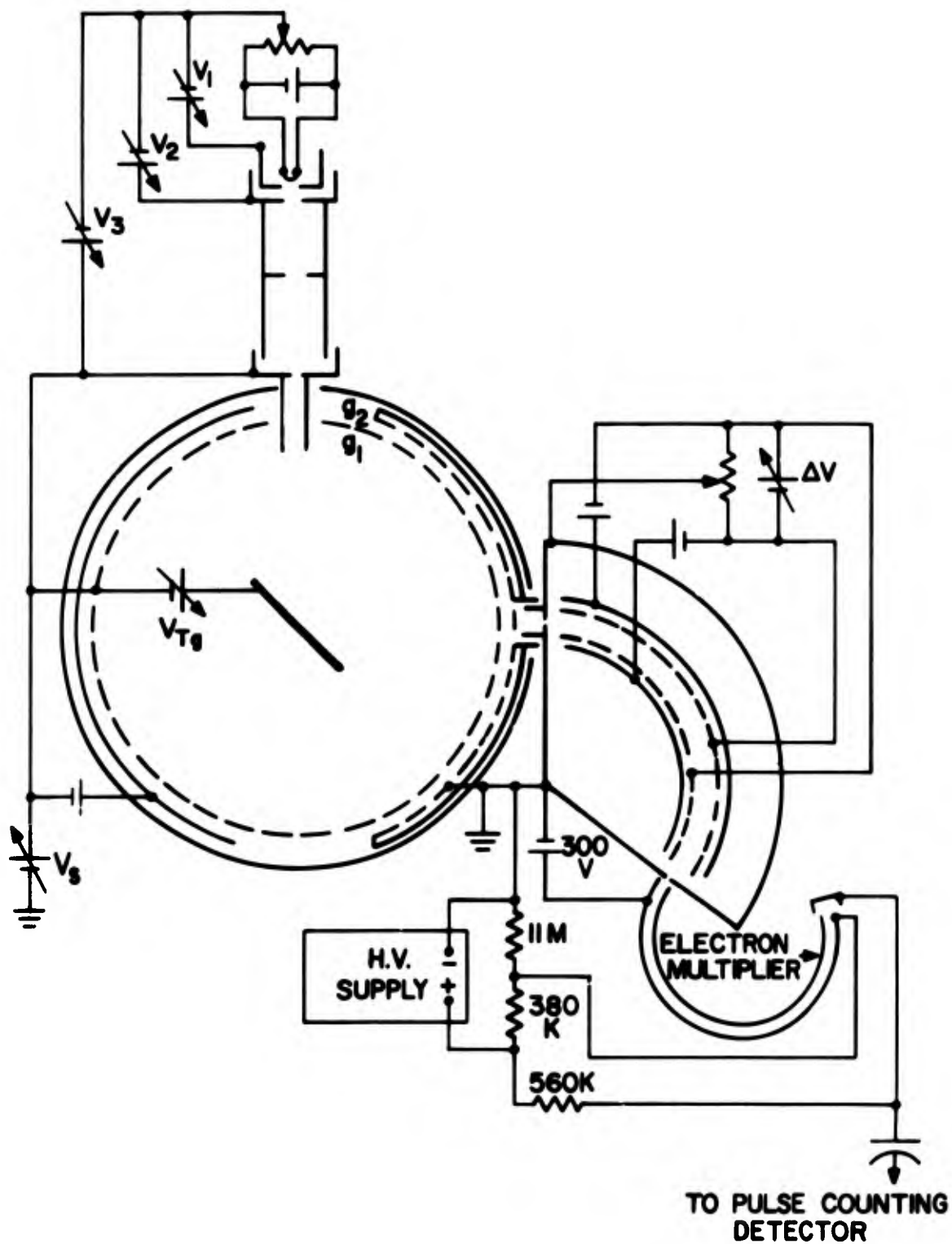


Figure 19 Schematic diagram of experimental apparatus

263074

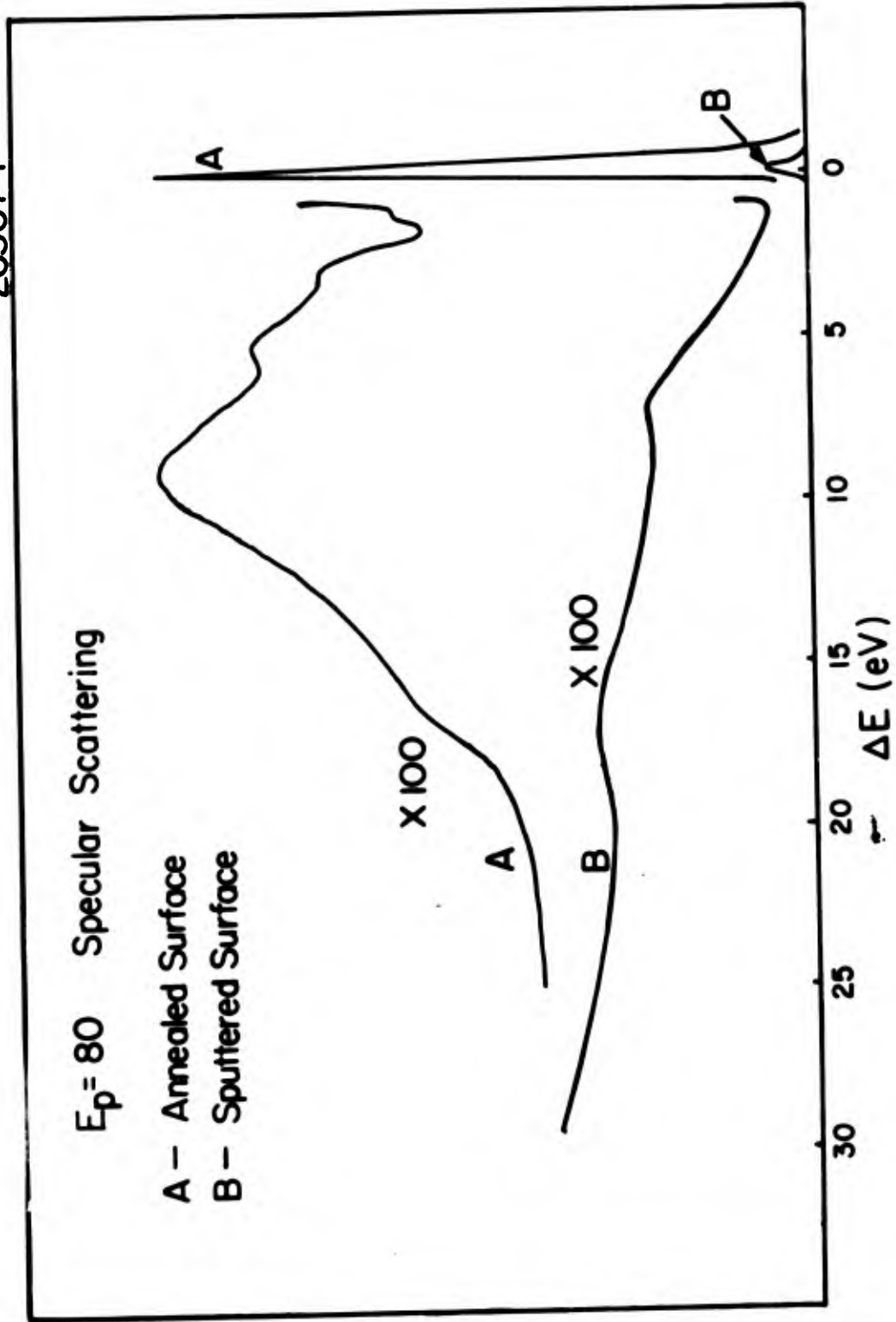


Figure 20 Inelastic electron spectra for a) annealed surface and b) sputtered surface

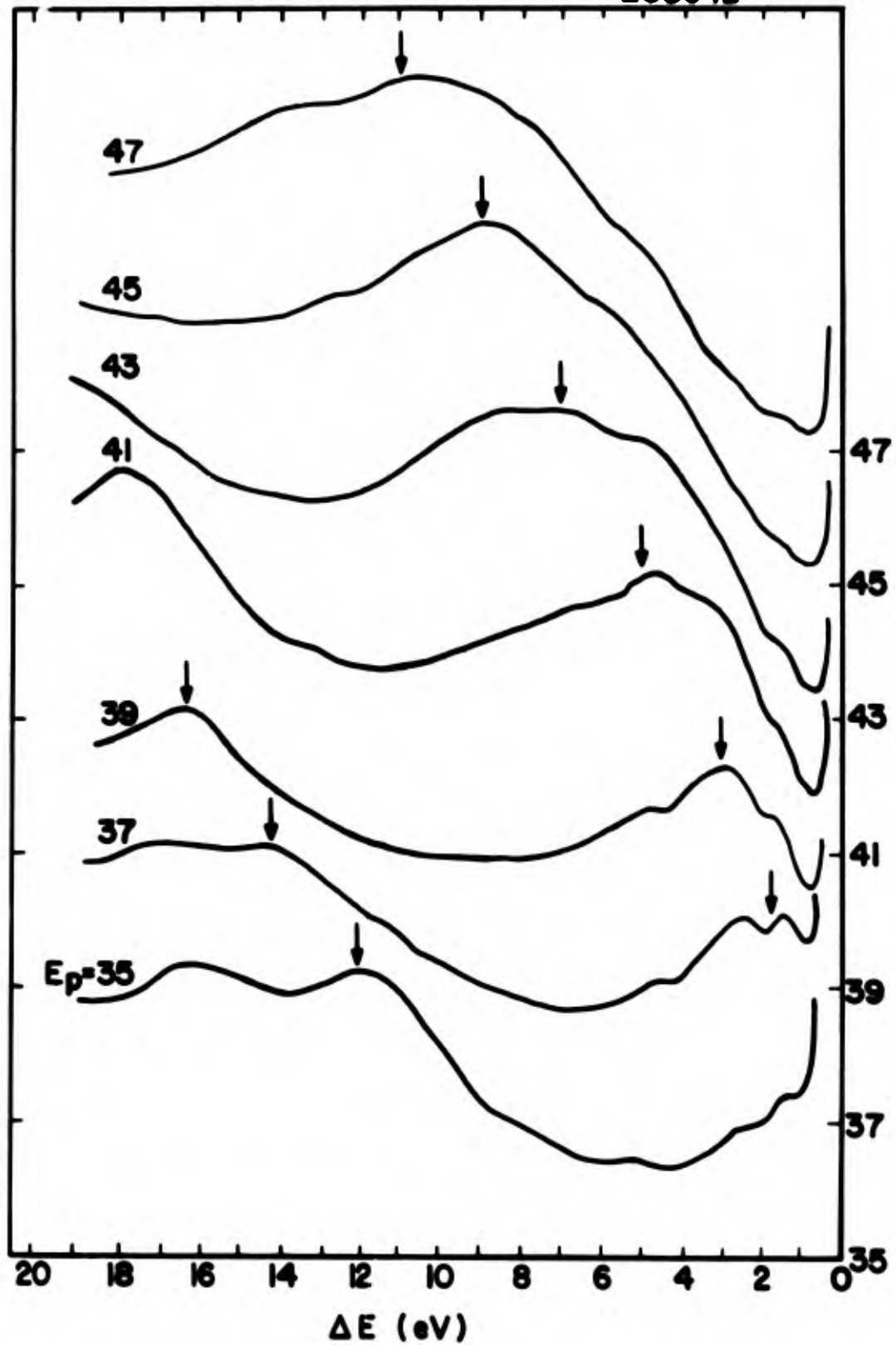


Figure 21 Inelastic electron spectra as function of E_p measured in scattering direction of (01) LEED beam at 36 eV

268034

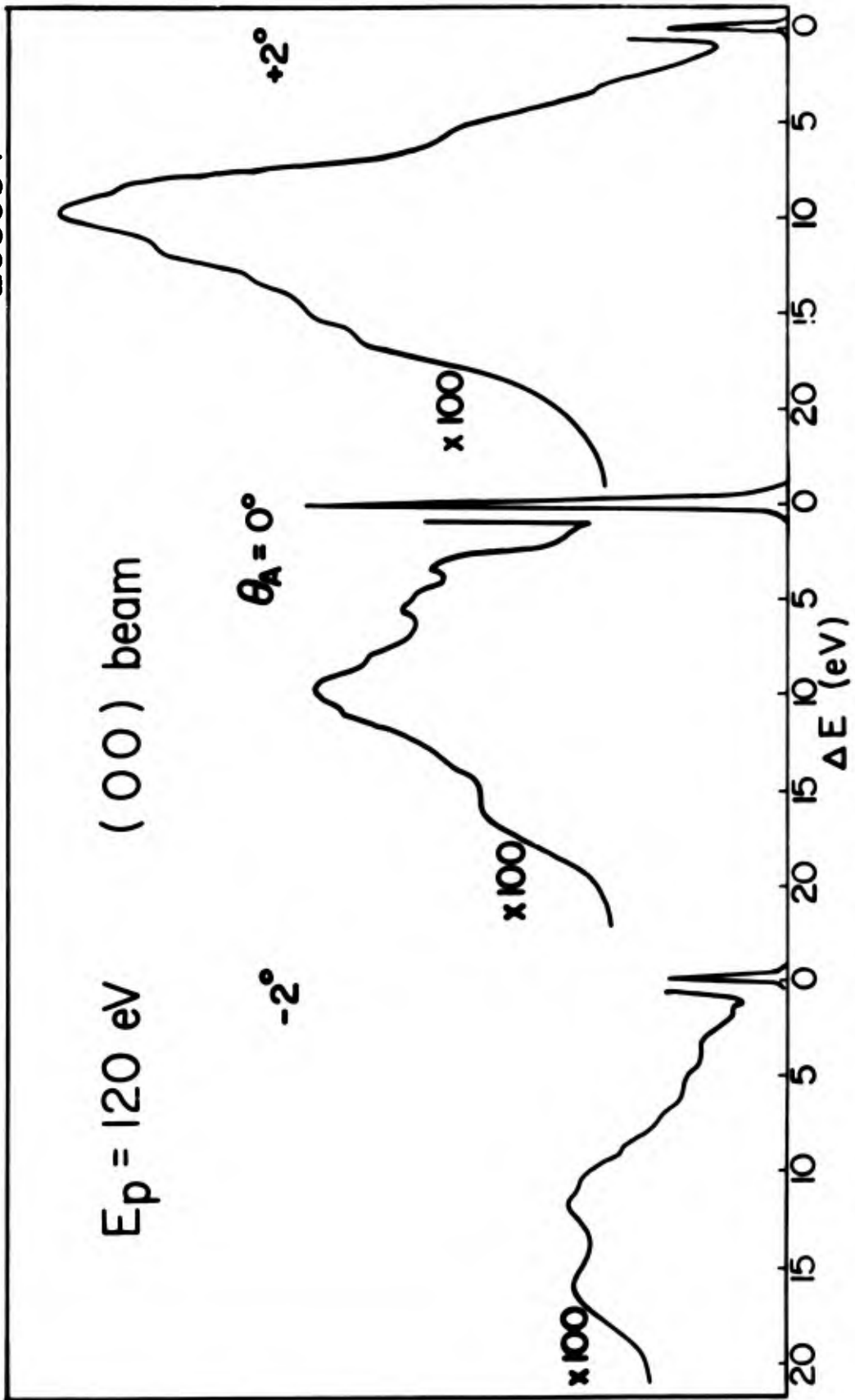


Figure 22 Inelastic electron spectra measured in (00) LEED beam direction and 2° to either side in plane of incidence

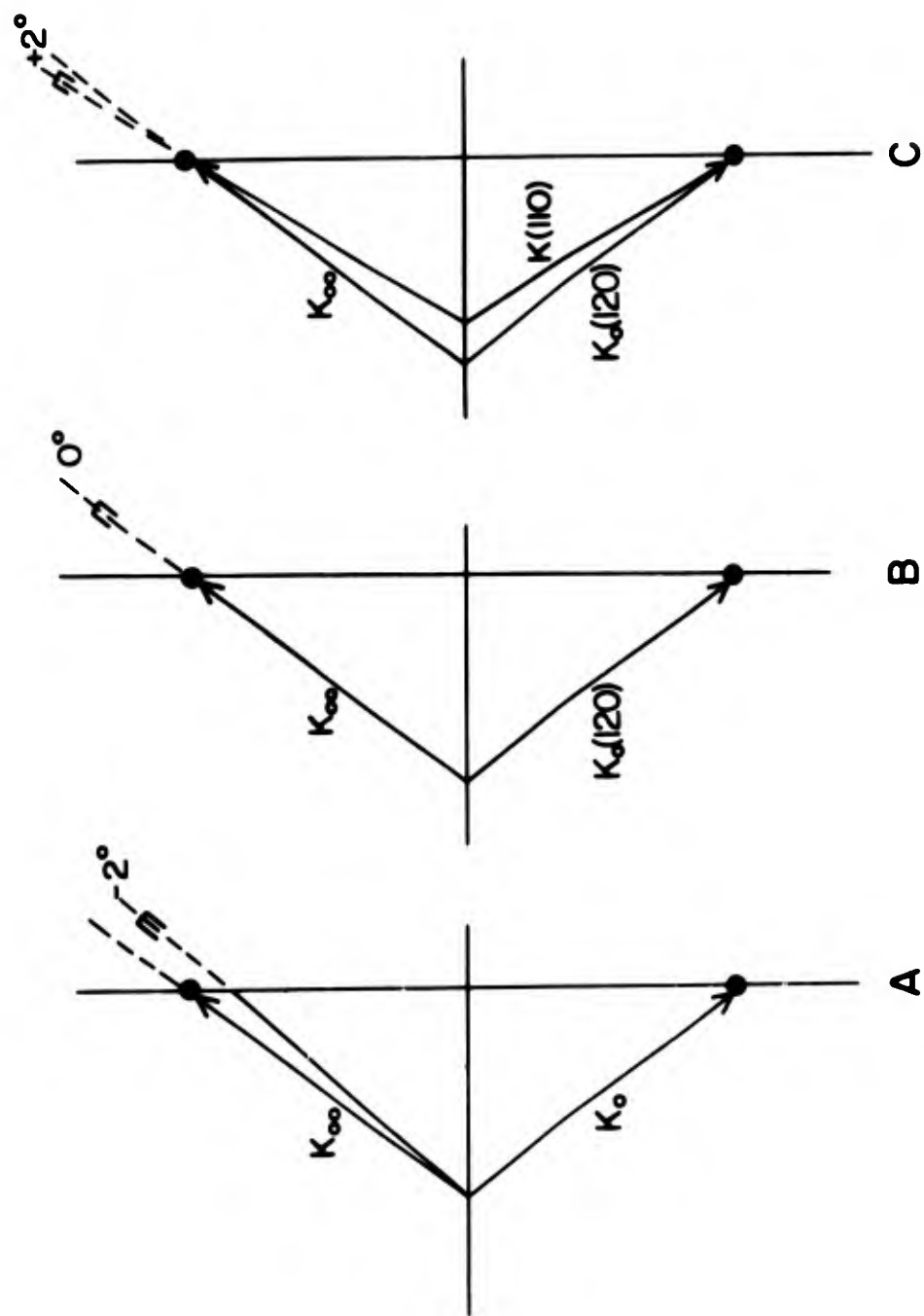


Figure 23 K-space plots showing scattering conditions for inelastic spectra of Fig. 22

268034

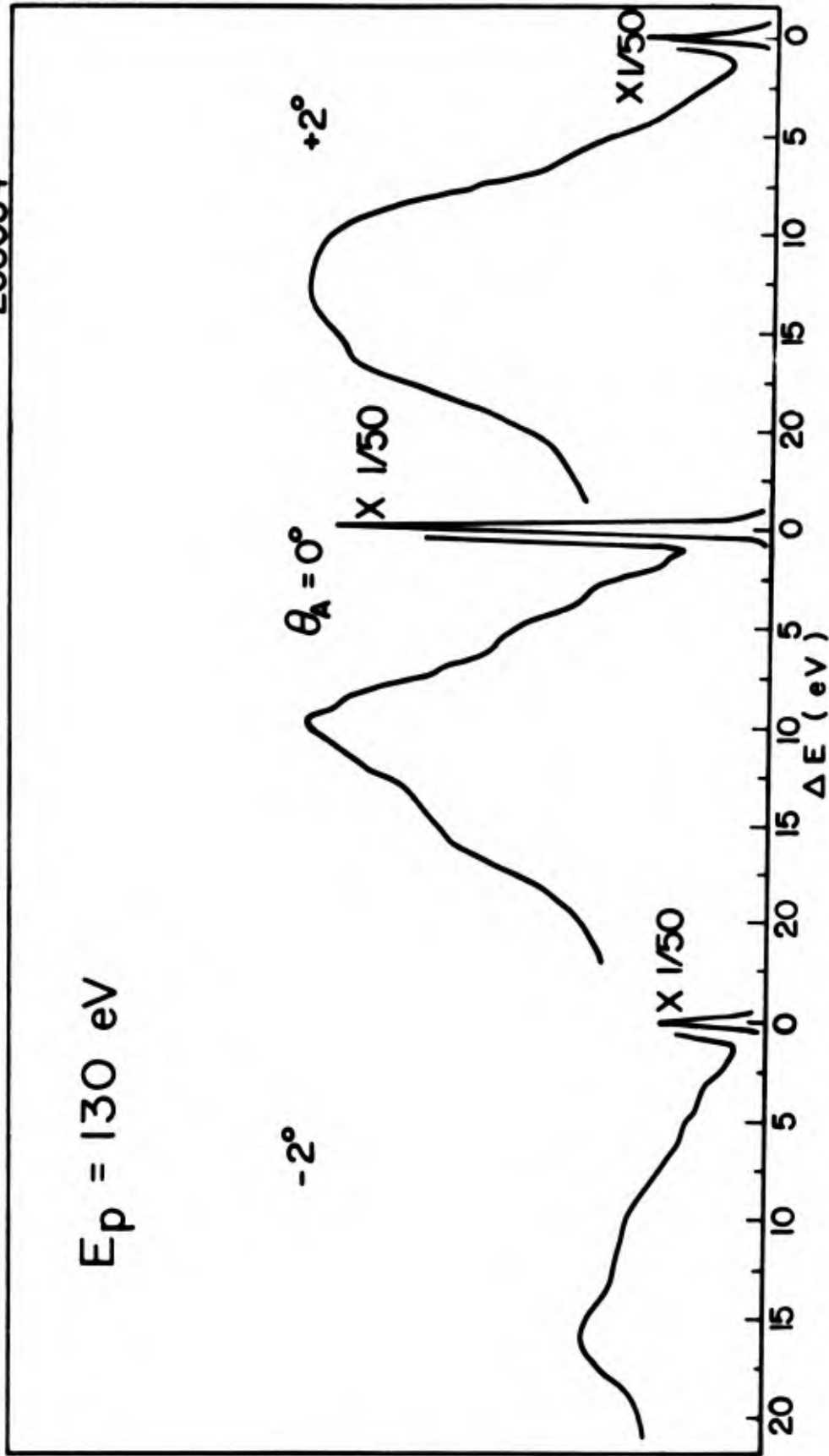


Figure 24 Inelastic electron spectra measured in (00) LEED beam direction and 2° to either side in plane of incidence

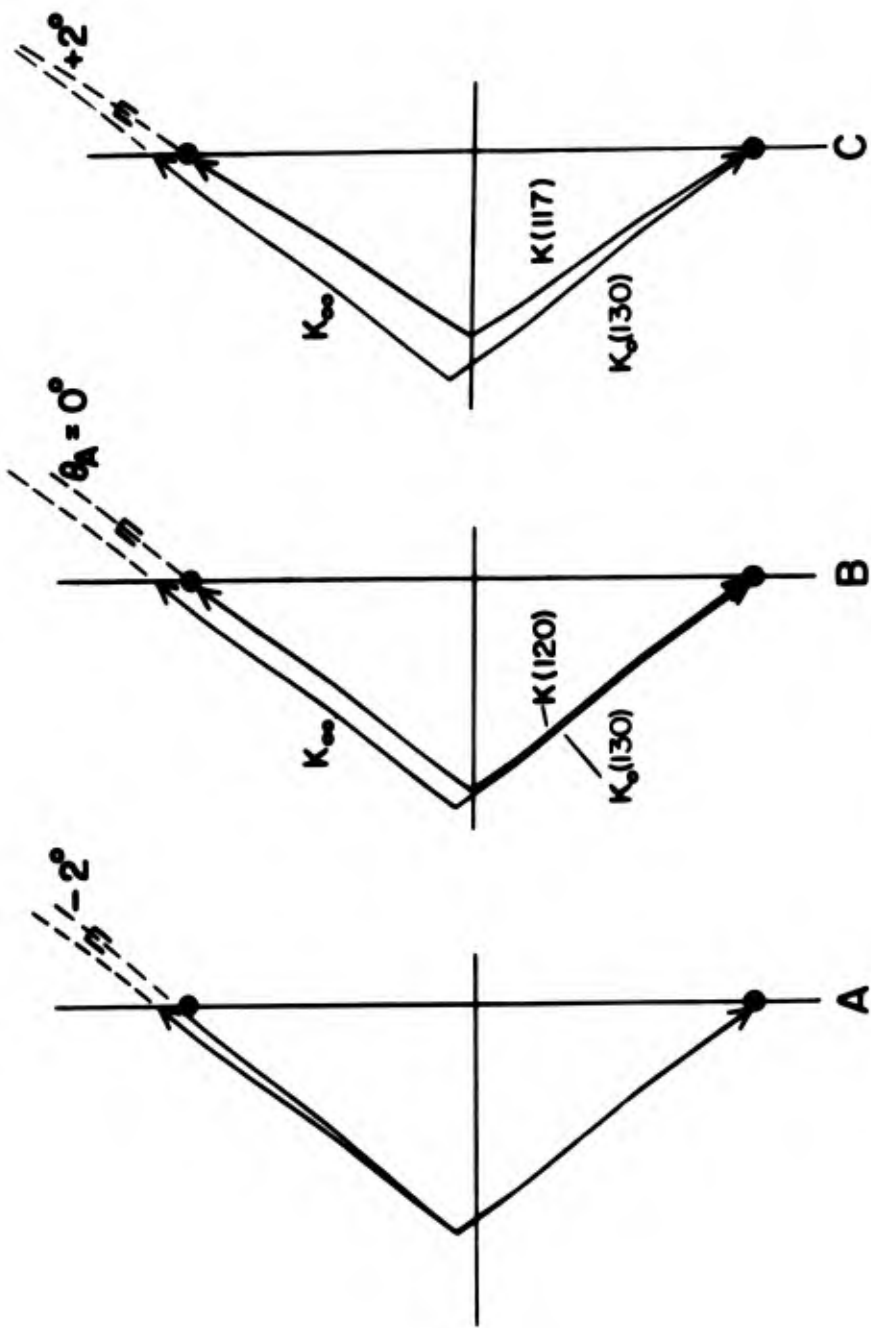


Figure 25 K-space plots showing scattering conditions for inelastic spectra of Fig. 24

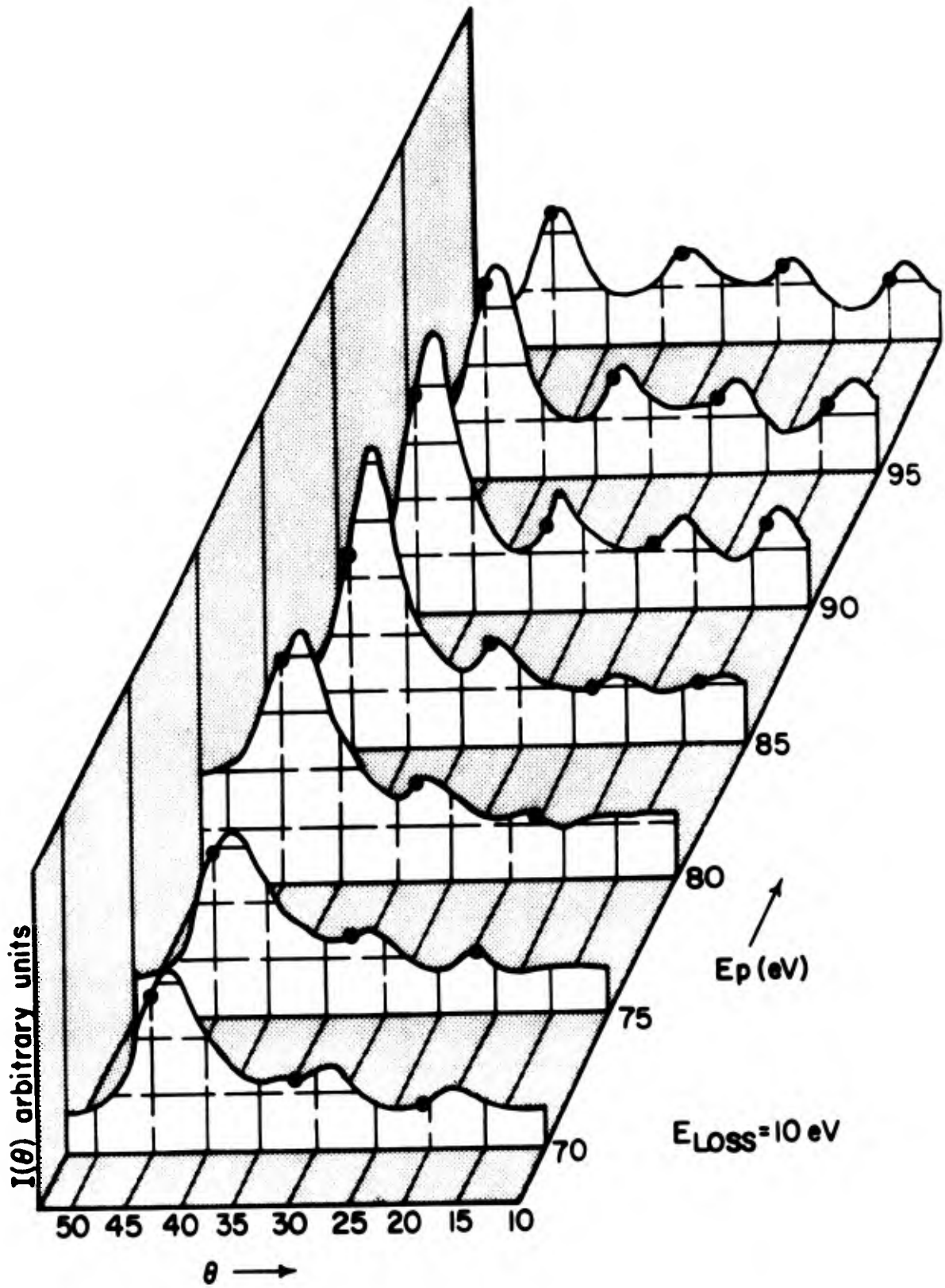


Figure 26 Inelastic angular intensity distributions in plane of incidence for $E_{Loss} = 10 \text{ eV}$ and $E_p = 70-100 \text{ eV}$

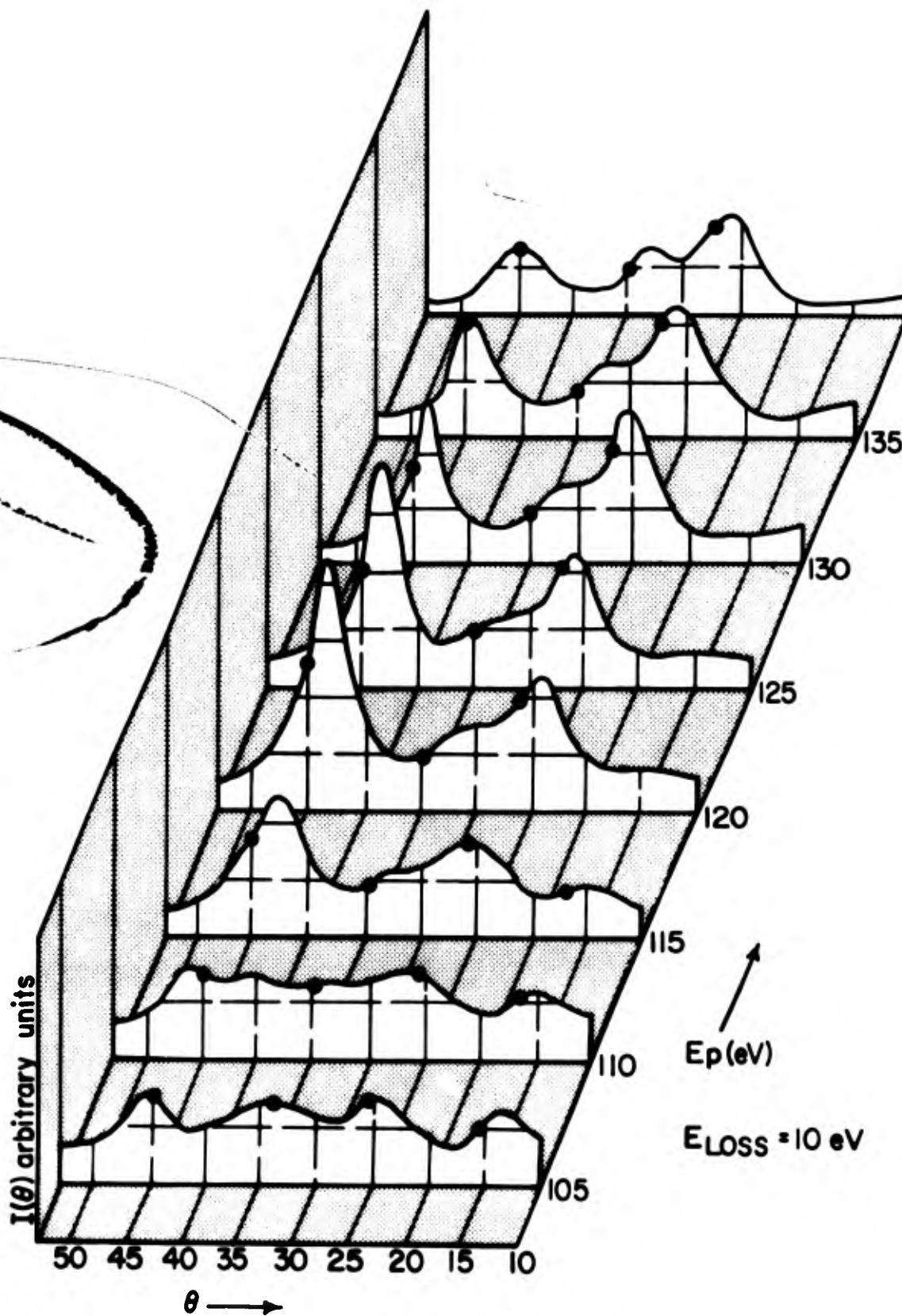


Figure 27 Inelastic angular intensity distributions in plane of incidence for $E_{Loss} = 10 \text{ eV}$ and $E_p = 105\text{-}140 \text{ eV}$

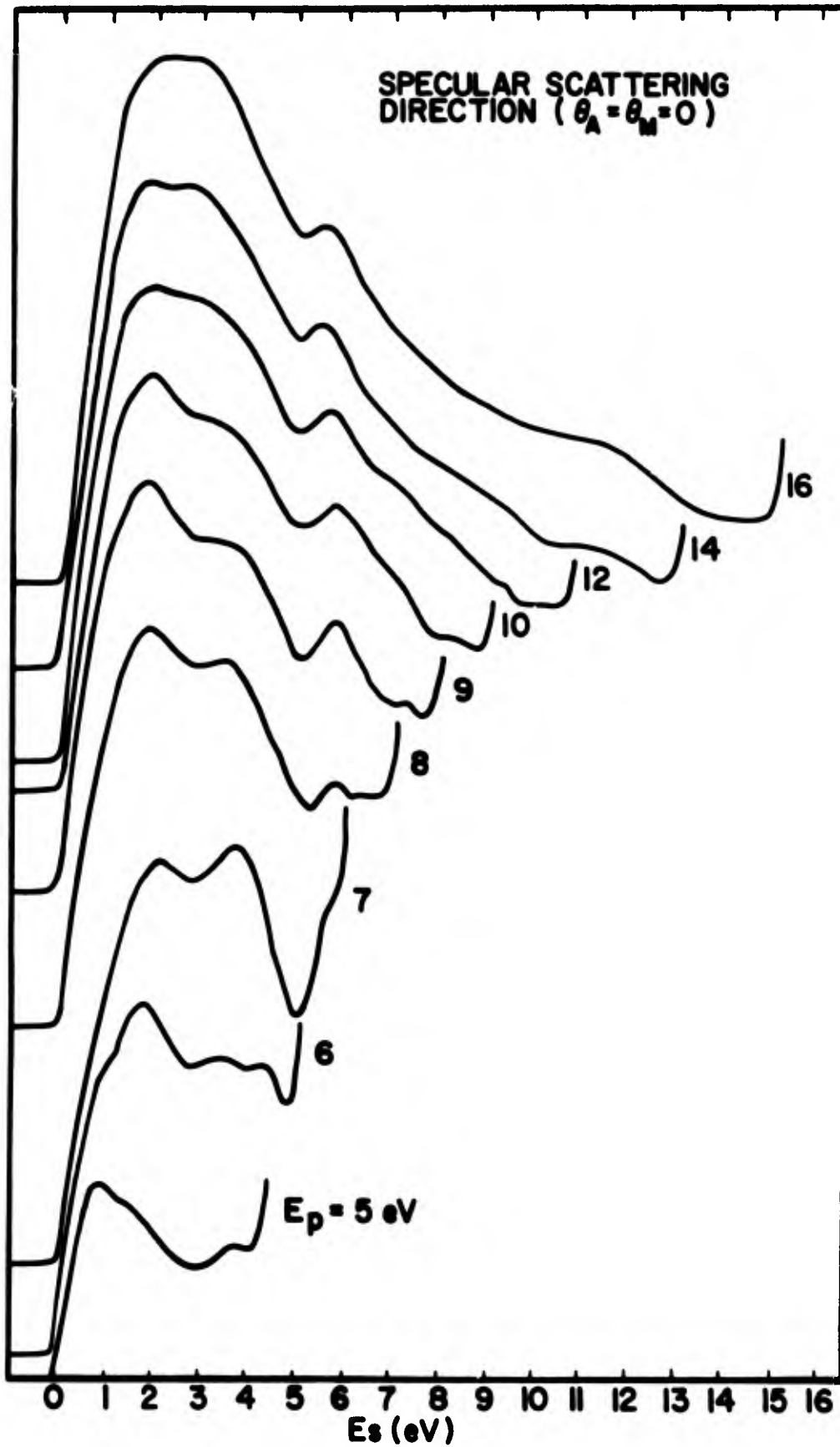


Figure 28 Secondary electron energy distributions as function of E_p , measured in specular scattering direction

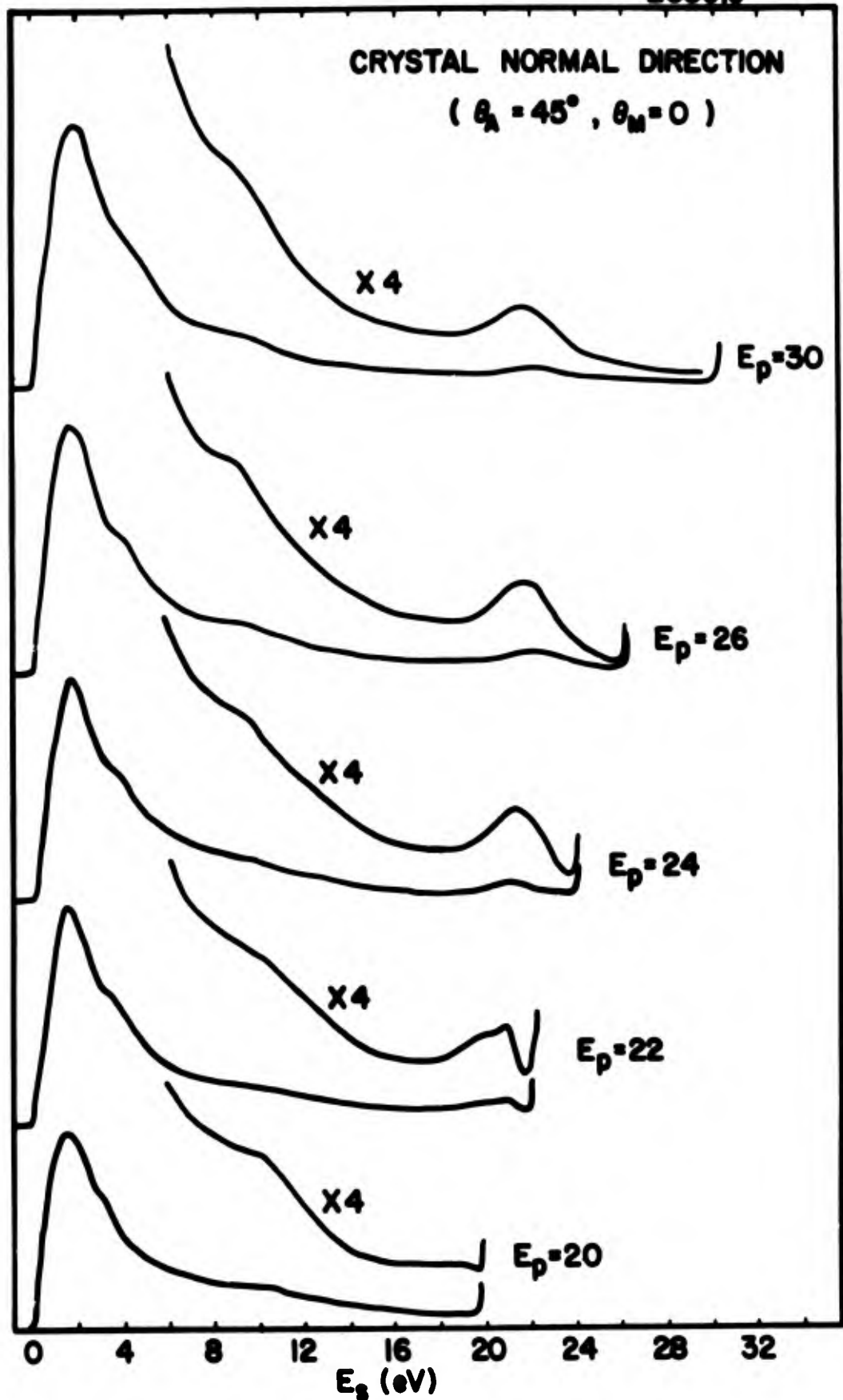


Figure 29 Secondary electron energy distributions as function of E_p , measured normal to sample surface.

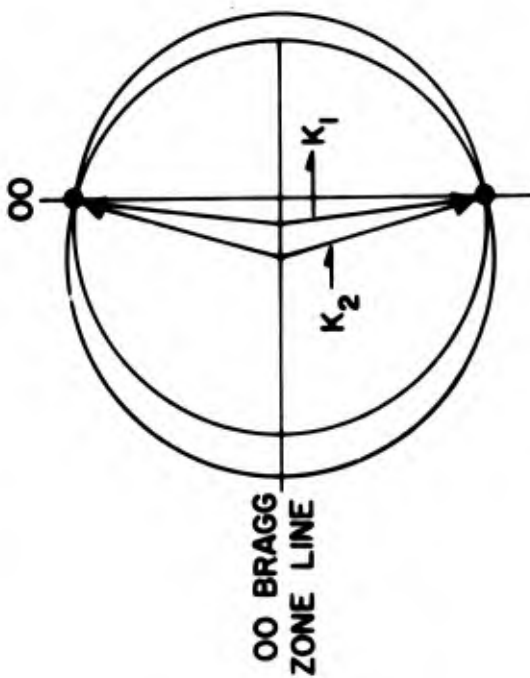
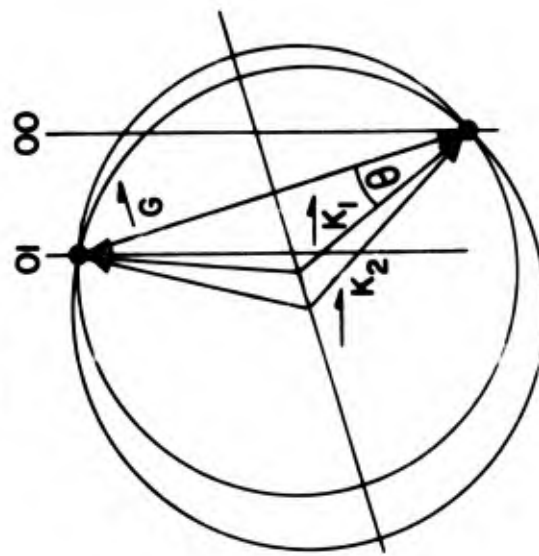
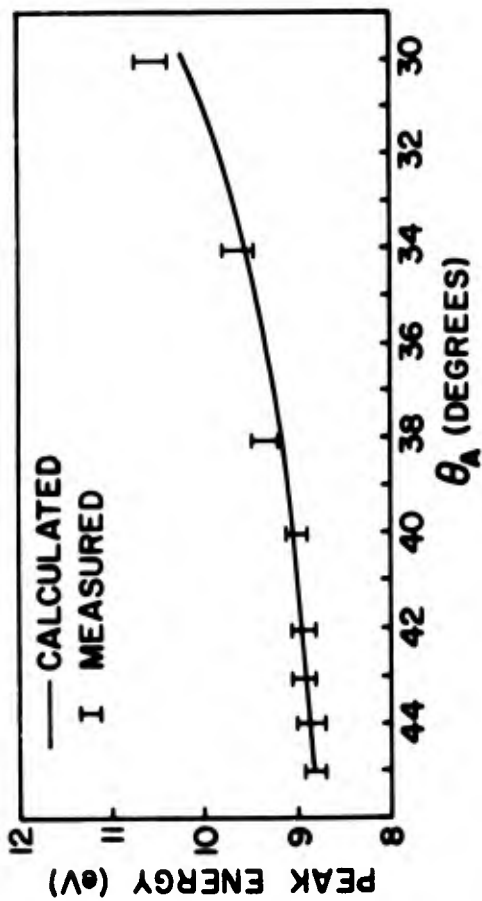
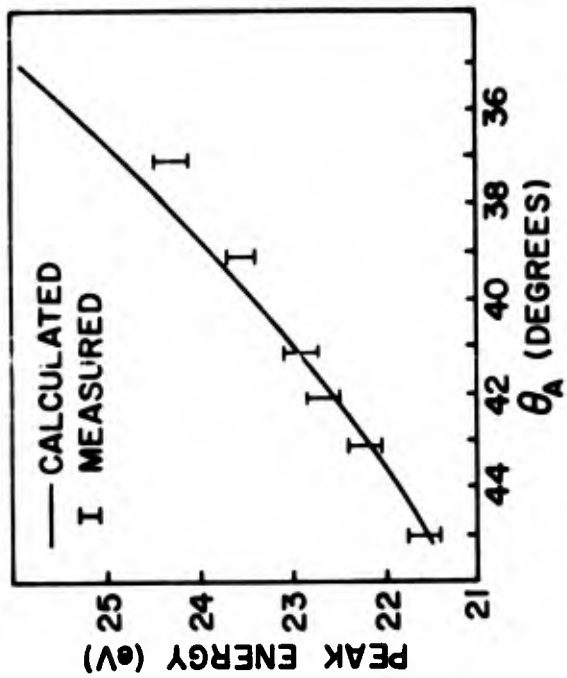


Figure 30 Secondary peak energy variation as function of scattering angle for diffraction of secondary electrons; with descriptive wave vector diagrams

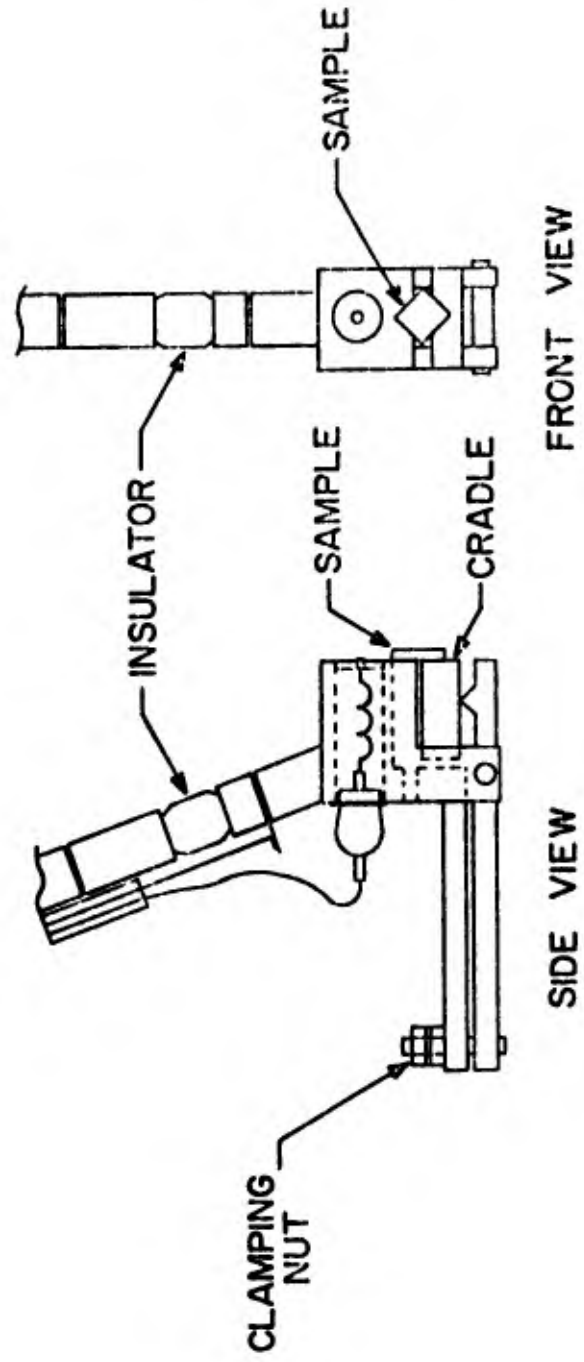
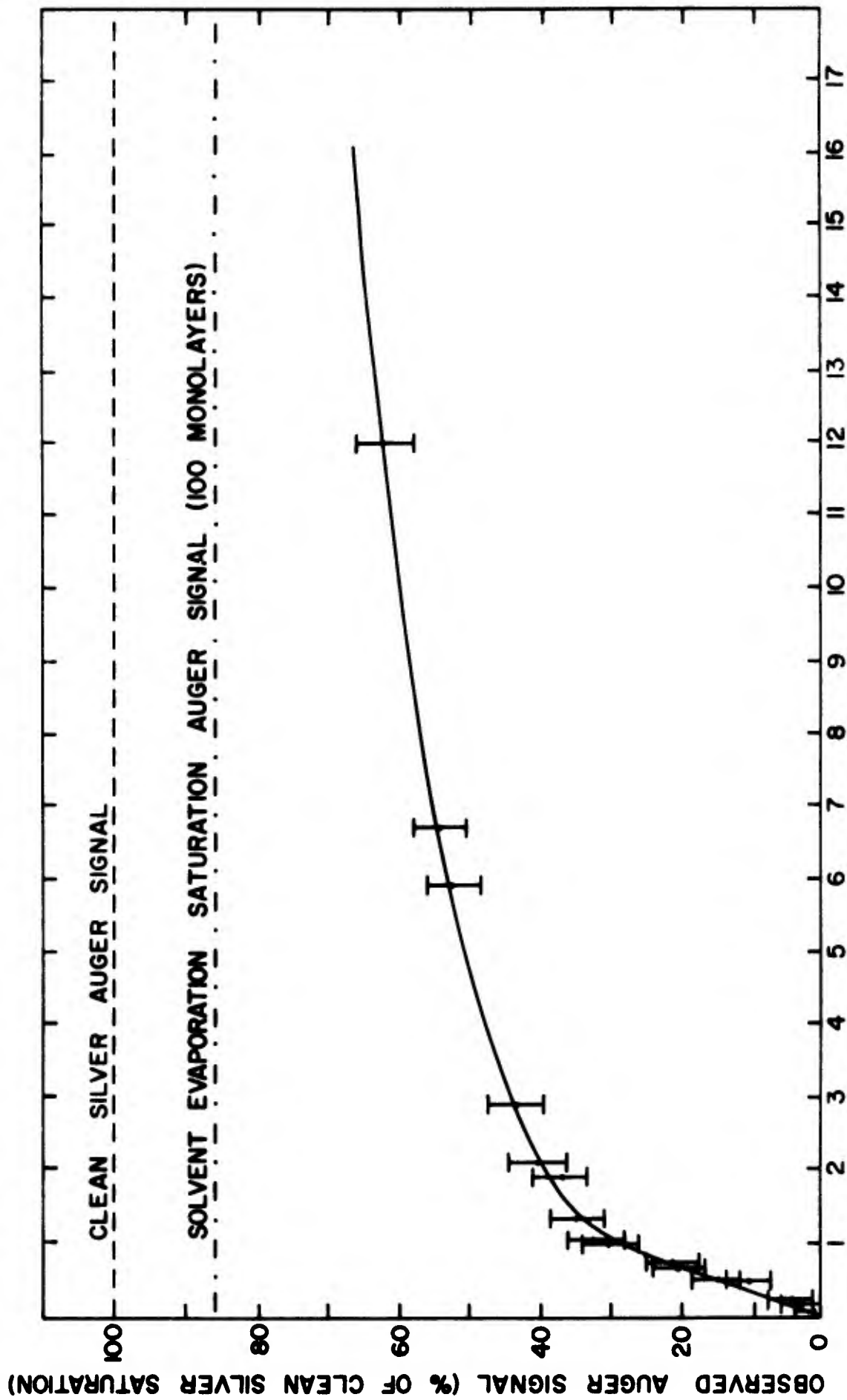


Figure 31 Crystal holder for vacuum cleavage



CALCULATED SILVER COVERAGE (MONOLAYERS)

Figure 32 Calculated Ag coverage versus observed Auger signal for drop-drying technique

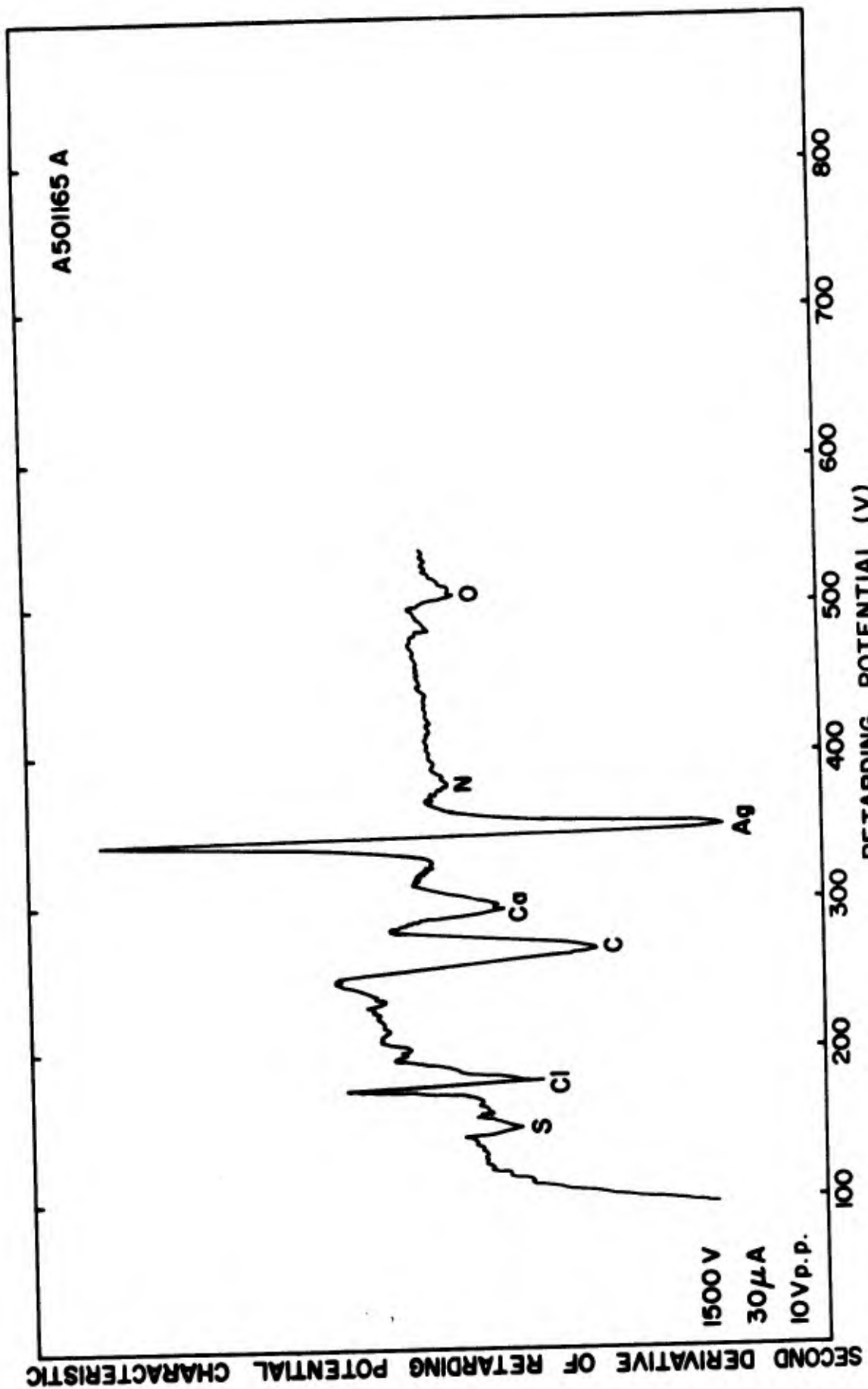


Figure 33 Auger spectrum of gold with Ag solution drop-dried

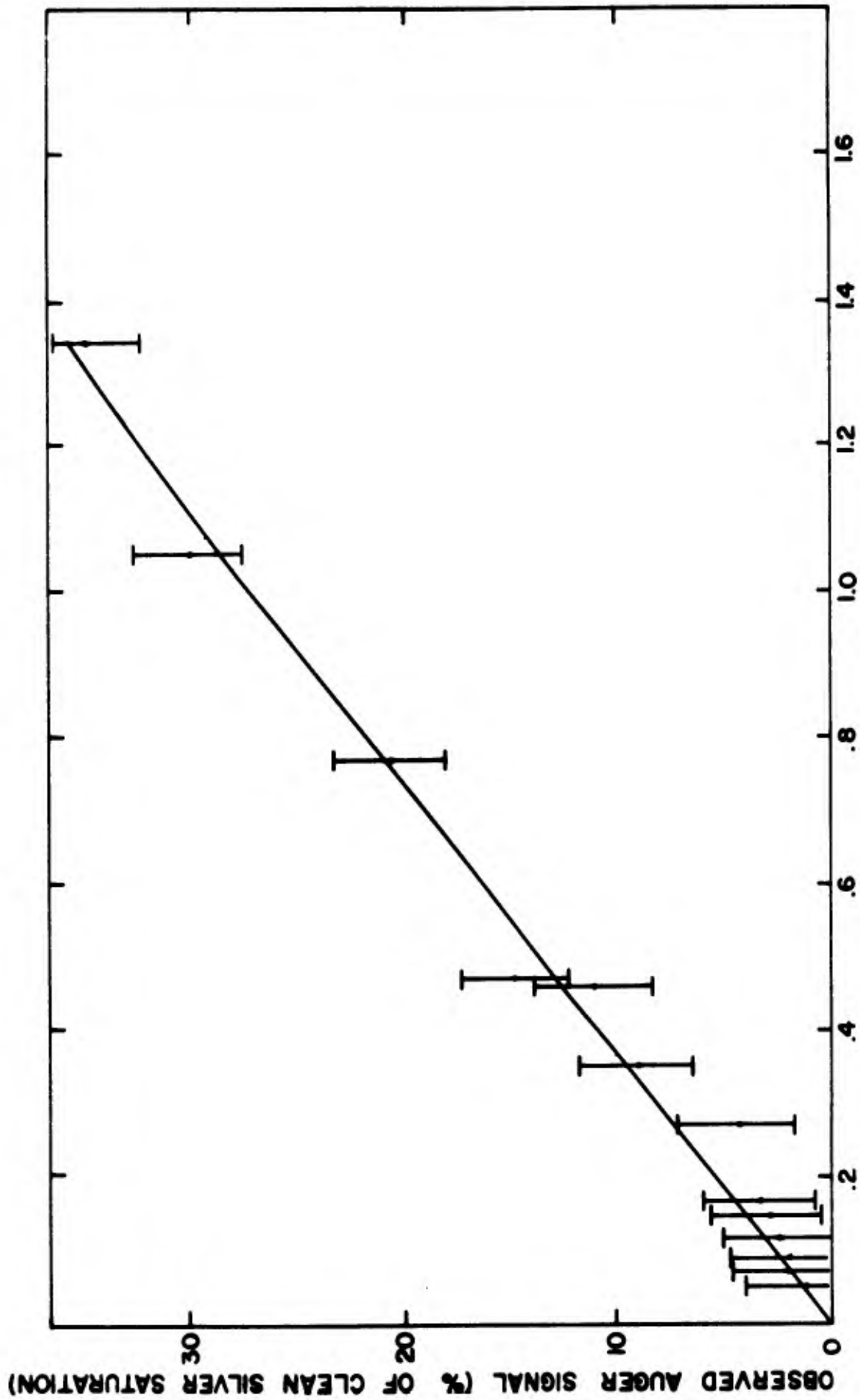


Figure 34 Calculated Ag coverage versus observed Auger signal for drop-drying technique (linear region)

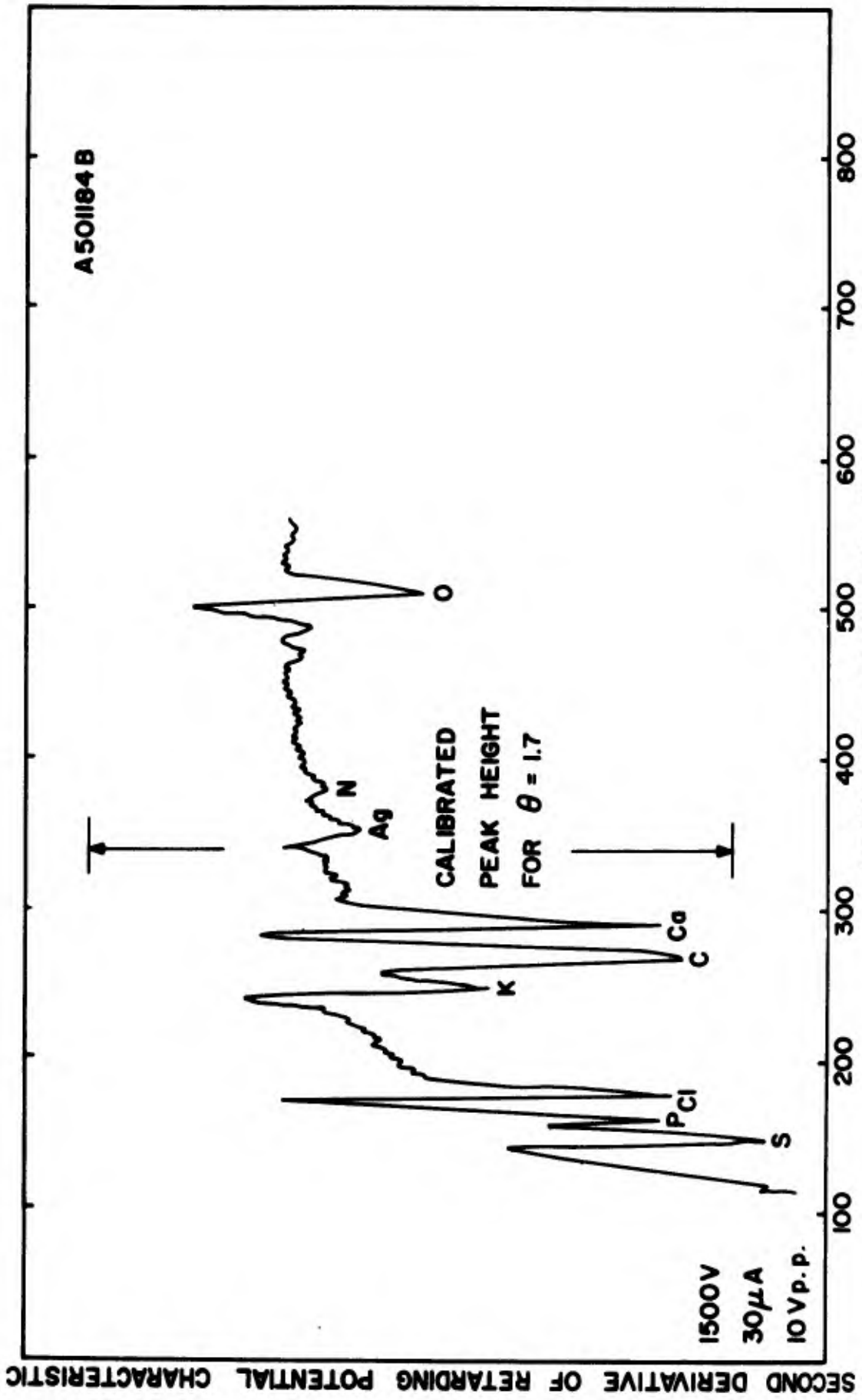


Figure 35 Auger spectra of gold sample after electroplating

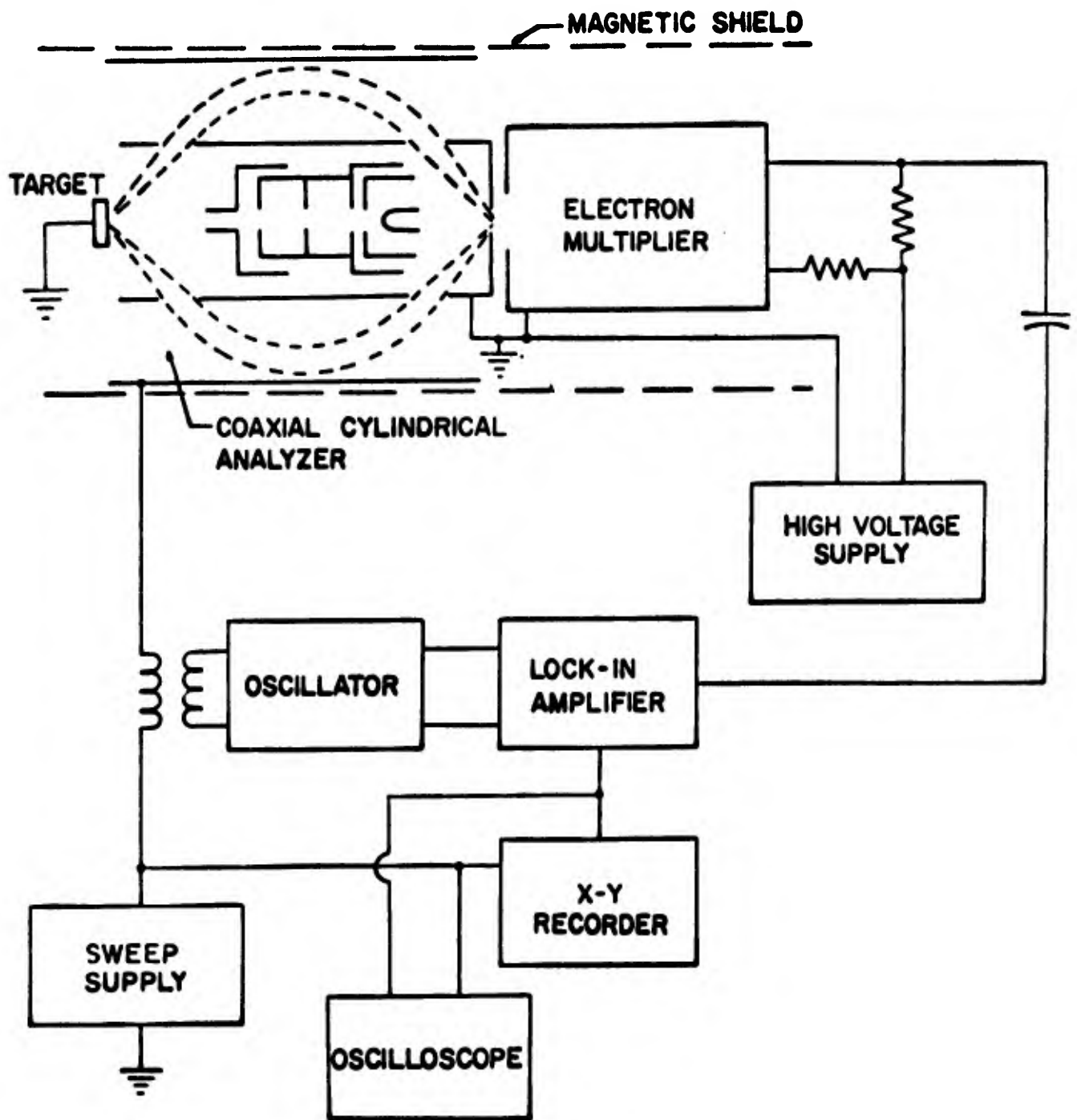


Figure 36 Cylindrical analyzer for thin film studies

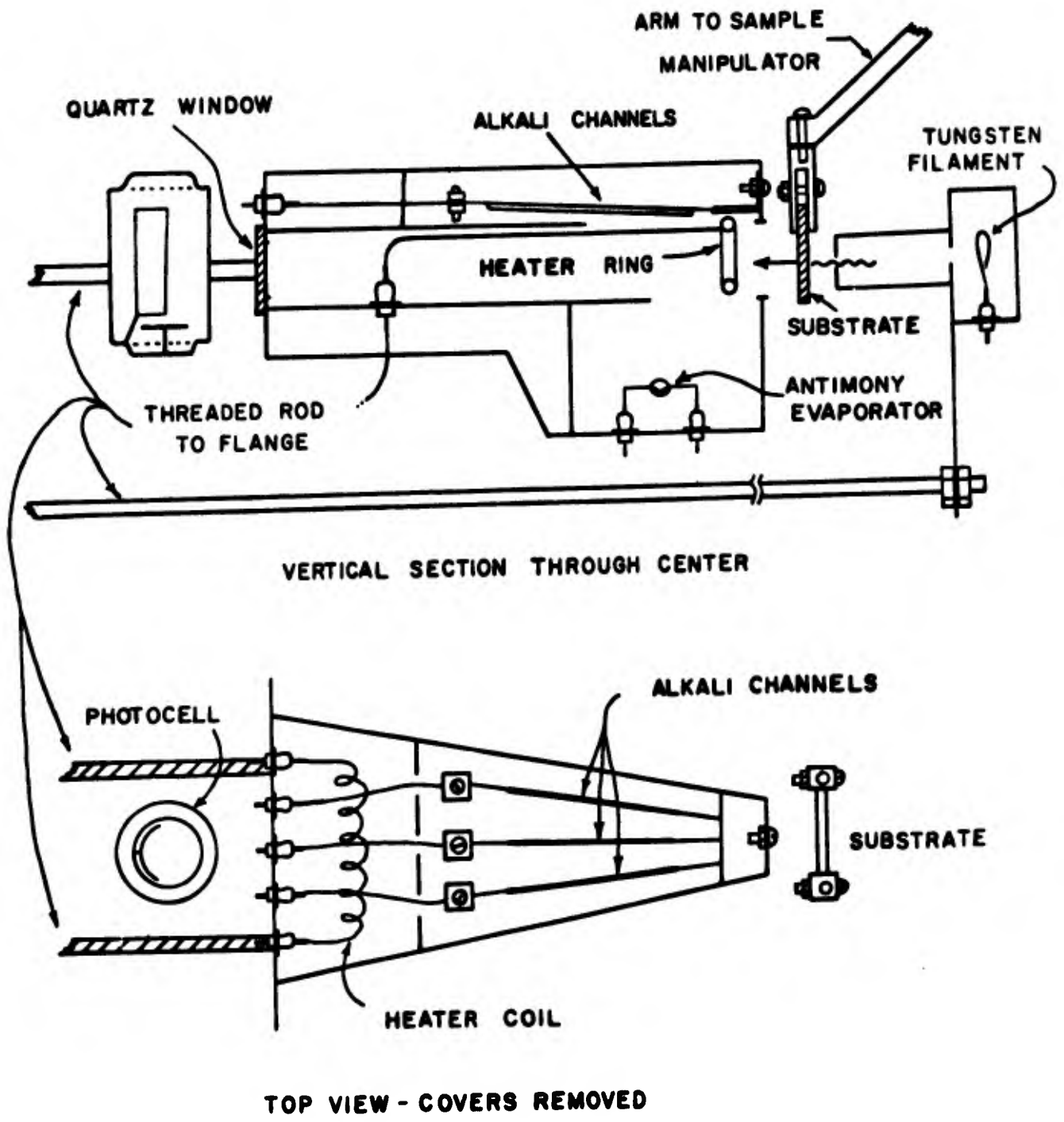


Figure 37 Flange mounted deposition chamber for thin film studies

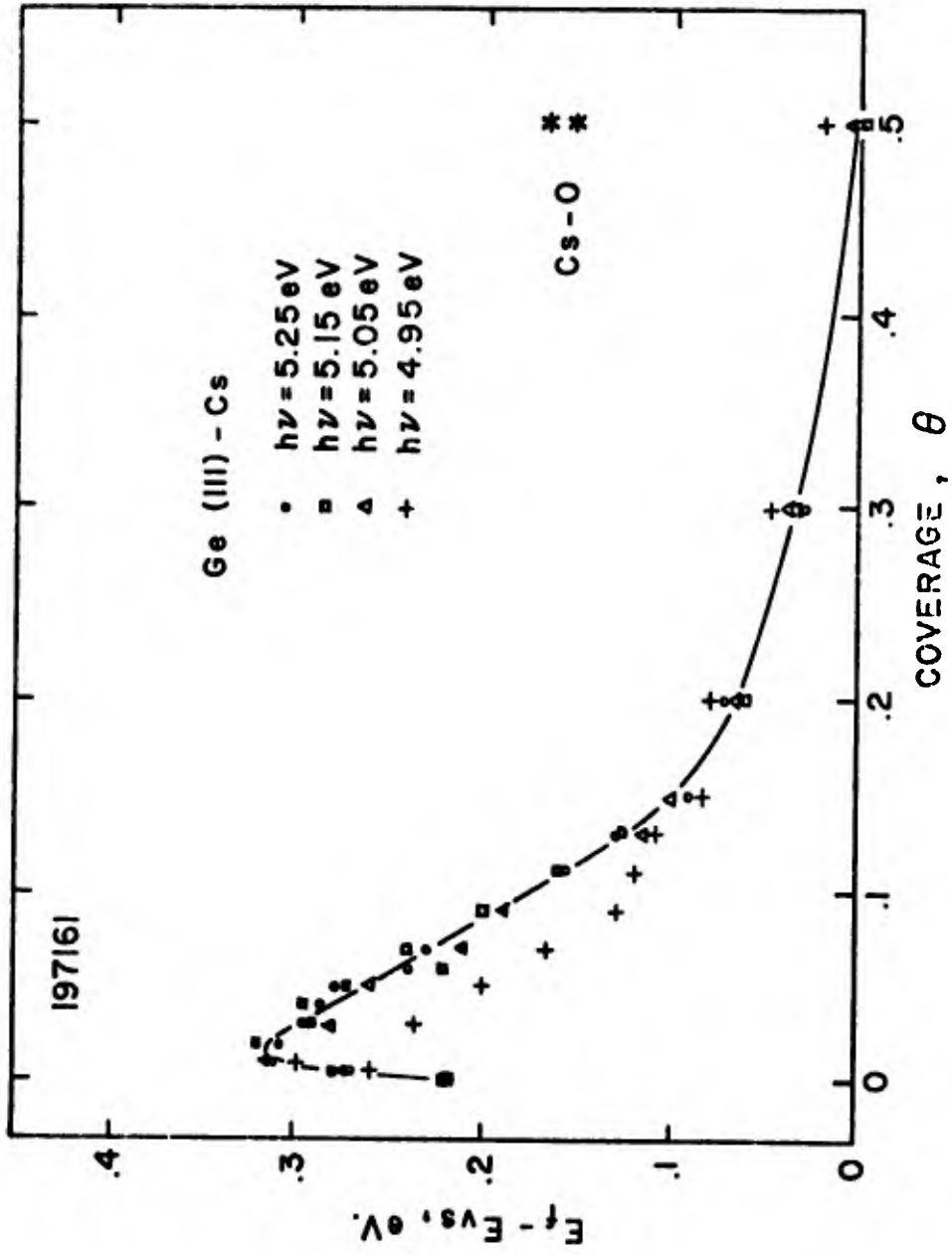


Figure 38 $E_F - E_V$ vs. cesium coverage for Ge(111)

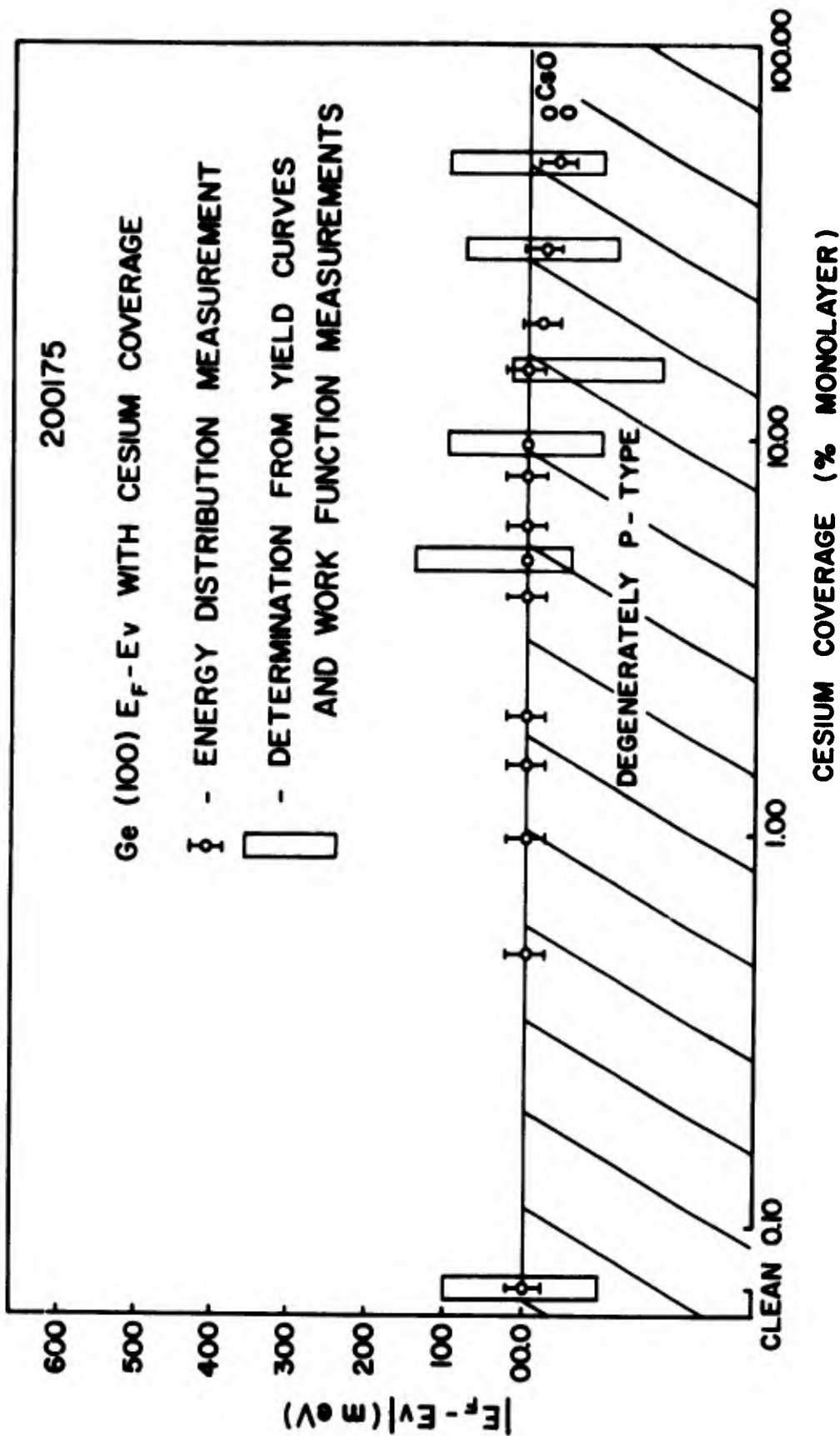


Figure 39 $E_F - E_V$ vs. cesium coverage for Ge(100)

202081

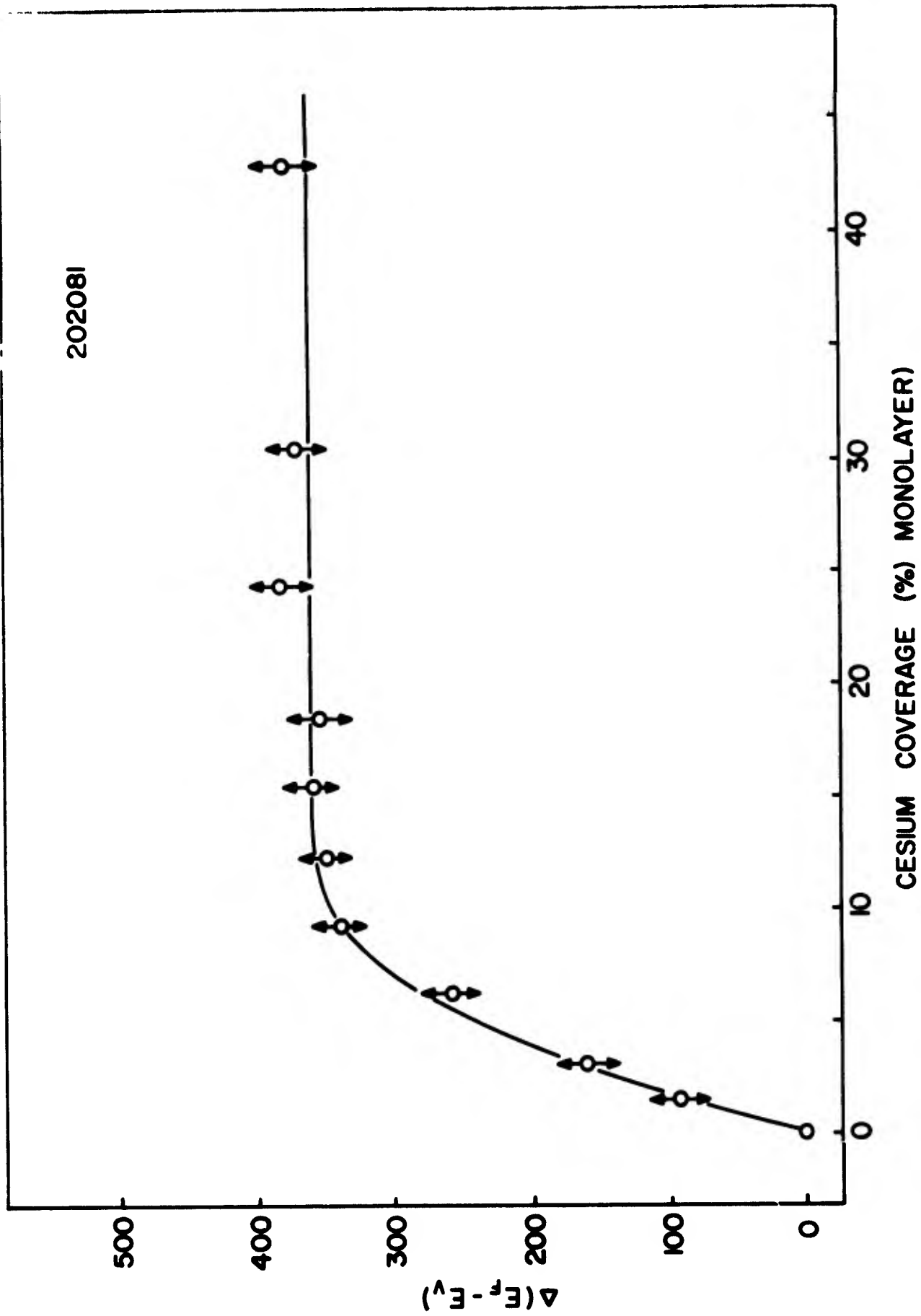


Figure 40 $E_F - E_V$ vs. cesium coverage for Si(100)

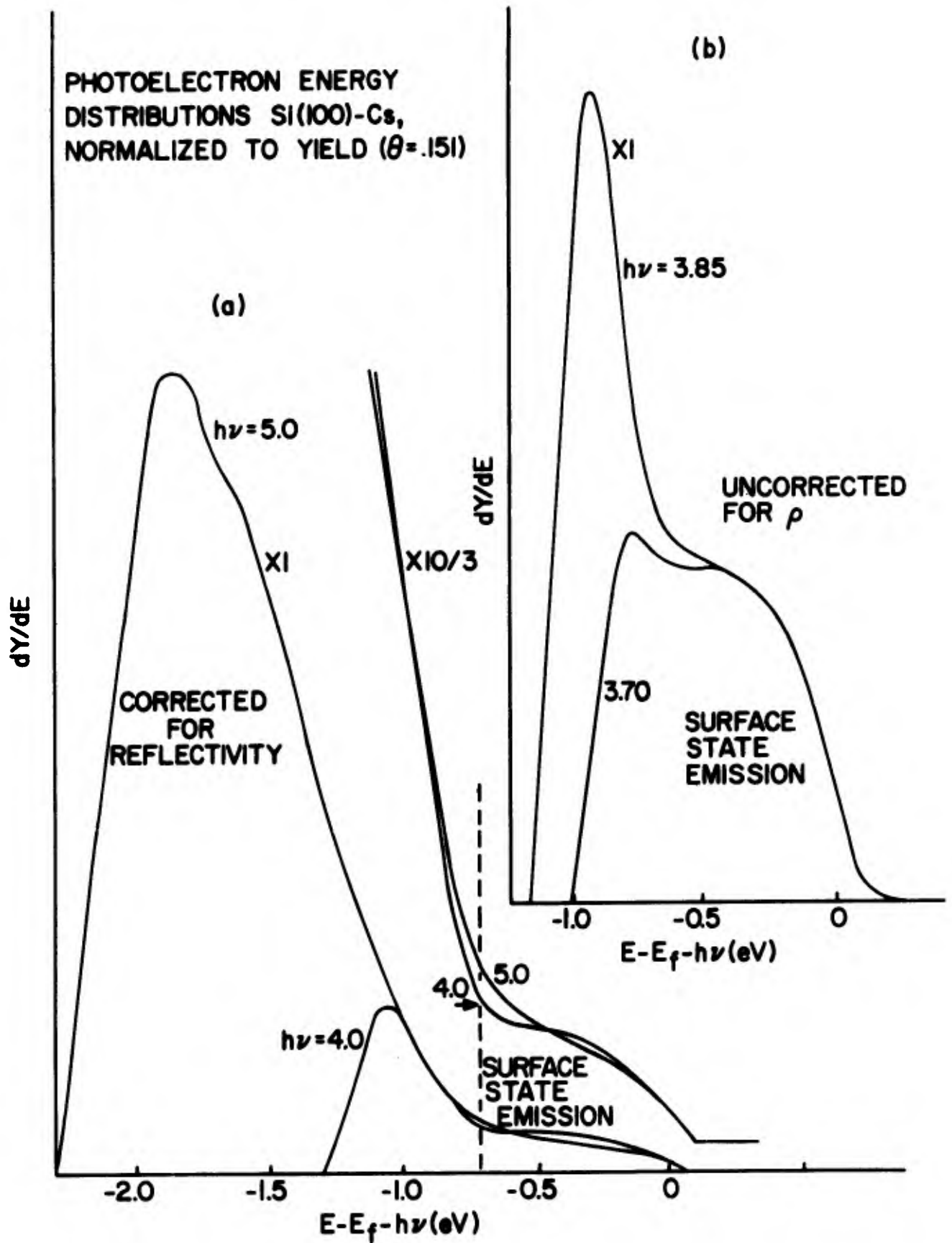


Figure 41 Photoelectron energy distributions from cesiated Si(100)

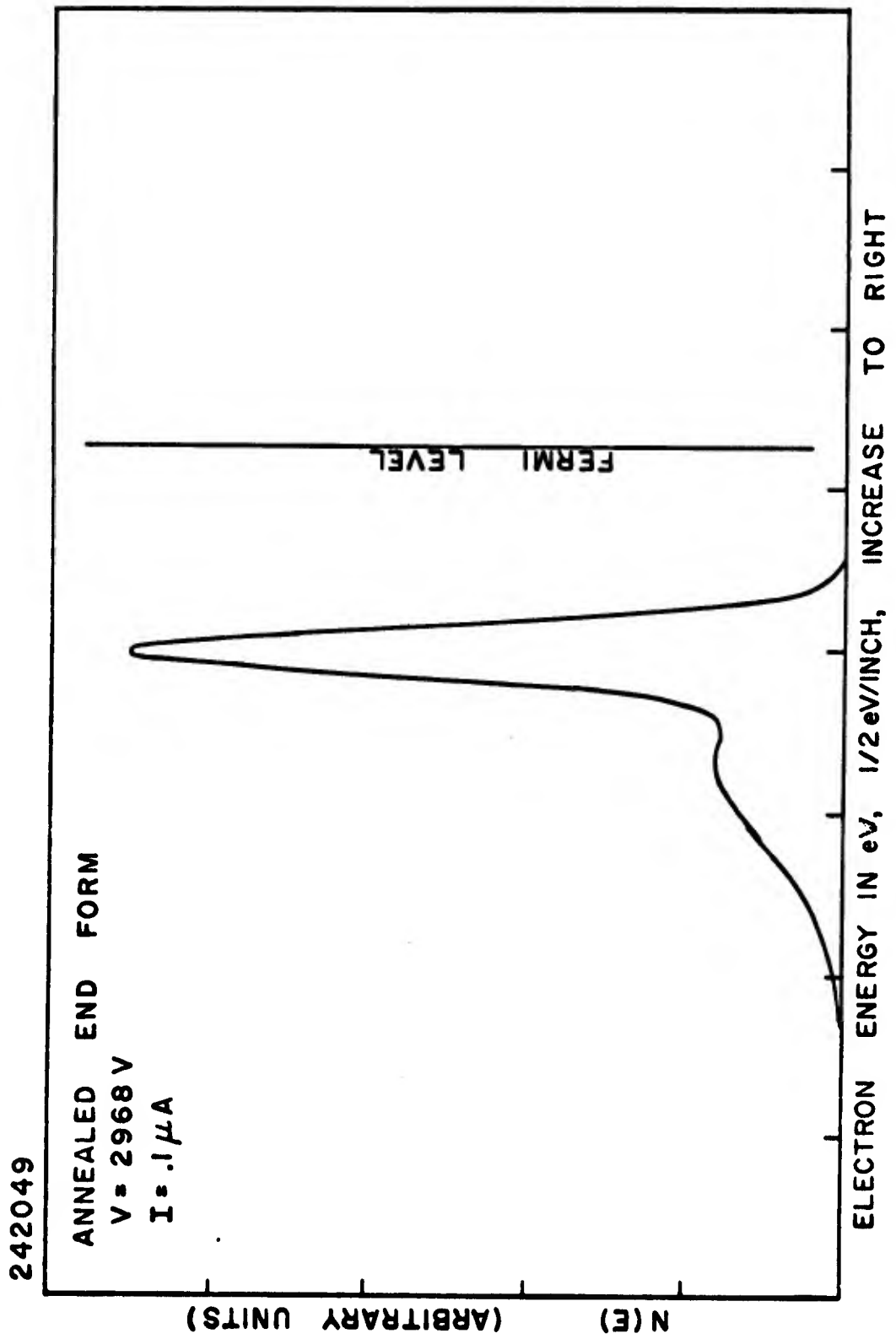


Figure 42 Energy distribution from (100) facet of Ge

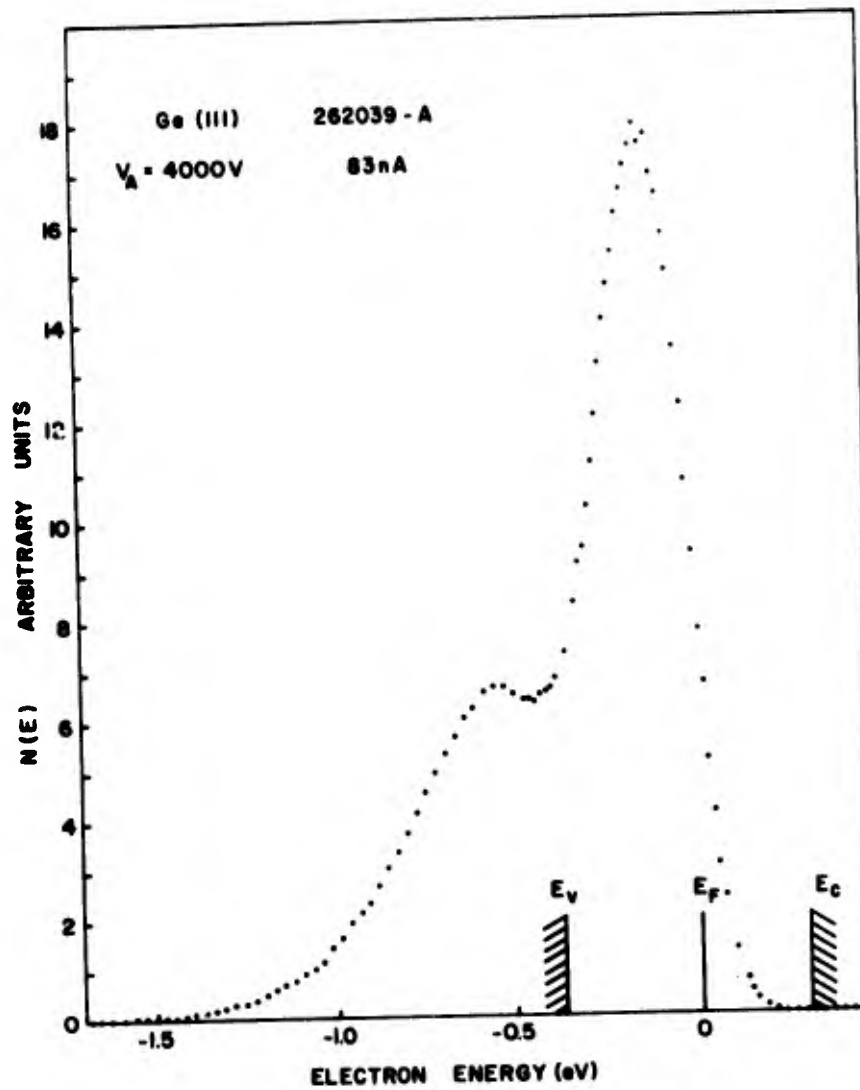


Figure 43 Energy distribution from (111) facet of Ge

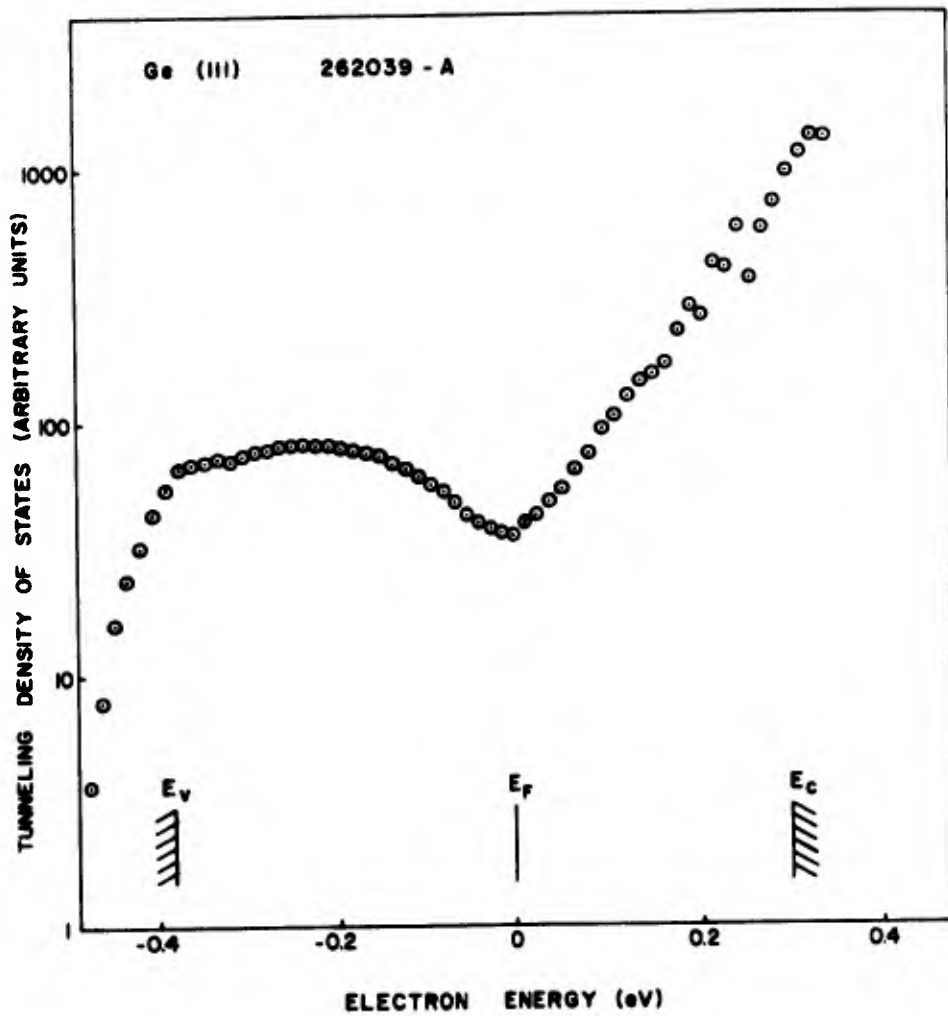


Figure 44 Tunnelling density of states for Ge(111)

UNCLASSIFIED

Security Classification

DOCUMENT CONTROL DATA - R&D

(Security classification of title, body of abstract and indexing annotation must be entered when the overall report is classified)

1 ORIGINATING ACTIVITY (Corporate author) University of Minnesota Department of Electrical Engineering Minneapolis, Minnesota 55455		2a REPORT SECURITY CLASSIFICATION UNCLASSIFIED	
		2b GROUP	
3 REPORT TITLE PHYSICS OF ELECTRON-PHOTON INTERACTION			
4 DESCRIPTIVE NOTES (Type of report and inclusive dates) Final Report (October 1, 1968-March 31, 1972)			
5 AUTHOR(S) (Last name, first name, initial) W.T. Peria			
6 REPORT DATE August, 1972		7a TOTAL NO OF PAGES 109	7b NO OF REFS 41
8a CONTRACT OR GRANT NO F33615-69-C-1053		9a ORIGINATOR'S REPORT NUMBER(S)	
b PROJECT NO 6102		9b OTHER REPORT NO(S) (Any other numbers that may be assigned this report)	
d 6102-03		AFAL-TR-73-43	
10 AVAILABILITY LIMITATION NOTICES Distribution limited to U.S. Government agencies only; test and evaluation; August 1972. Other requests for this document must be referred to AFAL/TEO, Wright-Patterson AFB, Ohio 45433			
11 SUPPLEMENTARY NOTES		12 SPONSORING MILITARY ACTIVITY Air Force Avionics Lab. (AFAL/TEO) Wright-Patterson AFB Ohio 45433	
13 ABSTRACT A continuation of the experiment examining the sticking probability of energetic alkali ions on Ge is described. Results are given for the Ge(100)-Cs system in the zero coverage region. Experimental difficulties which forced discontinuation of the study are discussed. A study of the Ge(100)-Cs-0 photosurface is described with particular emphasis on the structural changes associated with cathode formation. A stable negative electron affinity Si(100)-Cs-0 photocathode was obtained and the optimum amount of Cs determined to be 1.3 monolayer. A work function value of ~ 0.6 eV was measured. Experimental results of an electron scattering experiment on Ge(100) are summarized. A full report is forthcoming. Auger spectra obtained from vacuum-cleaned alkali halide crystals are presented and some of the difficulties encountered are summarized. Preliminary evaluation of the use of Auger spectroscopy for the analysis of aqueous solutions is described. A description of a system for studying complex photocathodes is given.			

KEY WORDS	LINK A		LINK B		LINK C	
	ROLE	WT	ROLE	WT	ROLE	WT
Photoemission						
photocathodes						
Auger spectroscopy						
semiconductor surfaces						
surface states						
field emission						
electron scattering						

INSTRUCTIONS

1. **ORIGINATING ACTIVITY:** Enter the name and address of the contractor, subcontractor, grantee, Department of Defense activity or other organization (*corporate author*) issuing the report.
2. **REPORT SECURITY CLASSIFICATION:** Enter the overall security classification of the report. Indicate whether "Restricted Data" is included. Marking is to be in accordance with appropriate security regulations.
3. **GROUP:** Automatic downgrading is specified in DoD Directives S200.10 and Armed Forces Industrial Manual. Enter the group number. Also, when applicable, show that optional markings have been used for Group 3 and Group 4 as authorized.
4. **REPORT TITLE:** Enter the complete report title in all capital letters. Titles in all cases should be unclassified. If a meaningful title cannot be selected without classification, show title classification in all capitals in parenthesis immediately following the title.
5. **DESCRIPTIVE NOTES:** If appropriate, enter the type of report, e.g., interim, progress, summary, annual, or final. Give the inclusive dates when a specific reporting period is covered.
6. **AUTHOR(S):** Enter the name(s) of author(s) as shown on or in the report. Enter last name, first name, middle initial. If military, show rank and branch of service. The name of the principal author is an absolute minimum requirement.
7. **REPORT DATE:** Enter the date of the report as day, month, year, or month, year. If more than one date appears on the report, use date of publication.
8. **TOTAL NUMBER OF PAGES:** The total page count should follow normal pagination procedures, i.e., enter the number of pages containing information.
9. **NUMBER OF REFERENCES:** Enter the total number of references cited in the report.
10. **CONTRACT OR GRANT NUMBER:** If appropriate, enter the applicable number of the contract or grant under which the report was written.
11. **PROJECT NUMBER:** Enter the appropriate military department identification, such as project number, subproject number, system numbers, task number, etc.
12. **ORIGINATOR'S REPORT NUMBER(S):** Enter the official report number by which the document will be identified and controlled by the originating activity. This number must be unique to this report.
13. **OTHER REPORT NUMBER(S):** If the report has been assigned any other report numbers (either by the originator or by the sponsor), also enter this number(s).
14. **AVAILABILITY LIMITATION NOTICES:** Enter any limitation on further dissemination of the report, other than those

imposed by security classification, using standard statements such as:

- (1) "Qualified requesters may obtain copies of this report from DDC."
- (2) "Foreign announcement and dissemination of this report by DDC is not authorized."
- (3) "U. S. Government agencies may obtain copies of this report directly from DDC. Other qualified DDC users shall request through _____."
- (4) "U. S. military agencies may obtain copies of this report directly from DDC. Other qualified users shall request through _____."
- (5) "All distribution of this report is controlled. Qualified DDC users shall request through _____."

If the report has been furnished to the Office of Technical Services, Department of Commerce, for sale to the public, indicate this fact and enter the price, if known.

11. **SUPPLEMENTARY NOTES:** Use for additional explanatory notes.

12. **SPONSORING MILITARY ACTIVITY:** Enter the name of the departmental project office or laboratory sponsoring (paying for) the research and development. Include address.

13. **ABSTRACT:** Enter an abstract giving a brief and factual summary of the document indicative of the report, even though it may also appear elsewhere in the body of the technical report. If additional space is required, a continuation sheet shall be attached.

It is highly desirable that the abstract of classified reports be unclassified. Each paragraph of the abstract shall end with an indication of the military security classification of the information in the paragraph, represented as (TS), (S), (C), or (U).

There is no limitation on the length of the abstract. However, the suggested length is from 150 to 225 words.

14. **KEY WORDS:** Key words are technically meaningful terms or short phrases that characterize a report and may be used as index entries for cataloging the report. Key words must be selected so that no security classification is required. Identifiers, such as equipment model designation, trade name, military project code name, geographic location, may be used as key words but will be followed by an indication of technical context. The assignment of links, roles, and weights is optional.

DISTRIBUTION LIST

<u>ACTIVITIES AT WRIGHT-PATTERSON AFB, OHIO 45433</u>	<u>COPIES</u>
AFAL/TSR Wright-Patterson AFB, Ohio 45433	1
AFAL/TEO ATTN: William H. Nelson Wright-Patterson AFB, Ohio 45433	3
2750 ABWg (SSL) Wright-Patterson AFB, Ohio 45433	1
ARL/LB ATTN: Dr. Guderley Wright-Patterson AFB, Ohio 45433	1
AFIT/LD Wright-Patterson AFB, Ohio 45433	1
AFAL/WR ATTN: Technical Director Wright-Patterson AFB, Ohio 45433	1
AFAL/RS ATTN: Technical Director Wright-Patterson AFB, Ohio 45433	1
AFAL/NV ATTN: Technical Director Wright-Patterson AFB, Ohio 45433	1
ASD/OIP ATTN: Robert Quayle Wright-Patterson AFB, Ohio 45433	1
AFML/LPT Wright-Patterson AFB, Ohio 45433	1
AFML/LTE Wright-Patterson AFB, Ohio 45433	1

OTHER DEPARTMENT OF DEFENSE ACTIVITIESAIR FORCE

AUL (3T-64-519) 1
Maxwell AFB, AL 36112

Hq, USAF (SAMID) 1
Wash, DC 20330

DAD (ATT) 1
ATTN: V. L. Reiersen
Eglin AFB, FL 32542

AFCRL (OPL) 1
ATTN: Mr. Bradbury
LG Hanscom Field
Bedford, MA 01731

Commander 1
RADC/ISCA
ATTN: Mr. M. Kesselman
Griffiss AFB, NY 13440

NAVY

Director, Office of Naval Research 1
ATTN: Code 421 (Dr. W. J. Condell)
Department of the Navy
Arlington, VA 22217

Naval Electronics Systems Command 1
ATTN: Code 051812 (Carl Rigdon)
Wash, DC 20350

ARMY

Office of Chief, Army Research and Development 1
Department of the Army
ATTN: Dr. Robert B. Watson (CRDPES)
Wash, DC 20310

Director 1
USAEL
HQS USAECOM
ATTN: AMSEL-KL-TD
Ft. Monmouth, NJ 07703

Director 1
USAEL
HQS USAECOM
ATTN: AMSEL-KL-SM
Ft. Monmouth, NJ 07703

Director 1
 USAEL
 HQS USAECOM
 ATTN: AMSEL-TL-QD (Mr. I. Reingold)
 Ft. Monmouth, NJ 07703

OTHER U.S. GOVERNMENT AGENCIES

Advisory Group on Electron Devices 4
 201 Varick St., 9th Floor
 New York, NY 10014

DDC (TISIA-1) 2
 Cameron Station
 5010 Duke St.
 Alexandria, VA 22314

Scientific and Technical Information Facility 2
 ATTN: NASA Representative (SAK/DL)
 P. O. Box 5700
 Bethesda, MD 20014

NON-GOVERNMENT INDIVIDUALS AND ORGANIZATIONS

Aerospace Corporation 1
 Post Office Box 95085
 ATTN: Library Acquisitions Group
 Los Angeles, CA 90045

Ohio University 1
 Department of Electrical Engineering
 College of Engineering and Technology
 Athens, Ohio 45701

Lincoln Laboratory, MIT 1
 ATTN: Dr. Frank L. McNamara
 Post Office Box 73
 Lexington, MA 02173

Hughes Research Laboratories 1
 ATTN: Dr. George Smith
 3011 Malibu Canyon Road
 Malibu, CA 90265

Westinghouse Electron Tube Division 1
 ATTN: Mr. Robert Schaffer
 Elmira, NY 14902

EIA (Section JT-4) 1
ATTN: J. F. Hessman
2001 Eye St., N.W.
Wash, DC

Sylvania Electronic Systems 1
ATTN: Mr. H. Sonnenbert
Post Office Box 188
Mountain View, CA 94040

General Electric Company 1
Research and Development Center
ATTN: Dr. R. Reddington
Post Office Box 8
Schenectady, NY 12301

EMR Photo Device 1
ATTN: R. Hahn
Post Office Box 44
Princeton, NJ 08540

University of California 1
ATTN: Professor John Winnery
Berkeley, CA 94720

Arizona State University 1
ATTN: Dr. I. Kaufman
Tempe, AZ 85281

Yale University 1
Department of Electrical Engineering
ATTN: Dr. T. Fischer
New Haven, CT 06520

Bell Telephone Laboratories, Inc 1
Electro-Optical Devices Lab
ATTN: Dr. E. I. Gordon
Murray Hill, NJ 07974

RCA Electronic Components 1
ATTN: Dr. Ralph Simon
New Holland Pike
Lancaster, PA 17603

Litton Industries 1
Electron Tube Division
ATTN: B. C. Einstine
960 Industrial Road
San Carlos, CA 94070

Sylvania Electronics, Inc. 1
ATTN: Mr. Mahlon Fischer
Johnston St.
Seneca Falls, NY 13148

Westinghouse Electric Corporation 1
Friendship International Airport, ATTN: Dr. Jas. Hall
P. O. Box 746
Baltimore, MD 21203

General Electric Co., ATTN: Mr. E. I. Bortels 1
3430 So. Dixie Drive
Dayton, OH 45439